In the IOCCG Report Series:

1. *Minimum Requirements for an Operational Ocean-Colour Sensor for the Open Ocean (1998).*
2. *Status and Plans for Satellite Ocean-Colour Missions: Considerations for Complementary Missions (1999).*
3. *Remote Sensing of Ocean Colour in Coastal, and Other Optically-Complex, Waters (2000).*
4. *Guide to the Creation and Use of Ocean-Colour, Level-3, Binned Data Products (2004).*
5. *Remote Sensing of Inherent Optical Properties: Fundamentals, Tests of Algorithms, and Applications (2006).*
6. *Ocean-Colour Data Merging (2007).*
7. *Why Ocean Colour? The Societal Benefits of Ocean-Colour Technology (2008).*
8. *Remote Sensing in Fisheries and Aquaculture (2009).*
9. *Partition of the Ocean into Ecological Provinces: Role of Ocean-Colour Radiometry (2009).*
10. *Atmospheric Correction for Remotely-Sensed Ocean-Colour Products (this volume).*

Reports and Monographs of the International Ocean-Colour Coordinating Group

An Affiliated Program of the Scientific Committee on Oceanic Research (SCOR)
An Associated Member of the Committee on Earth Observation Satellites (CEOS)

IOCCG Report Number 10, 2010

Atmospheric Correction for Remotely-Sensed Ocean-Colour Products

Edited by:
Menghua Wang, NOAA/NESDIS Center for Satellite Applications and Research, USA

Report of an IOCCG working group on Comparison of Atmospheric Correction Algorithms, chaired by Menghua Wang, and based on contributions from (in alphabetical order):

David Antoine	Laboratoire d'Oceanographie de Villefranche, France
Pierre-Yves Deschamps	Laboratoire d'Optique Atmospherique, France
Robert Frouin	Scripps Institution of Oceanography, UCSD, USA
Hajime Fukushima	Tokai University, Japan
Howard R. Gordon	University of Miami, USA
André Morel	Laboratoire d'Oceanographie de Villefranche, France
Jean-Marc Nicolas	Laboratoire d'Optique Atmospherique, France
Menghua Wang	NOAA/NESDIS Center for Satellite Applications and Research, USA

Series Editor: Venetia Stuart

Correct citation for this publication:

IOCCG (2010). Atmospheric Correction for Remotely-Sensed Ocean-Colour Products. Wang, M. (ed.), Reports of the International Ocean-Colour Coordinating Group, No. 10, IOCCG, Dartmouth, Canada.

The International Ocean-Colour Coordinating Group (IOCCG) is an international group of experts in the field of satellite ocean colour, acting as a liaison and communication channel between users, managers and agencies in the ocean-colour arena.

The IOCCG is sponsored by the Canadian Space Agency (CSA), Centre National d'Etudes Spatiales (CNES, France), Department of Fisheries and Oceans (Bedford Institute of Oceanography, Canada), European Space Agency (ESA), GKSS Research Centre (Geesthacht, Germany), National Institute for Space Research (INPE, Brazil), Indian Space Research Organisation (ISRO), Japan Aerospace Exploration Agency (JAXA), Joint Research Centre (JRC, EC), Korean Ocean Research and Development Institute (KORDI), National Aeronautics and Space Administration (NASA, USA), National Oceanic and Atmospheric Administration (NOAA, USA), and Second Institute of Oceanography (SIO), China.

http: //www.ioccg.org

Contents

Chapter 1

Introduction

Menghua Wang, André Morel and Howard R. Gordon

1.1 The IOCCG Atmospheric Correction Working Group

The IOCCG established the atmospheric correction working group (ACWG) because atmospheric correction is a key procedure in remote sensing of ocean colour. It is important to have quantitative evaluations and comparisons of the performance of various atmospheric correction algorithms used to derive global ocean-colour products from operational ocean-colour sensors. The primary objective of the IOCCG ACWG was to quantify the performance of the various existing operational atmospheric correction algorithms so that data users can have a better picture of how data products derived from various ocean-colour satellite sensors can be compared and/or possibly merged. A number of ocean-colour sensors designed to produce global ocean-colour products have been successfully launched in recent years: the Ocean Color Temperature Scanner (OCTS) from NASDA (now JAXA) and CNES's Polarization and Directionality of the Earth's Reflectances (POLDER)-1 (both launched on 17 August 1996), NASA's Sea-Viewing Wide Field-of-View Sensor (SeaWiFS) (launched on 1 August 1997), NASA's Moderate Resolution Imaging Spectroradiometer (MODIS) on Terra (launched on 18 December 1999), ESA's Medium Resolution Imaging Spectrometer (MERIS) (launched on 1 March 2002), NASA's MODIS on Aqua (launched on 4 May 2002), the Global Imager (GLI) from NASDA (now JAXA) and POLDER-2 from CNES (both launched on 14 December 2002). In addition, POLDER-3 on PARASOL was launched on 18 December 2004, and can be used for deriving ocean-colour products. SeaWiFS, MODIS-Aqua, and MERIS have been providing global ocean-colour products continuously since their launch, while both GLI and POLDER-2 unfortunately ended their missions on 24 October 2003 due to a sudden failure of the spacecraft power system. A complete list of ocean-colour satellite sensors, including some experimental ones, can be found in the IOCCG website at: http://www.ioccg.org/sensors_ioccg.html.

In this report, four operational atmospheric correction algorithms are discussed, and their performances for various cases are compared. These include algorithms for SeaWiFS and MODIS-Aqua (Gordon and Wang, 1994a; Gordon, 1997), MERIS (Antoine

and Morel, 1999), the Ocean Colour and Temperature Scanner (OCTS) and GLI from NASDA/JAXA (Fukushima *et al.*, 1998), and POLDER. Scientists and investigators who are primarily responsible for development of these four atmospheric correction algorithms comprised the IOCCG ACWG, and are also the authors of this report.

In the past decade or so, significant efforts have been made by space agencies for validating global ocean-colour products, particularly for routine ocean-colour products from SeaWiFS, MODIS, and MERIS. Consequently, various algorithms have been updated, modified, and refined. At the same time, significant progress has been made in the development of other approaches for atmospheric correction, particularly dealing with cases for strongly-absorbing aerosols and waters with non-negligible near-infrared (NIR) ocean contributions. Therefore, another objective of the ACWG was to provide the ocean community with an overview of the current status of atmospheric correction algorithm development, including a more complete list of references for those who are interested in the details. Some outstanding issues are also discussed.

In this report, overviews of the various atmospheric correction algorithms used for global ocean-colour data processing are provided. The performance of the various algorithms is compared using common simulated data sets, mainly for open ocean (Case-1) waters and for non- or weakly-absorbing aerosols (generally present in the open ocean). It should be noted that these four operational algorithms are designed specifically for Case-1 waters and non- or weakly-absorbing aerosols. Examples from coastal Case-2 waters (sediment-dominated and yellow-substance-dominated waters) and from strongly-absorbing aerosols are also provided and discussed. Overviews are also provided of some other approaches developed in recent years for regional applications, in particular, for dealing with turbid coastal waters and strongly-absorbing aerosol issues (see Appendix B). In addition, comparison results for deriving aerosol optical thickness data are presented. Aerosol optical property data are a by-product of the atmospheric correction of ocean-colour products. The question of whether or not the various algorithms meet predefined requirements were considered to be outside the scope of this report. For this reason, the report focuses only on intercomparisons between the various algorithms.

1.2 Brief History

Very likely, the first systematic measurements of the colour of the sea from aircraft, carried out at the end of the sixties, were those of George L. Clarke, Gifford C. Ewing, and Carl J. Lorenzen (Clarke, *et al.*, 1970). The remote spectroscopy of the light backscattered from the sea in coastal waters near Woods Hole, and in offshore waters from the Sargasso Sea across Georges Bank, demonstrated the possibility of detecting the chlorophyll concentration within the upper layers. Measurements from altitudes ranging from 152 to 3050 m showed the effect of increasing 'airlight' on

the upward radiance received by the sensor, and thus the need for an 'atmospheric correction' (Austin, 1974; Clarke and Ewing, 1974). It was soon realized that the atmospheric path radiance (the atmospheric signal) was largely dominant compared to the marine signal in the visible part of the spectrum.

Simultaneously, field measurements of upward and downward spectral irradiance, $E_u(\lambda)$ and $E_d(\lambda)$, respectively, were performed by John E. Tyler and Raymond C. Smith in different water bodies (Tyler and Smith, 1970). Thereafter, systematic determinations of the same radiometric quantities were made during the SCOR WG-15 Discoverer 1970 Expedition (Tyler, 1973), and allowed the diffuse attenuation coefficients, $K_d(\lambda)$, and the irradiance reflectance, $R(\lambda) = E_u(\lambda)/E_d(\lambda)$, to be computed. The interpretation of this reflectance, a basic quantity in ocean-colour science, was given in the frame of radiative transfer (Gordon *et al.*, 1975) and also in terms of optically-significant substances present in the water (Morel and Prieur, 1977; Smith and Baker, 1978).

The problem of removing the atmospheric and surface effects from satellite imagery of the ocean was examined (Gordon, 1978; Gordon and Clark, 1980; Morel, 1980), and the technique developed for that purpose (Gordon, 1980) was then implemented into the NASA processing system used with the NIMBUS-7 Coastal Zone Color Scanner (CZCS) sensor. The problem encountered with this sensor was the absence of an appropriate channel in the near-infrared (NIR) portion of the spectrum where the open ocean can be considered as black, so that the detected signal can be assumed to be of purely atmospheric origin. As a replacement, the CZCS band at 670 nm was used along with the assumption that the marine radiance at this wavelength, $L_w(670)$, was negligible, or if not, that it could be iteratively derived based on an empirical relationship between $L_w(670)$ and the chlorophyll concentration (Smith and Wilson, 1981; Bricaud and Morel, 1987), or based on *a priori* knowledge when the chlorophyll content is sufficiently low (clear water concept) (Gordon and Clark, 1981). Such a solution, applicable to Case-1 waters fails when turbid, highly reflective, coastal waters are under consideration. This particular situation continues to represent a difficult problem.

During the CZCS era, the atmospheric contribution was predicted (and removed) based on the single scattering approximation. Within such an approach, the Rayleigh scattering by air molecules can be considered separately, and computed in the absence of the aerosol, whereas the aerosol scattering contribution can also be computed separately in the absence of molecules (Gordon and Morel, 1983). Later in the CZCS mission, and also for the present ocean-colour sensors, this simplifying assumption was abandoned. The coupling of the scattering by aerosol molecules was addressed (Gordon and Wang, 1994a), as well as the effect of polarization on the magnitude of the atmospheric contribution (Gordon *et al.*, 1988a). The new schemes for the atmospheric correction, such as those presented in this report, include these improvements, together with the consideration and selection of various types of aerosols.

Atmospheric Correction Algorithm Description

Howard R. Gordon, David Antoine, Hajime Fukushima, Menghua Wang, Robert Frouin, André Morel, Pierre-Yves Deschamps and Jean-Marc Nicolas

In this document, the reflectance $\rho(\lambda)$, is defined at a given wavelength λ, to be related to the radiance $L(\lambda)$ through $\rho(\lambda) = \pi L(\lambda)/\{F_0(\lambda)\cos\theta_0\}$, where $F_0(\lambda)$ is the extraterrestrial solar irradiance and θ_0 is the solar-zenith angle. Radiance and reflectance are interchangeable based on this definition.

The purpose of the atmospheric correction for the remote retrieval of ocean properties is to remove the atmospheric and surface effects from the signal measured by the satellite-sensor, thereby deriving the radiances coming from the ocean waters. For the ocean-atmosphere system, the top-of-atmosphere (TOA) radiance $L_t(\lambda)$ can be partitioned linearly into various distinct physical contributions:

$$L_t(\lambda) = L_r(\lambda) + L_a(\lambda) + L_{ra}(\lambda) + t(\lambda)L_{wc}(\lambda) + T(\lambda)L_g(\lambda) + t(\lambda)t_0(\lambda)\cos\theta_0[L_w(\lambda)]_N,$$
(2.1)

where $L_r(\lambda)$ is the radiances due to scattering by the air molecules (Rayleigh scattering in the absence of aerosols), $L_a(\lambda)$ is the scattering by aerosols (in the absence of air molecules), $L_{ra}(\lambda)$ is the multiple interaction term between molecules and aerosols, $L_{wc}(\lambda)$ and $L_g(\lambda)$ are the components of radiance due to whitecaps on the sea surface and the specular reflection of direct sunlight off the sea surface (sun glitter), respectively, and $[L_w(\lambda)]_N$ is the normalized water-leaving radiance due to photons that penetrate the sea surface and are backscattered out of the water. The relationship between $[L_w(\lambda)]_N$ and the actual water-leaving radiance, $L_w(\lambda)$, propagating in a direction toward the sensor is given in Appendix D. The quantities $t_0(\lambda)$ and $t(\lambda)$ are the diffuse transmittances of the atmosphere from the sun to the surface and from the surface to the sensor, respectively (Appendix C). $T(\lambda)$ is the direct transmittance from the surface to the sensor. Note that Equation 2.1 is valid when the target is large spatially, i.e., effects of the target environment can be neglected. The goal of the atmospheric correction is to retrieve the normalized water-leaving radiance $[L_w(\lambda)]_N$ accurately from the spectral measurements of the TOA radiance $L_t(\lambda)$ at the satellite altitude. We can further define the TOA atmospheric path radiance (including both contributions from atmosphere scattering and

surface reflection) as

$$L_{\text{path}}(\lambda) = L_r(\lambda) + L_a(\lambda) + L_{ra}(\lambda). \tag{2.2}$$

It should be noted that L_{path} includes any and all-multiple reflections from the Fresnel reflection of the air-sea interface. The principal challenge in atmospheric correction is the estimation and removal of $L_{\text{path}}(\lambda)$ from $L_t(\lambda)$. In Case-1 waters, $L_{\text{path}}(\lambda)$ contributes about 90% of the TOA radiance in the blue and green, and a higher fraction in the red. The estimation of the diffuse transmittances is next in the order of importance. The main difficulty with its estimation is that it depends on the angular distribution of the radiance just beneath the sea surface. $L_g(\lambda)$ can be rendered as small as desired by avoiding the region surrounding the specular image of the sun, and $L_{wc}(\lambda)$ can be estimated from surface wind speed.

In the last two decades, various atmospheric correction algorithms have been developed and used to derive global ocean-colour products for the following satellite ocean-colour sensors: OCTS (1996-1997), POLDER-1 (1996-1997), SeaWiFS (1997-present), MODIS-Terra (1999-present), MODIS-Aqua (2002-present), MERIS (2002-present), GLI (2002-2003), and POLDER-2 (2002-2003). These algorithms all use standard radiative transfer methods to compute and remove $L_r(\lambda)$ from $L_t(\lambda)$. This computation requires an estimate of the surface atmospheric pressure (and in some implementations, the surface wind speed is also used). The remaining part of $L_{\text{path}}(\lambda)$ is estimated from $L_t(\lambda)$ in the NIR wavelengths, where $[L_w(\lambda)]_N$ is negligible, providing $L_a(\lambda) + L_{ra}(\lambda)$ in the NIR. Based on $L_a(\lambda) + L_{ra}(\lambda)$ in the NIR, an estimate is made of $L_a(\lambda) + L_{ra}(\lambda)$ in the visible (VIS). The principal difference between the atmospheric correction algorithms for the various sensors listed above is in the details of how the estimate of $L_a(\lambda) + L_{ra}(\lambda)$ in the VIS is made from the estimate of $L_a(\lambda) + L_{ra}(\lambda)$ in the NIR. These algorithms are described in the following sections.

2.1   The SeaWiFS/MODIS Algorithm

Gordon and Wang (1994a) developed the basic SeaWiFS/MODIS atmospheric correction algorithm. Its performance was then validated through simulations, and after launch, through direct application of the algorithms to SeaWiFS and MODIS imagery and comparison with *in situ* data (McClain *et al.*, 2004; Wang, *et al.*, 2005; Bailey and Werdell, 2006; Zibordi, *et al.*, 2006). Using Equation 2.1, the procedure for the SeaWiFS/MODIS atmospheric correction can be described as follows:

❖ the Rayleigh radiance $L_r(\lambda)$ is computed from the Rayleigh lookup tables that were prepared using the vector radiative transfer theory (all polarization effects included) with inputs of the solar-sensor geometry, atmospheric pressure, and wind speed (Gordon *et al.*, 1988a; Gordon and Wang, 1992; Wang, 2002; 2005);

❖ the whitecap radiance $L_{wc}(\lambda)$ is modelled using input of the sea surface wind speed (Gordon and Wang, 1994b; Frouin, *et al.*, 1996; Moore *et al.*, 2000);

❖ the TOA sun glint radiance $T(\lambda)L_g(\lambda)$ is mostly masked out and residual contamination is corrected based on a model of sea surface slope distribution (Cox and Munk, 1954; Wang and Bailey, 2001);

❖ the fact that $[L_w(\lambda)]_N$ is negligible in the NIR (for the open ocean), can be used to estimate the combination $L_a(\lambda) + L_{ra}(\lambda)$ in the NIR bands, and aerosol modelling can be used to extrapolate it from the NIR to the visible bands; and finally

❖ $t_0(\lambda)$ and $t(\lambda)$ are estimated (Yang and Gordon, 1997) and used to compute $[L_w(\lambda)]_N$ in the visible wavelengths.

The derived $[L_w(\lambda)]_N$ spectra data are then used as inputs for all of the ocean bio-optical products from ocean-colour sensors.

To account for the multiple-scattering effect on $L_a(\lambda) + L_{ra}(\lambda)$, which depends on the aerosol properties and increases as the aerosol concentration increases, realistic aerosol models are required. A set of 12 aerosol models from, or derived from, the work of Shettle and Fenn (1979) are used for the SeaWiFS/MODIS data processing (Shettle and Fenn, 1979; Gordon and Wang, 1994a; Wang *et al.*, 2005). Specifically, these 12 aerosol models are:

❖ the 'Oceanic' model with a relative humidity (RH) of 99% (denoted O99),

❖ the 'Maritime' model with a RH of 50%, 70%, 90%, and 99% (denoted M50, M70, M90 and M99),

❖ the 'Coastal' model with a RH of 50%, 70%, 90%, and 99% (denoted C50, C70, C90, and C99), and

❖ the 'Tropospheric' model with a RH of 50%, 90%, and 99% (denoted T50, T90, and T99).

These 12 aerosol models represent non- or weakly-absorbing aerosols. The single-scattering albedo at 865 nm varies from 0.930 for the T50 model, to 1.0 for the O99 model, while the Ångström exponent between wavelengths 510 and 865 nm changes from -0.087 for the O99 model to 1.53 for the T50 model.

These aerosol models are used to compute lookup tables (LUTs) for computing $L_a(\lambda) + L_{ra}(\lambda)$. Briefly, for each aerosol model radiative transfer, computations are carried out to determine $L_{\text{path}}(\lambda)$ as a function of the aerosol optical thickness $\tau_a(\lambda)$, for a variety of sensor-sun geometries. For these computations the sea surface is assumed to be flat and free of whitecaps. The computations are carried out using scalar radiative transfer (Gordon and Wang, 1994a) or more recently, complete vector radiative transfer (Wang, 2006a). The appropriate L_r is then subtracted from L_{path} yielding $L_a(\lambda) + L_{ra}(\lambda)$, or equivalently, $\rho_a(\lambda) + \rho_{ra}(\lambda)$. For a given geometry, $\rho_a(\lambda) + \rho_{ra}(\lambda)$ is then fit to a fourth order polynomial in the single-scattered aerosol reflectance $\rho_{as}(\lambda)$, i.e.,

$$\rho_a + \rho_{ra} = a\rho_{as} + b\rho_{as}^2 + c\rho_{as}^3 + d\rho_{as}^4, \tag{2.3}$$

where a, b, c and d are constants,

$$\rho_{as}(\lambda) \equiv \frac{\omega_a(\lambda)\tau_a(\lambda)\left[P_a(\lambda, \alpha_+) + P_a(\lambda, \alpha_-)\left[r(\theta) + r(\theta_0)\right]\right]}{4\cos\theta\cos\theta_0} \equiv \frac{\omega_a(\lambda)\tau_a(\lambda)\left[p_a(\lambda)\right]}{4\cos\theta\cos\theta_0}$$

(2.4)

$$\cos\alpha_\pm = \pm\cos\theta\cos\theta_0 + \sin\theta\sin\theta_0\cos(\phi - \phi_0),$$ (2.5)

P_a is the aerosol scattering phase function at the appropriate scattering angle, θ and ϕ are the polar and azimuth angles of the sensor's view of the sea surface, θ_0, and ϕ_0 are the solar zenith and azimuth angles, and r is the Fresnel reflectance for the indicated incidence angle (in air). The LUTs contain a, b, c and d constants for a large number of viewing-sun geometries and for values of $\tau_a(\lambda)$ up to 0.8.

The procedure for estimating $L_a(\lambda) + L_{ra}(\lambda)$ or $\rho_a(\lambda) + \rho_{ra}(\lambda)$ is to estimate this quantity in the NIR first, assuming negligible $[L_w(\lambda)]_N$ in that region of the spectrum for the open oceans. Using the aerosol LUTs, the sensor-measured spectral variation of $\rho_a(\lambda) + \rho_{ra}(\lambda)$ at the two NIR bands can be used to estimate $\rho_{as}(\lambda)$ for the same two bands. As $\rho_{as}(\lambda)$ is related directly to the aerosol phase function, single scattering albedo, and optical thickness, it can be computed directly for each aerosol model. It is then possible to select the most appropriate aerosol models for which the computed radiances are best matched with the measured values. This is accomplished by comparing the measured value of the single scattering epsilon (SSE) with those computed for each model (Gordon and Wang, 1994a; Wang and Gordon, 1994; Wang, 2004). SSE is denoted $\epsilon(\lambda_i, \lambda_j)$, where λ_i and λ_j are the two NIR wavelengths, and

$$\epsilon(\lambda_i, \lambda_j) \equiv \frac{\rho_{as}(\lambda_i)}{\rho_{as}(\lambda_j)} = \frac{\omega_a(\lambda_i)\tau_a(\lambda_i)p_a(\lambda_i)}{\omega_a(\lambda_j)\tau_a(\lambda_j)p_a(\lambda_j)}.$$ (2.6)

This approach was used (and is still used today) because the SSE depends only on the aerosol model, and not on the aerosol optical thickness. Based on the derived SSE values in the NIR bands, the two most appropriate aerosol models (from the set of 12 models) are retrieved and used for estimation of the aerosol effects in the visible bands $L_a(\lambda) + L_{ra}(\lambda)$. Therefore, the normalized water-leaving radiance in the visible wavelengths $[L_w(\lambda)]_N$ can be derived through Equation 2.1.

For Case-2 waters, where the assumption that $[L_w(\lambda)]_N$ is negligible in the NIR may be violated, the procedure is to:

❖ use the derived $[L_w(\lambda)]_N$ to estimate $[L_w(\lambda)]_N$ in the NIR,
❖ use this estimate of $[L_w(\lambda)]_N$ in the NIR to provide a new estimate of $\rho_a(\lambda) + \rho_{ra}(\lambda)$ in the NIR, and
❖ use this as above to estimate $\rho_a(\lambda) + \rho_{ra}(\lambda)$ and hence $[L_w(\lambda)]_N$ in the visible.

This latter procedure can be iterated as many times as required for convergence. For this report, we have implemented the Siegel *et al.* (2000) algorithm to estimate the NIR ocean contributions in Case-2 waters.

2.2 The MERIS Algorithm

Basic principles for the MERIS atmospheric correction scheme are described in Antoine and Morel (1998), and the practical implementation and tests are developed in Antoine and Morel (1999), as described below. In this multiple scattering algorithm, the path reflectance is derived globally to perform the atmospheric correction, instead of separately assessing $\rho_a(\lambda)$ and $\rho_r(\lambda)$. It is therefore based on the following decomposition of the total reflectance at the top of atmosphere level ($\rho_t(\lambda)$):

$$\rho_t(\lambda) = \rho_{\text{path}}(\lambda) + t(\lambda)\rho_w(\lambda), \tag{2.7}$$

where $\rho_{\text{path}}(\lambda)$ is the atmospheric path reflectance and $t(\lambda)$ is the diffuse transmittance along the pixel-to-sensor path (approximated as per Gordon *et al.*, 1983). The reflectance ρ_{path} is formed by all photons reaching the TOA after one or several scattering events in the atmosphere, with the exception of those that entered the ocean.

It was shown that the $[\rho_{\text{path}}/\rho_r]$ ratios are monotonic and unique functions of τ_a for a given aerosol and geometry (Antoine and Morel, 1998). Such functions allow an aerosol type to be identified among several predefined models, by using LUTs generated from radiative transfer simulations. These LUTs contain the coefficients of the quadratic relationship between the ratio $[\rho_{\text{path}}/\rho_r]$ and τ_a, for several aerosol models, geometries, and wavelengths. A quadratic expression is used to account for the saturating behavior of the $[\rho_{\text{path}}/\rho_r]$ versus τ_a relationship for large values of τ_a. For moderate τ_a values ($<\sim 0.5$) linearity between $[\rho_{\text{path}}/\rho_r]$ and τ_a is actually observed (for non-absorbing aerosols).

The scheme starts with computing $[\rho_{\text{path}}/\rho_r]$ at two wavelengths in the NIR (λ_{NIR1} and λ_{NIR2}, where there is no marine signal), where ρ_{path} is measured by the sensor and ρ_r is pre-computed. Because multiple scattering effects depend on the aerosol type, several values of $\tau_a(\lambda_{NIR1})$ correspond to the value of $[\rho_{\text{path}}/\rho_r]$ at λ_{NIR1}, each one being associated with a given aerosol model. This set of $\tau_a(\lambda_{NIR1})$ values is converted into the equivalent set at λ_{NIR2}, using the spectral attenuation coefficients of each aerosol. Several values of the ratio $[\rho_{\text{path}}/\rho_r]$ at λ_{NIR2} correspond to these $\tau_a(\lambda_{NIR2})$ values; they differ according to the aerosol type. Comparing this set of values to the actual $[\rho_{\text{path}}/\rho_r]$ ratio at λ_{NIR2} allows the two aerosol models that most closely bracket the actual $[\rho_{\text{path}}/\rho_r]$ ratio to be selected. The remaining steps of the algorithm rest on the assumption that the mixing ratio derived in this way, is invariable with wavelength (Gordon and Wang, 1994a). It is then possible to estimate $[\rho_{\text{path}}/\rho_r]$ for the visible wavelengths from its values at λ_{NIR2} and λ_{NIR1}, provided that the relationships with τ_a have been previously established for the appropriate wavelengths. Atmospheric correction of the visible observations is obtained by multiplying the ratio $[\rho_{\text{path}}/\rho_r]$ by ρ_r, leading to ρ_{path}, and, by difference with ρ_t, to the marine reflectance. The aerosol optical thickness is obtained at each wavelength as the weighted average of the two values corresponding to

the two bracketing aerosol models, again using the mixing ratio obtained from the NIR bands. The accuracy of reflectance in the blue wavebands of such a multiple scattering algorithm has been shown to be about ±0.002.

The algorithm implementation used for the present inter-comparison exercise is described in Antoine and Morel (1999). The radiative transfer computations needed to produce the necessary LUTs were performed with a scalar version of the Matrix Operator Method (MOM) code (Fell and Fischer, 2001). The more recent implementation into the ESA operational processing environment is somewhat different. It still uses aerosol models from Shettle and Fenn (1979), but with a set of 12 aerosol models similar to the one used in the SeaWiFS processing. The Rayleigh and aerosol LUTs are now generated from a successive order of scattering radiative transfer code including polarization (Deuze *et al.*, 1989).

This 'Case-1 water algorithm' (assumption of no marine signal in the NIR) is applied over all water types, after application of a specific procedure (Moore *et al.*, 1999), which removes the marine signal, if any, in the NIR bands.

A specific feature has been implemented in addition to the reference scheme for non-absorbing aerosols, which allows absorbing aerosols to be detected using the observations at 510 nm and assumptions about the marine signal at this wavelength (Nobileau and Antoine, 2005). When the presence of blue-absorbing aerosols is revealed by this test, atmospheric correction is based on the dust models proposed by (Moulin *et al.*, 2001a). This unique feature of the MERIS atmospheric corrections is not further discussed here (but see Nobileau and Antoine, 2005; Antoine and Nobileau, 2006).

2.3   The OCTS/GLI Algorithm

The OCTS/GLI algorithm shares its theoretical basis with that of SeaWiFS, although the implementation of the algorithm has some differences. The theoretical aspect of the algorithm is described in Fukushima *et al.* (1998), while the implementation details can be found in the NASDA-EOC (1997) document.

In the reflectance-based expression, the satellite-observed radiance $\rho_t(\lambda)$ is modelled as:

$$\rho_t(\lambda) = \rho_r(\lambda) + \rho_a(\lambda) + \rho_{ra}(\lambda) + t(\lambda)t_0(\lambda)[\rho_w(\lambda)]_N, \qquad (2.8)$$

where $\rho_r(\lambda)$ is Rayleigh reflectance, $\rho_a(\lambda)$ is the reflectance that would be observed if the atmosphere consisted of aerosol particles only, ρ_{ra} is the Rayleigh-aerosol interaction term, $[\rho_w(\lambda)]_N$ is the normalized water-leaving reflectance (i.e., $\rho_w(\lambda)/t_0(\lambda)$), and $t_0(\lambda)(t(\lambda))$ is the transmittance between sun and the ocean surface (between satellite and the ocean surface). Note that, for simplicity, sun glitter reflectance and whitecap reflectance are omitted from the equation.

The transmittance $t(\lambda)$ (or similarly $t_0(\lambda)$) is expressed as a product of Rayleigh transmittance $t_r(\lambda)$, absorptive gaseous transmittance $t_{oz}(\lambda)$ and aerosol transmittance $t_a(\lambda)$, where $t_r(\lambda)$ and $t_{oz}(\lambda)$ are easily given. In the OCTS algorithm, t_a is modelled as:

$$t_a(\lambda) = \exp\left[-\{1 - \omega_a(\lambda)\eta(\lambda)\}\tau_a / \cos\theta\right], \tag{2.9}$$

where ω_a is the aerosol single scattering albedo, η is the aerosol forward scattering probability, and θ is the satellite zenith angle. In the evaluation of t_a, the OCTS algorithm assumes η is unity while ω_a is determined through the atmospheric correction process.

In Equation 2.8, $\rho_r(\lambda)$ is determined accurately by theory. Assuming that $[\rho_w(\lambda)]_N$ in the NIR bands are negligible, $\rho_a(\lambda) + \rho_{ra}(\lambda)$ can be obtained in the NIR bands. Following the standard scheme for ocean-colour atmospheric correction described in this report, the OCTS algorithm, in essence, estimates $\rho_a(\lambda) + \rho_{ra}(\lambda)$ in the visible bands based on the observed $\rho_a(\lambda) + \rho_{ra}(\lambda)$ in the red and NIR bands (i.e. 670 and 865 nm).

Similar to the SeaWiFS algorithm, a set of 10 aerosol models are defined (the SeaWiFS algorithm uses 12 models). The first 9 models are: 'Tropospheric' models with a RH of 50%, 80% and 90%, 'Coastal' models with the same set of RH, and 'Maritime' models with a RH of 50%, 80%, and 98%, all defined based on the aerosol models described in Shettle and Fenn (1979). The last one, 'Asian dust' aerosol is defined based on the ground-level observation in an Asian dust event (Nakajima *et al.*, 1989), although the model was rarely used because of its extremely low epsilon values, i.e. Equation 2.6

The method for estimating $\rho_a(\lambda) + \rho_{ra}(\lambda)$ in the visible bands from the NIR observed aerosol reflectance is almost the same as for the SeaWiFS algorithm, but instead of relating $\rho_a(\lambda) + \rho_{ra}(\lambda)$ to $\rho_{as}(\lambda)$, it is assumed that $\rho_a(\lambda) + \rho_{ra}(\lambda)$ for each aerosol model M, wavelength, and scan geometry, can be given as a function of aerosol optical thickness, τ_a, as follows:

$$
\begin{aligned}
\rho_a(M,\lambda) + \rho_{ra}(M,\lambda) = {} & a_1(M,\lambda,\theta,\theta_0,\Delta\phi)\tau_a(M,\lambda) \\
& + a_2(M,\lambda,\theta,\theta_0,\Delta\phi)\tau_a^2(M,\lambda) \\
& + a_3(M,\lambda,\theta,\theta_0,\Delta\phi)\tau_a^3(M,\lambda),
\end{aligned} \tag{2.10}
$$

where θ and θ_0 are satellite-zenith and solar-zenith angles, respectively, and $\Delta\phi$ is satellite azimuth angle relative to sun. LUTs are generated for $a_i(M,\lambda,\theta,\theta_0,\Delta\phi)$ for every few degrees of $\theta, \theta_0, \Delta\phi$ for an appropriate set of τ_a values for every aerosol type M, by conducting a series of radiative transfer simulation with the Rstar5b code (Nakajima and Tanaka, 1988). In processing actual satellite data, the values of a_i for given $\theta, \theta_0, \Delta\phi$ are derived from 3-dimensional Lagrangian interpolation of the table entries.

In addition to the aerosol LUTs, auxiliary aerosol lookup tables are used for single scattering albedo, extinction coefficient (K_{ext}), and phase function for every

aerosol model M, in addition to a Rayleigh reflectance lookup table, which was generated through a series of vector radiative transfer simulations.

Given $\rho_a(\lambda) + \rho_{ra}(\lambda)$ at 670 and 865 nm bands, the algorithm calculates aerosol optical thickness, τ_a, at these bands, assuming each one of the aerosol models by solving the cubic Equation 2.10. Then, a model-wise ratio of $\tau_a(M, 670)$ to $\tau_a(M, 865)$, or

$$\gamma_E(670, 865) = \frac{\tau_A(670)}{\tau_A(865)}, \tag{2.11}$$

where 'E' denotes 'estimated' is calculated to produce 'average γ_E'. This γ_E is compared with 'theoretical γ' for each model

$$\gamma_T(M, 670, 865) = \frac{K_{ext}(M, 670)}{K_{ext}(M, 865)}, \tag{2.12}$$

and a pair of aerosol models which have the closest γ_T to γ_E average is selected. Using the aerosol lookup table for a_i in Equation 2.10, $\rho_a(\lambda) + \rho_{ra}(\lambda)$ values for the selected two aerosol models are obtained for each visible band and used for interpolation to determine the final $\rho_a(\lambda) + \rho_{ra}(\lambda)$ to estimate $tt_0\rho_w$. The aerosol single scattering albedo ω_a, which is necessary for evaluation of aerosol transmittance, is determined from the aerosol model pair selected for that pixel. This completes the pixel-wise OCTS atmospheric correction.

The GLI algorithm is based on the OCTS algorithm described above but with some enhancements. The earlier version (Version 1.5) of the GLI atmospheric correction algorithm has a slightly different aerosol model set with no Asian dust model included. It incorporates a bio-optical model and a neural network (Tanaka *et al.*, 2004) to determine iteratively the magnitude of $[\rho_w(\lambda_{NIR})]_N$, which considers the effect of inorganic suspended matter as well as phytoplankton. Version 2.1 of this algorithm introduces an empirical iterative scheme for absorptive aerosol correction. The algorithm description can be found in NASDA-EOC (2004) and Toratani *et al.* (2007), while Murakami *et al.* (2006) and Fukushima *et al.* (2007) evaluated the performance of the algorithm in comparison with *in situ* data.

2.4 The POLDER Algorithm

The general idea of the algorithm is to use spectral bands in which ocean reflectance is very low to assess aerosol quantity (optical thickness) and quality (Ångström coefficient and model). This information is then extrapolated to ocean-colour bands to correct the TOA signal from atmospheric perturbations. As in Gordon and Wang (1994a), the aerosol inversion relies on models developed by Shettle and Fenn (1979). In situations of eutrophic or Case-2 waters, the algorithm takes into account the non-negligible ocean reflectance in the red. The algorithm also deals with absorbing aerosols by exploiting directional information. These features, however, were not implemented to produce the results discussed in Chapters 4 and 5 of this report.

The core of the algorithm is a two-step iterative process. In the first step, the aerosol model is determined for a given optical thickness. In the second step, the optical thickness is computed for the model inverted in the first step. Because of multiple scattering effects, the two steps are run twice. The atmospheric correction of the ocean-colour bands is then carried out using the aerosol model and optical thickness inverted in the previous steps. Specific operations are implemented for sun-glint and whitecap correction and are discussed in detail in Appendix A.

Aerosols families are defined to deal with absorbing aerosols, ranging from a non-absorbing aerosol family to a highly absorbing one. The idea is to run the core of the algorithm for each family (one family is made of 12 aerosol models), and then to select the family that best fits directional observations.

The algorithm relies heavily on exact simulation of the TOA radiances for each pixel and viewing direction, and for multiple geophysical conditions, including polarization effects from molecules and aerosols scattering. The simulations are CPU-consuming and are incompatible with global data set processing. For that reason, lookup tables are computed beforehand. The simulated data are then linearly interpolated over multiple variables (solar and sensor viewing angles, aerosol models, optical thicknesses).

Solar zenith angle, view zenith angle and relative azimuth angle are available for each pixel and each viewing direction in the Level-1 product. Precision is sufficient for the solar zenith angle (there is a lapse of about four minutes between the first and the last sequence for an observed spot on Earth from POLDER), but for the viewing zenith angle and relative azimuth angle a fine geometric registration correction is computed for each band, to account for the small lapse of 0.306 seconds between measurements in the two different bands. The measurements are then associated with a geometry exactly defined by a triplet $[\theta_0(i), \theta(\lambda_j, i), \phi(\lambda_j, i)]$, where λ_j is the wavelength of band j, and i is the index of viewing direction. Further details of the POLDER algorithm are provided in Appendix A.

Simulated Testing Data Set

Menghua Wang, Howard R. Gordon and André Morel

To test the various atmospheric correction algorithms, a pseudo-TOA data set was generated using the radiative-transfer simulation for the ocean-atmosphere system. In generating the TOA data set, it was assumed that the radiative-transfer processes for ocean and atmosphere are decoupled, i.e., processes such as photons scattered from ocean water then scattered back into the water, and backscattered out again, are ignored. Therefore, the TOA atmospheric path radiance and water-leaving radiance can be computed separately. For a fair comparison, the radiative-transfer code for generating pseudo-TOA atmospheric path radiance is different from all the codes used for generating the lookup tables for the atmospheric correction algorithms.

3.1 The TOA Atmospheric Path Radiance

3.1.1 Radiative-Transfer Code

The forward Monte-Carlo vector radiative-transfer code was used to generate the TOA atmospheric path radiance $L_{\text{path}}(\lambda)$ as in Equation 2.2. The forward Monte-Carlo code was developed by Ding and Gordon based on their backward Monte-Carlo code (Ding and Gordon, 1994) and subsequently modified to include the polarization effects. Typically, the Monte-Carlo code can produce the TOA path radiance within an uncertainty of $<\sim 0.1\%$. The simulations were carried out for a two-layer plane-parallel atmosphere (PPA) model with 78% of molecules occupying the top layer (aerosols mixed with 22% of molecules confined in the bottom layer), overlying a flat Fresnel-reflecting ocean surface (black ocean). The PPA model is generally valid for the solar and sensor zenith angles $<\sim 80°$, and the effects of the aerosol vertical distribution on results of the atmospheric correction are negligible for non- and weakly-absorbing aerosols. The TOA atmospheric path radiances, $L_{\text{path}}(\lambda)$, were simulated to include polarization effects. For each Monte-Carlo run, 15 million photons were used to reduce the noise. Results show that, using the 15 million photons, the random noise in the Monte-Carlo simulation is generally within $\sim 0.05\%$. In addition, the Monte-Carlo results were compared with those from the vector

successive order of scattering (SOS) code (Gordon and Wang, 1992) for various cases. They generally agreed with one another to within ~0.3%, and differences in the reflectance within ~5×10^{-4}.

3.1.2   Aerosol Models

The 'Maritime' aerosol model with a RH of 80% (M80) was used for generating the pseudo-TOA atmospheric path radiance $L_{\text{path}}(\lambda)$. The M80 model (not used in the look-up tables generated by the various algorithms) represents weakly-absorbing aerosols in the open ocean with a single-scattering albedo of 0.99 at 865 nm. The aerosol optical thickness (at 865 nm) used for the M80 model is 0.05, 0.1, and 0.2. In addition, the 'Urban' model from Shettle and Fenn (1979), with a RH of 80% (U80), was used for $L_{\text{path}}(\lambda)$ generation to test the algorithm performance for strongly absorbing aerosols. For the U80 model, the single-scattering albedo was 0.75, and an aerosol optical thickness of 0.1 was used (at 865 nm). Table 3.1 summarizes all the parameters and models used for computation of the TOA atmospheric path radiances, $L_{\text{path}}(\lambda)$.

Table 3.1   Parameters and models for generating the TOA atmospheric path radiance $L_{\text{path}}(\lambda)$.

Radiative Transfer Code	Forward Monte-Carlo (Vector)
Atmospheric Model	Two-layer plane-parallel atmosphere with 78% molecules at the top and aerosols mixed with 22% molecules at the bottom
Ocean Surface	A flat Fresnel-reflecting ocean surface
Photons used for Each Monte-Carlo Run	15 million
Aerosol Models	Maritime RH=80%, Urban RH=80%
Aerosol Optical Thickness at 865 nm	M80: 0.05, 0.1, and 0.2; U80: 0.1
Wavelengths (nm)	412, 443, 490, 555, 670, 708, 765, 779, 865
Solar-Zenith Angles	0°, 45°, 60°, 65°, 70°, 78°
Sensor-Zenith Angles	5°, 25°, 45°, 55°, 65°
Relative Azimuth Angle	90°

3.2   The Ocean Water Radiance Contributions

The ocean radiance contributions for both the Case-1 and Case-2 waters, which were used for the pseudo-TOA radiance computations ($[L_w(\lambda)]_N$ component in Equation 2.1, or equivalently $[\rho_w(\lambda)]_N$), are described below.

3.2.1 Case-1 Water

Representative normalized water-leaving reflectance spectra for Case-1 waters were derived using a semi-analytic model (Gordon, *et al.*, 1988b). Briefly, in the Gordon *et al.* (1988b) model the normalized water-leaving reflectance $[\rho_w(\lambda)]_N$ is given by

$$[\rho_w(\lambda)]_N = \pi \left[\frac{(1-\rho)(1-\bar{\rho})}{m^2} \right] \left[\frac{1}{(1-rR)} \right] \frac{R}{Q}, \qquad (3.1)$$

where ρ is the Fresnel reflectance of the sea surface at normal incidence, $\bar{\rho}$ is the Fresnel reflectance for irradiance from the sun and sky, m is the refractive index of water, R is the irradiance reflectance just beneath the surface, r is the water-to-air surface reflectance for diffuse light ($r \approx 0.48$), and $Q = E_u/L_u$, with E_u the upwelling irradiance just beneath the sea surface and L_u the upwelling radiance in the same position propagating toward the zenith. A nominal value of Q is π, the value assuming a totally diffuse upwelling light field. The quantity R/Q can be related to the inherent optical properties of the water through

$$\frac{R}{Q} \approx 0.0949 \frac{b_b}{a+b_b}, \qquad (3.2)$$

where the absorption coefficient of the medium is given by $a = a_w + a_c$ and the backscattering coefficient by $b_b = (b_b)_w + (b_b)_c$, where the subscripts 'w' and 'c' refer to water and its constituents, respectively. It has been shown (Gordon, *et al.*, 1975) that the sum $a + b_b$ can be related to the attenuation coefficient of downwelling irradiance K just beneath the water surface through

$$K \approx 1.16(a+b_b), \qquad (3.3)$$

so Equation 3.2 becomes

$$\frac{R}{Q} \approx 0.11 \frac{b_b}{K}. \qquad (3.4)$$

In the Gordon *et al.* (1988b) model, K is divided according to $K = K_w + K_C + K_{ys}$, where the subscripts 'w', 'C', and 'ys' stand for water, chlorophyll, and yellow substance, respectively. Although this separation is not quite correct because K cannot be rigorously summed over constituents, Gordon (1989) has nevertheless shown that for most purposes this approximation is a valid approximation. The spectral values of K_w are taken from Smith and Baker (1978) and K_C from Smith and Baker (1981). K_{ys} is taken to be zero here. This is equivalent to assuming that any background yellow substance is accounted for in K_C.

The backscattering coefficient of the constituents (phytoplankton) is written as

$$(b_b)_c = A(\lambda)C^{B(\lambda)}, \qquad (3.5)$$

where C is the chlorophyll concentration. The coefficients $A(\lambda)$ and $B(\lambda)$ were chosen in a manner that provided the best fit to the spectral radiance data collected

by Clark (1981). Given these quantities, R/Q in Equation 3.2 is determined as a function of C. Then assuming $Q = \pi$ (the value for a totally diffuse upwelling light field), R is determined for the computation of $(1 - rR)$. These are then inserted into Equation 3.1 providing $[\rho_w(\lambda)]_N$ as a function of C. Figure 3.1a shows the normalized water-leaving reflectance $[\rho_w(\lambda)]_N$ as a function of the wavelength for chlorophyll concentrations of 0.03, 0.1, 0.3, and 1.0 mg/m^3. These spectra should be representative of those in typical Case-1 waters and sufficiently accurate for the purpose of this atmospheric correction study.

3.2.2   Case-2 Water Examples

Two examples of the ocean contributions from Case-2 waters, which correspond to typical sediment-dominated and yellow substance dominated waters, are used for the pseudo-TOA radiance computations.

The first example corresponds to sediment-dominated Case-2 waters. It is derived from actual irradiance measurements (upward and downward irradiances just below the surface, E_u and E_d), which were performed at a station off Cap Corveiro (Morocco-Mauritania, Station #16, 16 March 1974 at 17°03 W, 21°47.5 N, water depth 37 m) during the CINECA-5 cruise (Cooperative Investigation of the NE Central Atlantic, a sub-program of the CUEA, Coastal Upwelling Ecosystems Analysis). The high particle load resulted from the re-suspension of bottom sediments due to wave action generated by strong trade winds. The scattering coefficient, $b(\lambda)$, at 550 nm was between 3.1 and 3.9 m^{-1}, and the chlorophyll concentration ranged from 1.1 to 1.9 mg m^{-3}. Such turbid milky waters were encountered along this arid coast within a strip delimited by the shoreline and the 40 or 50 m isobaths (Morel, 1982).

The second example is typical of yellow substance dominated Case-2 water. The irradiance ratio, $R = E_u/E_d$, was determined in Saanich inlet (Sidney, Vancouver Island, BC, Canada) on 7 August 1979. The water was dark brownish, almost black with $b(550)$ around 1.2 m^{-1} and chlorophyll about 4.5 mg m^{-3}. The high yellow substance content of terrigenous origin originated from the drainage of the forest soil.

For both examples, the irradiance reflectance, $R(\lambda)$, was transformed into normalized water-leaving reflectance $[\rho_w(\lambda)]_N = R(\lambda)F_0(\lambda)(\Re_0/Q_0)$ (see Appendix D). Figure 3.1b provides the normalized water-leaving reflectance $[\rho_w(\lambda)]_N$ as a function of the wavelength for sediment-dominated water observed off the Mauritanian coast and yellow substance-dominated water acquired from an inlet in Vancouver Island. Table 3.2 summarizes model and data used for computations of the ocean normalized water-leaving reflectance $[\rho_w(\lambda)]_N$ (or radiance $[L_w(\lambda)]_N$).
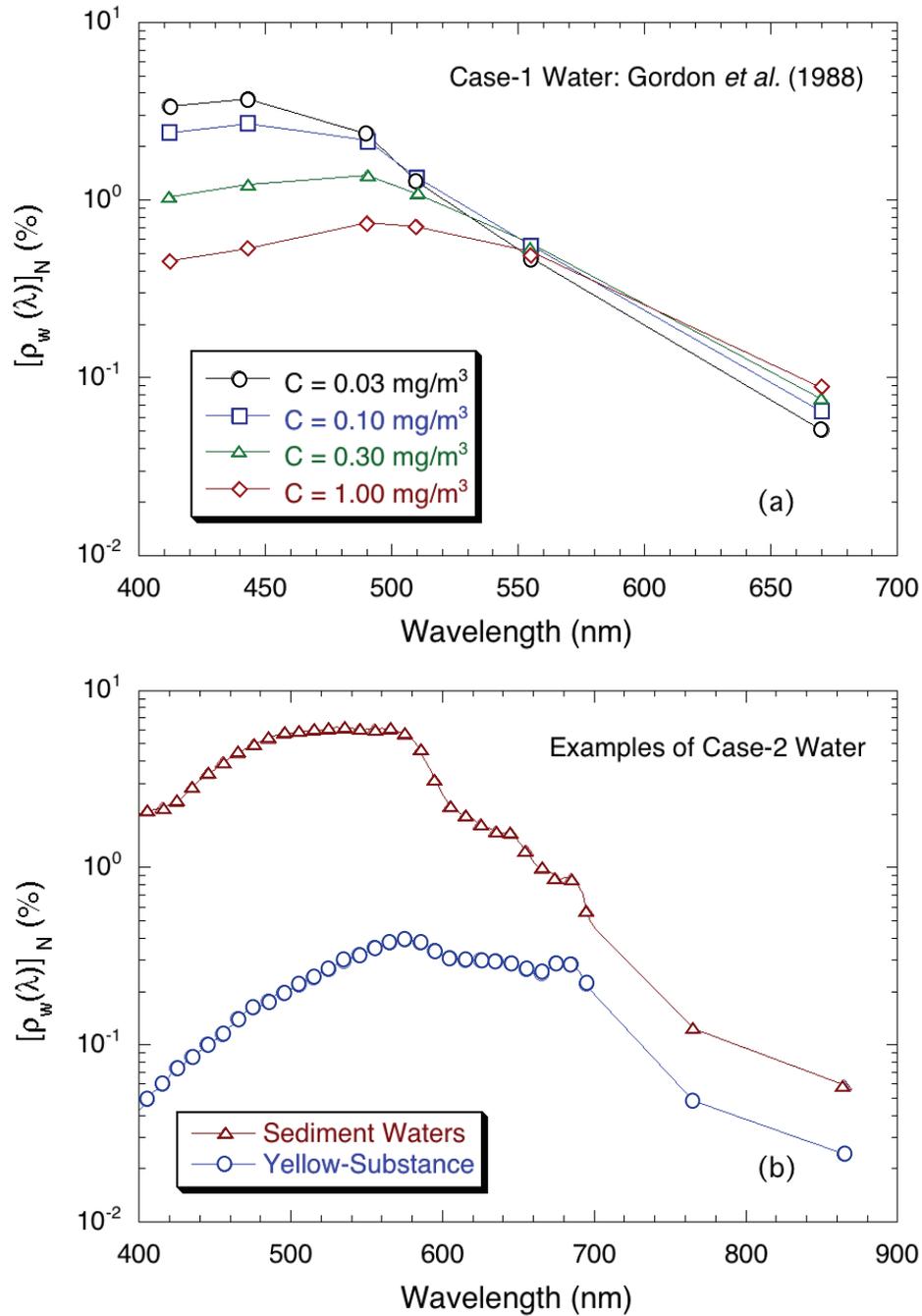
Figure 3.1 Examples of the ocean normalized water-leaving reflectance $[\rho_w(\lambda)]_N$ as a function of the wavelength for (a) Case-1 waters for chlorophyll concentrations of 0.03, 0.1, 0.3, and 1.0 mg/m^3 and (b) Case-2 waters for sediment-dominated water observed off the Mauritanian coast, and yellow substance-dominated water acquired from an inlet in Vancouver Island, respectively. Note that reflectance values at 749, 765 and 865 nm are null for the Case-1 waters.

Table 3.2 Parameters for generating ocean normalized water-leaving radiance $[L_w(\lambda)]_N$.

Case-1 Waters	Case-2 Waters
Model data: Gordon *et al.* (1988b) semianalytic model	Two examples from measurements
Chlorophyll concentrations: 0.03, 0.1, 0.3, and 1.0 mg/m^3	Sediment-dominated: Data from the Mauritanian coast
Black ocean assumed for wavelengths > 670 nm	Yellow substance-dominated: Data from an inlet in Vancouver Island

3.3 The TOA Radiance Data Set

With the simulated TOA atmospheric path radiance $L_{\text{path}}(\lambda)$ and the modelled (or observed) ocean water contributions $[L_w(\lambda)]_N$, the TOA radiance $L_t(\lambda)$ as in Equation 2.1 can be computed by ignoring both $L_{wc}(\lambda)$ and $L_g(\lambda)$ terms, i.e.,

$$L_t(\lambda) = L_r(\lambda) + L_a(\lambda) + L_{ra}(\lambda) + t(\lambda)t_0(\lambda)\cos\theta_0[L_w(\lambda)]_N, \qquad (3.6)$$

where terms $t_0(\lambda)$ and $t(\lambda)$ are calculated according to Yang and Gordon (1997) with appropriate aerosol models (M80 or U80). The contributions of $L_{wc}(\lambda)$ and $L_g(\lambda)$ are ignored because the algorithm performance comparisons are focusing on the aerosol corrections. In addition, the term $L_g(\lambda)$ is generally masked out, while the $L_{wc}(\lambda)$ contribution was found to be less important than originally expected (Gordon and Wang, 1994b; Moore *et al.*, 2000).

Figure 3.2 shows some examples of the simulated TOA reflectance $\rho_t(\lambda)$ as a function of the wavelength for various cases. Figure 3.2a provides examples of the simulated $\rho_t(\lambda)$ for three typical water types, i.e., Case-1 water with a chlorophyll concentration of 0.1 mg/m^3, sediment-dominated water (Case-2), and yellow substance-dominated water (Case-2), for the M80 aerosols with aerosol optical thickness at 865 nm ($\tau_a(865)$) of 0.1, while Figures 3.2b–d provide the TOA total reflectance $\rho_t(\lambda)$ and the Rayleigh reflectance contribution $\rho_r(\lambda)$, as well as a more detailed reflectance contribution partition for each of these three cases. These are all for a case of the solar-zenith angle of 60°, sensor-zenith angle of 45°, and relative-azimuth angle of 90°. The right side of Figures 3.2b–d show the scale for the reflectance ratio value indicated in the plot. For example, results in Figure 3.2b show that, for the case of the M80 model with $\tau_a(865)$ of 0.1 and with chlorophyll concentration of 0.1 mg/m^3, the TOA atmospheric path reflectance $\rho_{\text{path}}(\lambda)$ contributes about 93.6%, 90.2%, 87.9%, 89.2%, 94.5% and 98.7% in the TOA reflectance for wavelengths at 412, 443, 490, 510, 555, and 670 nm, respectively. In other words, the corresponding TOA water-leaving reflectance $t(\lambda)\rho_w(\lambda)$ contributes about 6.4%, 9.8%, 12.1%, 10.8%, 5.5%, and 1.3% in the TOA reflectance at these wavelengths. On the other hand, for the sediment-dominated waters, Figure 3.2c shows that the TOA water-leaving reflectance contributes about 5.8%, 11.8%, 26.3%, 30.6%, 39.0%,
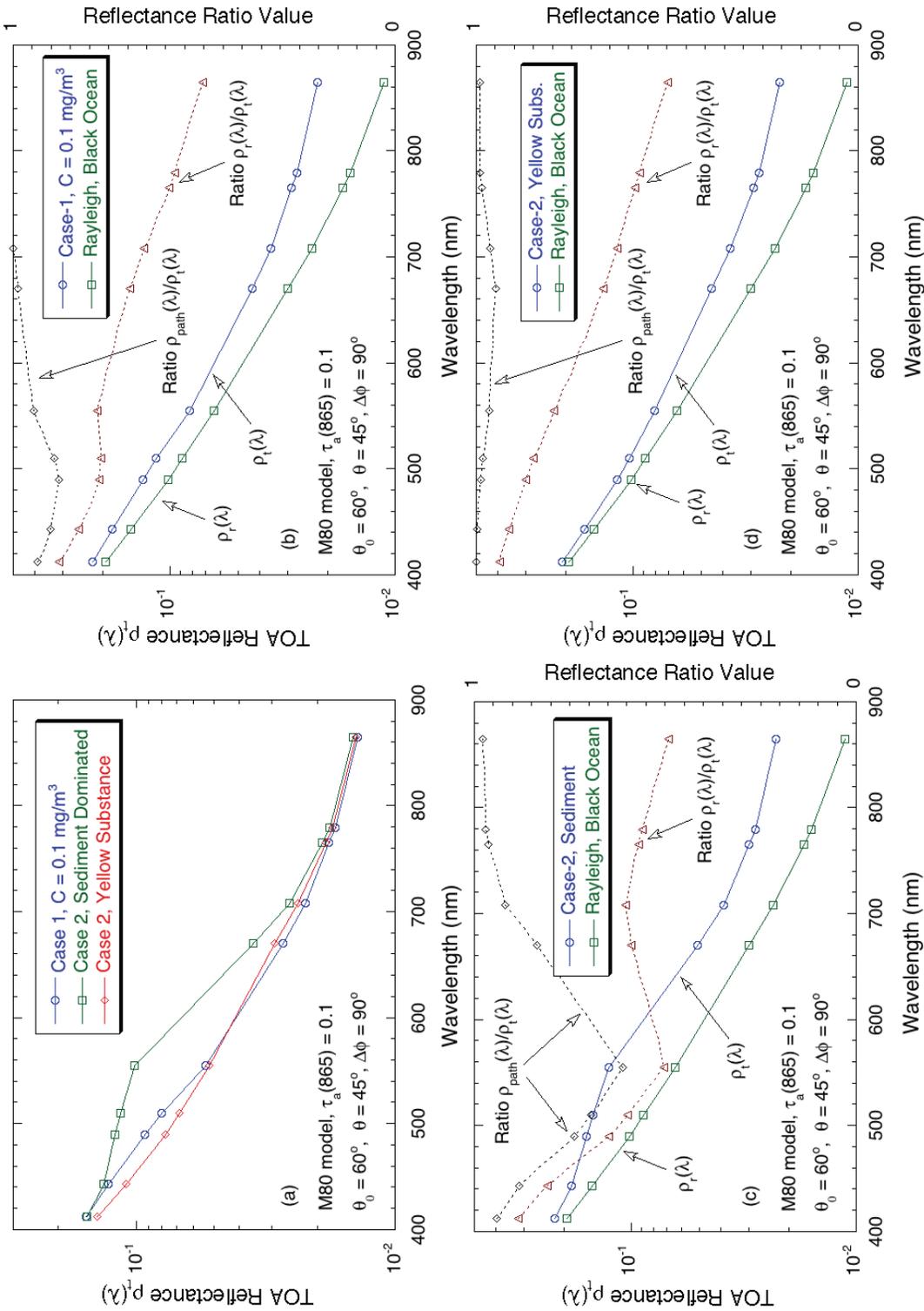
Figure 3.2 Examples of the simulated TOA reflectance $\rho_t(\lambda)$ (testing data set) as a function of the wavelength for the M80 aerosol model with $\tau_a(865)$ of 0.1 and for (a) cases with both Case-1 and Case-2 waters, (b) Case-1 water with chlorophyll concentration of 0.1 mg/m³, (c) Case-2 with sediment-dominated waters, and (d) Case-2 with yellow substance-dominated waters. Plots (b)–(d) also present results of ratio values for $\rho_{path}(\lambda)/\rho_t(\lambda)$ and $\rho_r(\lambda)/\rho_t(\lambda)$ (scaled on the right side).

16.4%, 8.2%, 3.7%, 3.0%, and 2.4% in the TOA reflectance for wavelengths at 412, 443, 490, 510, 555, 670, 708, 765, 779, and 865 nm, respectively, while for the yellow substance-dominated waters Figure 3.2d shows that these values are reduced dramatically to 0.2%, 0.4%, 1.2%, 1.7%, 3.6%, 5.3%, 3.8%, 1.5%, 1.2%, and 1.0%, respectively.

Results in Figure 3.2 demonstrate that the ocean contributions comprise only a small portion of the sensor-measured signals in the visible wavelengths. This is especially the case for the waters dominated by yellow substances. Therefore, for such waters sufficiently accurate atmospheric correction in the blue and green bands is extremely difficult, if not impossible. Results in Figure 3.2 also indicate the importance of the vicarious calibration for ocean-colour remote sensing. It requires a calibration accuracy of ~0.1%. Examples of the Case-2 waters in Figure 3.2c and Figure 3.2d also show that the NIR black ocean assumption is not valid for these ocean waters (Siegel, *et al.*, 2000; Wang and Shi, 2005).

The simulated TOA reflectance $\rho_t(\lambda)$ (or radiance $L_t(\lambda)$) spectra are used as inputs for testing the performance of the various atmospheric correction algorithms.

Chapter 4

Comparison Results

Menghua Wang, David Antoine, Robert Frouin, Howard R. Gordon, Hajime Fukushima, André Morel, Jean-Marc Nicolas and Pierre-Yves Deschamps

With inputs of the pseudo-TOA reflectance $\rho_t(\lambda)$ for various atmosphere and ocean cases, the performance of various atmospheric correction algorithms is evaluated. Specifically, results are compared with the 'true' normalized water-leaving radiance $[L_w(\lambda)]_N$ at 443, 490, and 555 nm, and radiance ratio values of $[L_w(443)]_N/[L_w(555)]_N$ and $[L_w(490)]_N/[L_w(555)]_N$ for Case-1 (Table 4.1) and Case-2 (Table 4.2) waters. Some example results of the retrieved aerosol optical thickness (AOT) data from the four algorithms for typical Case-1 waters are also provided and discussed in the following sections. Note that $[L_w(\lambda)]_N$ data at 412 nm are not included because POLDER does not have a 412 nm band.

Table 4.1 True water parameters for Case-1 waters.

Parameter	Case-1 Water with Pigment Concentration C in mg/m³			
	0.03	**0.1**	**0.3**	**1.0**
$[L_w(443)]_N{}^\dagger$	2.309	1.668	0.761	0.333
$[L_w(490)]_N{}^\dagger$	1.510	1.398	0.886	0.483
$[L_w(555)]_N{}^\dagger$	0.283	0.335	0.344	0.306
$[L_w(490)]_N/[L_w(555)]_N$	8.174	4.978	2.212	1.088
$[L_w(490)]_N/[L_w(555)]_N$	5.344	4.173	2.574	1.578

† Units mW cm^{-2} μm^{-1} sr^{-1}

4.1 The Open Ocean (Case-1 Waters)

4.1.1 Ocean-Colour Parameters

Figure 4.1 provides some examples of the results of algorithm performance for a typical Case-1 water with maritime aerosols. Results in Figure 4.1 are ratio values (derived/true) of various ocean-colour parameters as a function of the air mass,
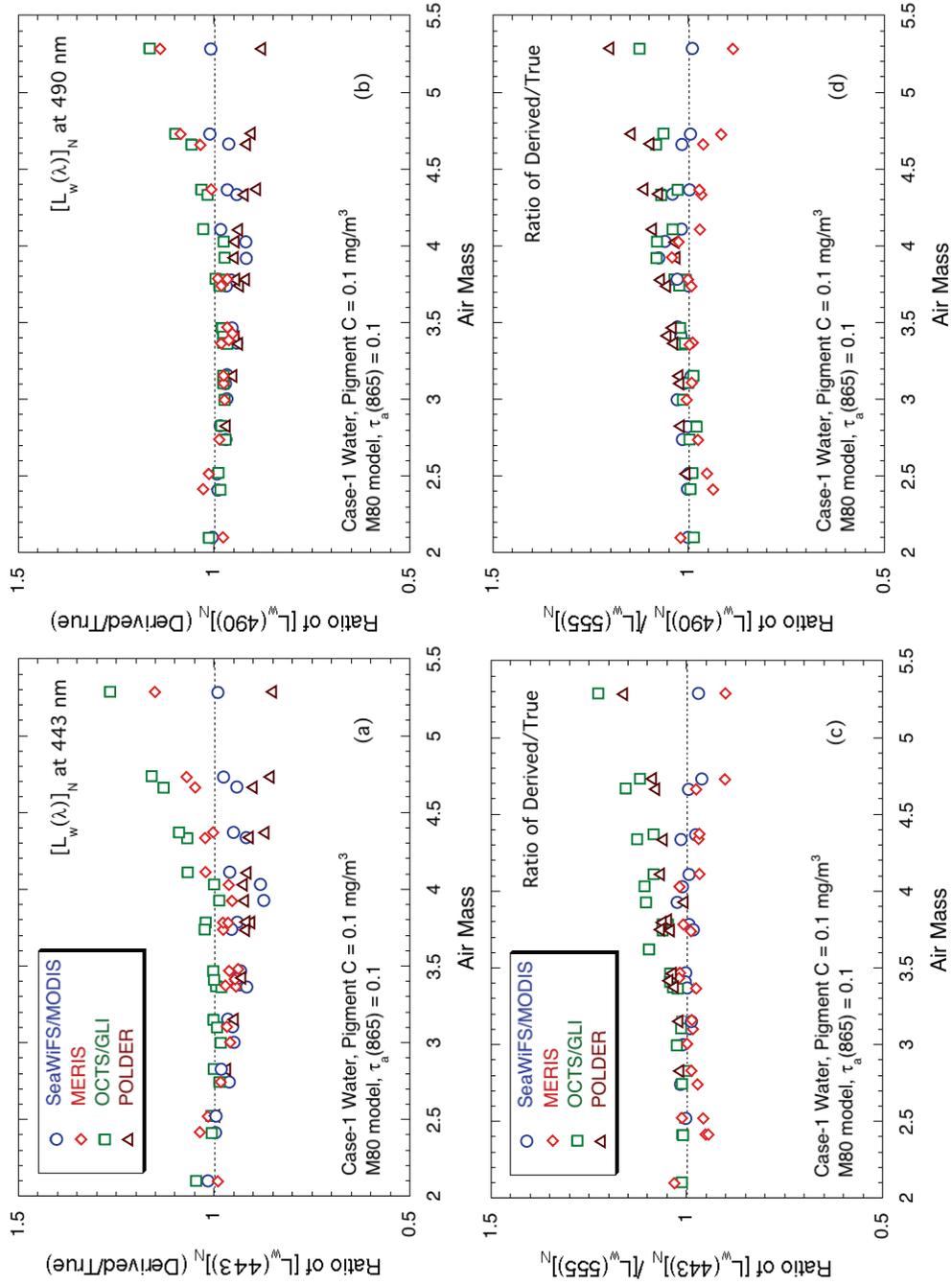
Figure 4.1 Ratio values (derived/true) of various ocean-colour parameters as a function of the air mass from atmospheric correction algorithms of SeaWiFS/MODIS, MERIS, OCTS/GLI, and POLDER for (a) $[L_w(\lambda)]_N$ at 443 nm, (b) $[L_w(\lambda)]_N$ at 490 nm, (c) ratio $[L_w(443)]_N/[L_w(555)]_N$, and (d) ratio $[L_w(490)]_N/[L_w(555)]_N$. These results are for the M80 aerosols with aerosol optical thickness of 0.1 at 865 nm and for open ocean (Case-1) water with pigment concentration of 0.1 mg/m^3.

Table 4.2   True water parameters for Case-2 waters.

Parameter	Case-2 Waters	
	Sediment Dominated Water	Yellow Substance Dominated Water
$[L_w(443)]_N$[†]	2.053	0.061
$[L_w(490)]_N$[†]	3.619	0.123
$[L_w(555)]_N$[†]	3.650	0.224
$[L_w(443)]_N/[L_w(555)]_N$	0.562	0.272
$[L_w(490)]_N/[L_w(555)]_N$	0.991	0.550

[†] Units mW cm^{-2} μm^{-1} sr^{-1}

which is defined as air mass = $1/\cos\theta_0 + 1/\cos\theta$, from atmospheric correction algorithms of SeaWiFS/MODIS, MERIS, OCTS/GLI, and POLDER, respectively. Figures 4.1a and Figure 4.1b are for the ratio of the derived normalized water-leaving radiance $[L_w(\lambda)]_N$ at wavelengths of 443 and 490 nm, while Figure 4.1c and Figure 4.1d are the radiance ratio values of $[L_w(443)]_N/[L_w(555)]_N$ and $[L_w(490)]_N/[L_w(555)]_N$, respectively. These results are for the M80 aerosols with aerosol optical thickness of 0.1 at 865 nm and for open ocean water (Case-1) with a chlorophyll concentration of 0.1 mg/m^3. Results show that, overall, all four atmospheric correction algorithms performed quite well for cases with moderate air mass values. Some quantitative comparisons in statistics for typical open ocean cases are also provided in Table 4.3, which shows the mean and standard deviation (STD) values of the ratio (derived/true) values for various ocean-colour parameters ($[L_w(\lambda)]_N$ at wavelengths of 443, 490, and 555 nm, as well as radiance ratios for $[L_w(443)]_N/[L_w(555)]_N$ and $[L_w(490)]_N/[L_w(555)]_N$). The mean and STD values were derived for Case-1 waters with a chlorophyll concentration of 0.1 mg/m^3 and for cases with air mass values < 5.5. They are for the M80 aerosols with AOT at 865 nm of 0.05, 0.1, and 0.2. As expected, cases with large AOTs (e.g., 0.2) generally have larger uncertainties in the derived water-leaving radiance data. We have only listed results for various aerosol optical thicknesses with a global average chlorophyll concentration for open oceans because results of atmospheric correction depend strongly on the aerosol properties. Uncertainties for other Case-1 waters can be easily computed from Table 4.1 and Table 4.3, as the error in atmospheric correction is independent of $[L_w(\lambda)]_N$, e.g., ratio values for $[L_w(443)]_N$ with $C = 0.03$ mg/m^3 are closer to 1 than those with $C = 0.1$ mg/m^3, but ratios are lower for cases with $C = 0.3$ and 1.0 mg/m^3.

4.1.2   Aerosol Optical Thickness Results

In deriving the ocean-colour parameters from satellite-measured radiance spectra (as discussed in Chapter 2), the aerosol radiance contributions in the visible must be estimated accurately and removed (atmospheric correction). Therefore, ocean-colour
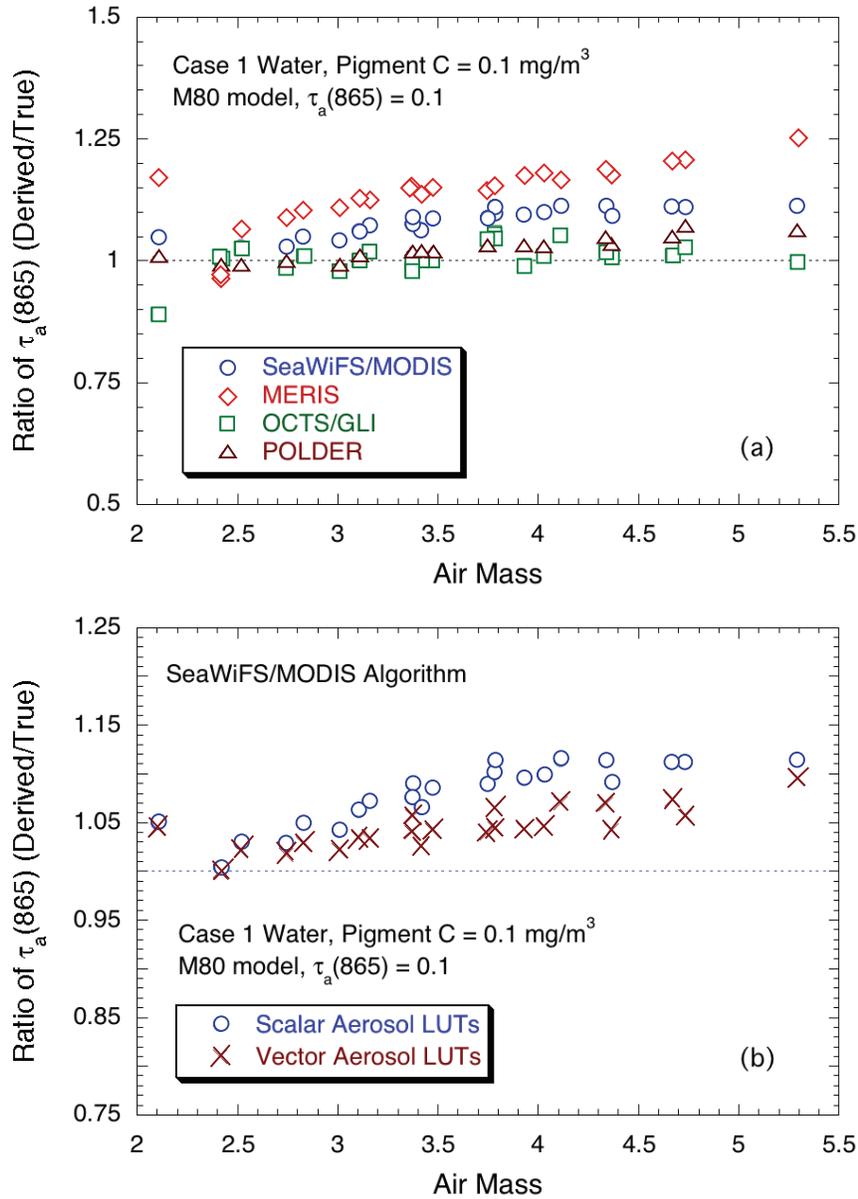
Figure 4.2   Ratio values (derived/true) of the AOT data at 865 nm as a function of the air mass from atmospheric correction algorithms of (a) SeaWiFS/MODIS, MERIS, OCTS/GLI, and POLDER and (b) comparison of the derived ratio in the AOT data for using the scalar and vector aerosol lookup tables (including polarization effects). These results are for the M80 aerosols with an aerosol optical thickness of 0.1 at 865 nm and for open ocean (Case-1) water with a chlorophyll concentration of 0.1 mg/m^3.

Table 4.3 Statistics (mean and standard deviation) for Case-1 water for various AOT data.

Parameter	C=0.1 mg/m^3 and for $\tau_a(865)$	Mean Ratio of Derived/True Value ± STD			
		SeaWiFS/MODIS	MERIS	OCTS/GLI	POLDER
$[L_w(443)]_N$	0.05	0.968±0.025	0.971±0.030	1.014±0.028	0.933±0.053
	0.10	0.966±0.027	0.998±0.047	1.036±0.067	0.940±0.044
	0.20	0.944±0.048	1.022±0.101	1.053±0.121	0.923±0.055
$[L_w(490)]_N$	0.05	0.975±0.018	0.983±0.022	0.989±0.018	0.948±0.040
	0.10	0.977±0.017	1.001±0.042	1.004±0.046	0.952±0.032
	0.20	0.961±0.037	1.017±0.089	1.009±0.086	0.930±0.046
$[L_w(555)]_N$	0.05	0.961±0.034	0.995±0.043	0.946±0.038	0.919±0.060
	0.10	0.955±0.043	1.020±0.083	0.978±0.033	0.906±0.069
	0.20	0.923±0.113	1.062±0.190	1.019±0.104	0.846±0.114
$[L_w(443)]_N/$ $[L_w(555)]_N$	0.05	1.008±0.019	0.976±0.022	1.073±0.057	1.016±0.018
	0.10	1.013±0.026	0.981±0.034	1.060±0.055	1.041±0.036
	0.20	1.035±0.098	0.973±0.064	1.034±0.054	1.104±0.098
$[L_w(490)]_N/$ $[L_w(555)]_N$	0.05	1.016±0.020	0.988±0.023	1.047±0.044	1.033±0.028
	0.10	1.025±0.033	0.985±0.037	1.028±0.038	1.055±0.050
	0.20	1.055±0.113	0.969±0.069	0.993±0.043	1.113±0.109
$\tau_a(865)$	0.05	1.130±0.091 1.036±0.016[†]	1.107±0.057	1.015±0.035	0.970±0.019
	0.10	1.075±0.034 1.042±0.022[†]	1.139±0.065	1.008±0.032	1.026±0.023
	0.20	1.061±0.024 1.043±0.018[†]	1.108±0.053	0.963±0.030	0.994±0.004

[†] Use the vector aerosol lookup tables.

satellite sensors can also give access to aerosol optical properties, in particular AOT. Figure 4.2 displays examples of evaluation results for the derived AOT. Figure 4.2a provides the resulting ratio values in the retrieved AOT (derived/true) from the four algorithms as a function of the air mass for a maritime aerosol (M80 model) with the AOT of 0.1 at 865 nm, and for Case-1 ocean water with a chlorophyll concentration of 0.1 mg/m^3. Some relatively larger errors for the case with air mass ~2 likely resulted from the effect of the glint contamination. Results in Figure 4.2a show that the AOT data derived from the POLDER and OCTS/GLI algorithms are quite accurate with uncertainties within ~5%, while both the SeaWiFS/MODIS and MERIS algorithms over-estimated the AOT data with uncertainties of ~10% for SeaWiFS/MODIS and ~15% for the MERIS algorithms. Overestimation of the AOT data for the SeaWiFS/MODIS algorithm (probably also for the MERIS algorithm) is partly due to the use of the scalar aerosol lookup tables, which do not include

polarization effects (Wang, 2006a). Note that the pseudo data were generated using the vector RTE. POLDER has used the vector aerosol lookup tables for the data processing in retrievals of ocean colour and aerosol parameters. Results in Figure 4.2b show that using the vector aerosol lookup tables, which include polarization effects, the SeaWiFS/MODIS-derived AOT data are improved, with uncertainties usually within ~5%, which is consistent with the results from Wang (2006a). Some detailed discussions for effects of the polarization on the other aerosol models, for example the T80 model, can be found in Wang (2006a).

Statistics (mean and STD) comparison results for the AOT at 865 nm of 0.05, 0.1, and 0.2 for the four operational algorithms, as well as for the SeaWiFS/MODIS algorithm using the vector aerosol lookup tables are presented in Table 4.3 (the last row). The OCTS/GLI and POLDER algorithms produced AOT products with uncertainties usually within ~3% (Table 4.3). Both SeaWiFS/MODIS and MERIS operational algorithms overestimate the AOT product for the M80 aerosols. With the vector aerosol lookup tables, however, the SeaWiFS/MODIS algorithm not only improves the bias error in the derived AOT, but also the noise error (STD values) is reduced significantly. It is worth noting that even though the AOT data are overestimated by SeaWiFS/MODIS and MERIS algorithms, both algorithms still derived accurate ocean-colour products. Wang (2006a) found that for aerosols with spectrally flat SSE (or Ångström exponent), e.g., maritime aerosols, ocean colour products can still be derived accurately even though the AOT data are overestimated. However, for aerosols with significant spectral variation in SSE, e.g., tropospheric aerosols, errors in the AOT data will result in relatively large uncertainties in the ocean colour products (Wang, 2006a). Thus, the comparison of AOTs does not necessary allow one to evaluate and compare the performance of the different atmospheric correction algorithms. Note that, for the open ocean, aerosols often exhibit spectrally flat SSE, while in coastal regions, aerosols with large spectral variation SSE are usually the case.

4.2 The Coastal Ocean Region (Case-2 Waters)

4.2.1 Sediment-Dominated Waters

Sample results for a Case-2 sediment-dominated water are shown in Figure 4.3. Presented similarly to Figure 4.1, this figure shows ratio values (derived/true) of various ocean-colour parameters as a function of the air mass for atmospheric correction algorithms of SeaWiFS/MODIS, MERIS, OCTS/GLI, and POLDER, and for a sediment-dominated Case-2 water as shown in Figure 3.1b. Figures 4.3a and b are for the ratio (derived/true) of the derived $[L_w(\lambda)]_N$ at wavelengths of 443 and 490 nm, while Figures 4.3c and d are the ratio (derived/true) of parameters $[L_w(443)]_N/[L_w(555)]_N$ and $[L_w(490)]_N/[L_w(555)]_N$, respectively. Overall all four atmospheric correction algorithms underestimated the $[L_w(\lambda)]_N$ values in the
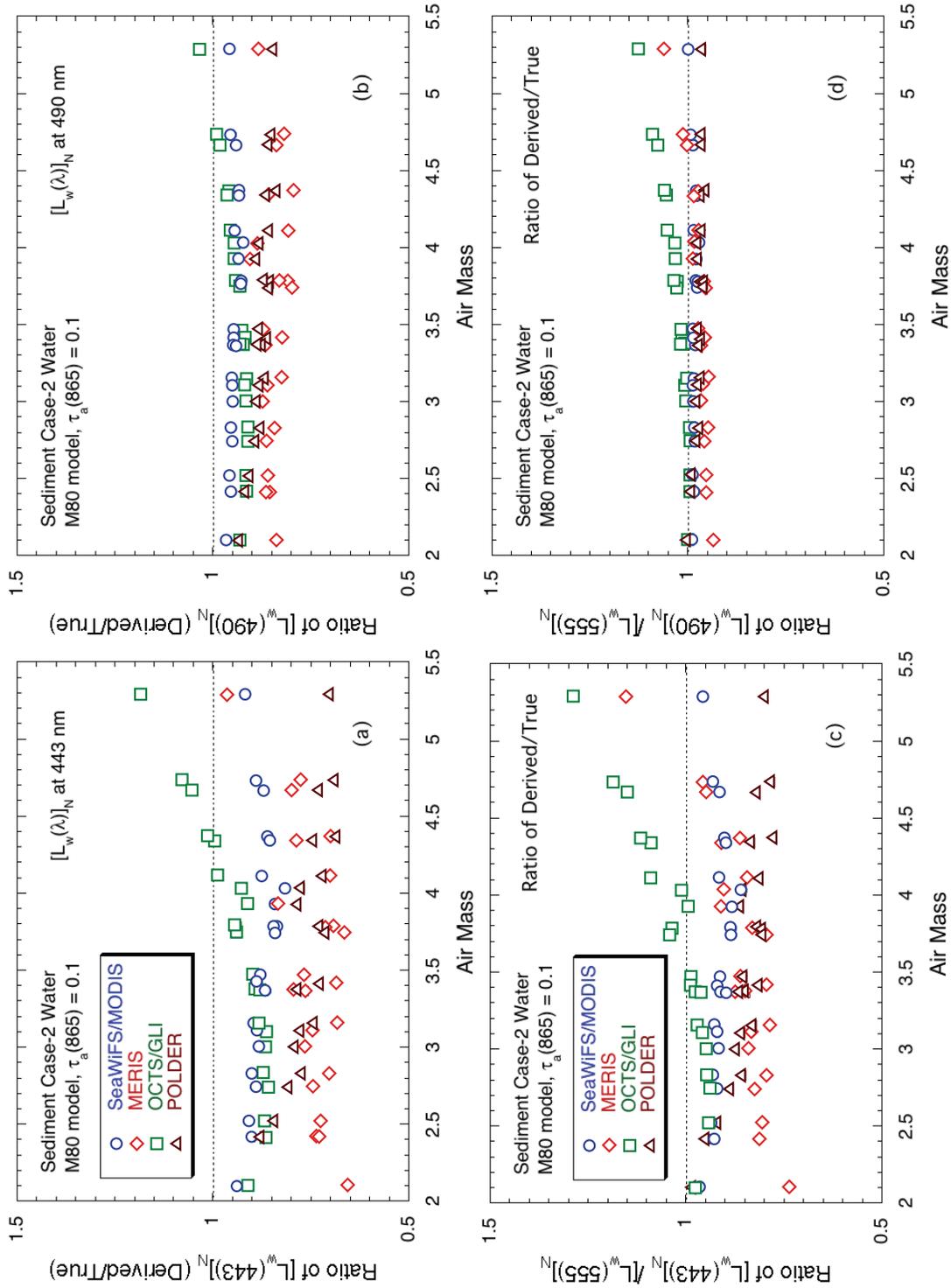
Figure 4.3 Ratio values (derived/true) of various ocean-colour parameters as a function of the air mass from atmospheric correction algorithms of SeaWiFS/MODIS, MERIS, OCTS/GLI, and POLDER for (a) $[L_w(\lambda)]_N$ at 443 nm, (b) $[L_w(\lambda)]_N$ at 490 nm, (c) ratio $[L_W(443)]_N/[L_W(555)]_N$, and (d) ratio $[L_w(490)]_N/[L_w(555)]_N$. These results are for the M80 aerosols with aerosol optical thickness of 0.1 at 865 nm and for a sediment-dominated Case-2 water.

visible (e.g., at wavelengths of 443 and 490 nm) due to the incorrect assumption in the estimation of the NIR ocean contributions. The biased error in the derived $[L_w(\lambda)]_N$ gets worse with the decrease of the wavelength, for example in the blue bands, because the extrapolation error in the aerosol contribution (biased high) increases with increase of wavelength difference from the NIR band. However, the radiance ratio values were derived relatively accurately for all four algorithms, in particular, for the parameter $[L_w(490)]_N/[L_w(555)]_N$. The coherent errors in the derived $[L_w(490)]_N$ and $[L_w(555)]_N$ cancel each other in the corresponding ratio value. This suggests that, for the current four operational atmospheric correction algorithms, it may be better to use the normalized water-leaving radiance ratios (particularly for $[L_w(490)]_N/[L_w(555)]_N$) for deriving the water properties for sediment-dominated Case-2 waters.

Table 4.4 Statistics (mean and standard deviation) for Case-2 sediment-dominated water for various AOT data.

Parameter	Case-2 Sediment Water and for $\tau_a(865)$	Mean Ratio of Derived/True Value ± STD			
		SeaWiFS/MODIS	MERIS	OCTS/GLI	POLDER
$[L_w(443)]_N$	0.05	0.874±0.027	0.778±0.057	0.904±0.047	0.749±0.062
	0.10	0.878±0.028	0.748±0.065	0.933±0.080	0.771±0.059
	0.20	0.869±0.043	0.650±0.182	0.956±0.116	0.768±0.057
$[L_w(490)]_N$	0.05	0.942±0.012	0.880±0.037	0.940±0.021	0.873±0.026
	0.10	0.945±0.011	0.848±0.030	0.939±0.030	0.880±0.023
	0.20	0.942±0.016	0.770±0.059	0.923±0.038	0.873±0.023
$[L_w(555)]_N$	0.05	0.961±0.008	0.911±0.033	0.928±0.007	0.901±0.014
	0.10	0.961±0.007	0.875±0.032	0.914±0.006	0.902±0.014
	0.20	0.959±0.007	0.796±0.048	0.885±0.011	0.894±0.014
$[L_w(443)]_N/$ $[L_w(555)]_N$	0.05	0.909±0.021	0.853±0.039	0.974±0.050	0.831±0.056
	0.10	0.913±0.024	0.856±0.082	1.021±0.088	0.854±0.053
	0.20	0.906±0.039	0.820±0.238	1.081±0.134	0.858±0.051
$[L_w(490)]_N/$ $[L_w(555)]_N$	0.05	0.980±0.005	0.966±0.010	1.013±0.021	0.968±0.013
	0.10	0.983±0.006	0.970±0.025	1.027±0.033	0.976±0.011
	0.20	0.983±0.011	0.968±0.066	1.043±0.045	0.976±0.011

Some statistics results for sediment-dominated Case-2 waters are presented in Table 4.4 for the M80 aerosols with the AOT at 865 nm of 0.05, 0.1, and 0.2. Results in Table 4.4 show that, for the sediment-dominated Case-2 water with the AOT of 0.1, errors in the derived $[L_w(443)]_N, [L_w(490)]_N$, and $[L_w(555)]_N$ from four algorithms vary from ~7-25%, ~5-15%, and ~4-10%, respectively, while the derived $[L_w(443)]_N/[L_w(555)]_N$ and $[L_w(490)]_N/[L_w(555)]_N$ change from ~2-15% and ~2-3%, respectively. Thus, errors in the radiance ratios are reduced significantly. For

the ratio of $[L_w(490)]_N / [L_w(555)]_N$, all four algorithms produced results within 5% for all three AOT values.

4.2.2 Yellow Substance-Dominated Waters

As one would expect, for the yellow substance-dominated waters, deriving the normalized water-leaving radiance accurately from satellite sensor measurements is extremely difficult, particularly for $[L_w(\lambda)]_N$ values at the short visible wavelengths. Not only are there non-negligible ocean contributions at the NIR bands (Figure 3.1b), but the ocean signals in the visible bands are also very small, compared with the $[L_w(\lambda)]_N$ spectra over open oceans (Case-1 waters) and sediment-dominated Case-2 waters. For example, the $[L_w(\lambda)]_N$ at 443 nm for typical open ocean, sediment-dominated, and yellow substance-dominated water are about 1.668, 2.053, and 0.061 mW cm$^{-2}\mu$m^{-1} sr^{-1} respectively (Tables 4.1 and 4.2), corresponding to the contributions of the sensor-measured TOA signal of about 9.8%, 11.8%, and 0.4%, respectively (Section 3.3).

Table 4.5 Statistics (mean and standard deviation) for Case-2 yellow-substance-dominated water for various AOT data.

Parameter	Case-2 Yellow-sub Water and for $\tau_a(865)$	Mean Ratio of Derived/True Value ± STD			
		SeaWiFS/MODIS	MERIS	OCTS/GLI	POLDER
$[L_w(443)]_N$	0.05	0.676±1.397	0.274±1.027	-0.763±0.620	-2.749±1.707
	0.10	0.482±1.695	2.979±2.601	0.501±1.581	-8.324±0.908
	0.20	0.774±1.721	5.407±5.656	2.142±3.251	-8.036±0.993
$[L_w(490)]_N$	0.05	1.097±0.500	0.480±0.281	0.298±0.178	-0.498±0.581
	0.10	1.071±0.670	1.448±0.820	0.714±0.533	-2.794±0.283
	0.20	1.228±0.567	2.264±1.923	1.243±1.071	-2.750±0.353
$[L_w(555)]_N$	0.05	1.159±0.189	0.703±0.109	0.681±0.027	0.413±0.150
	0.10	1.140±0.275	0.971±0.173	0.748±0.060	-0.412±0.073
	0.20	1.175±0.168	1.175±0.512	0.860±0.187	-0.418±0.106
$[L_w(443)]_N/$ $[L_w(555)]_N$	0.05	0.404±1.499	0.386±1.543	-1.146±0.919	-10.370±12.002
	0.10	0.046±1.889	2.759±2.163	0.524±1.927	20.462±1.669
	0.20	0.502±1.598	2.793±5.086	1.932±2.697	19.837±2.585
$[L_w(490)]_N/$ $[L_w(555)]_N$	0.05	0.896±0.398	0.665±0.388	0.432±0.249	-2.263±3.430
	0.10	0.832±0.514	1.401±0.592	0.913±0.586	6.877±0.599
	0.20	1.003±0.414	1.377±1.554	1.288±0.764	6.773±0.785

In this exercise, the $[L_w(\lambda)]_N$ at 490 nm for the yellow-substance type of water is 0.123 mW cm$^{-2}\mu$m^{-1} sr^{-1}, compared with values of 1.398 and 3.619 mW cm$^{-2}\mu$m^{-1} sr^{-1} for typical open ocean (Case-1) and sediment type waters. With this in mind,
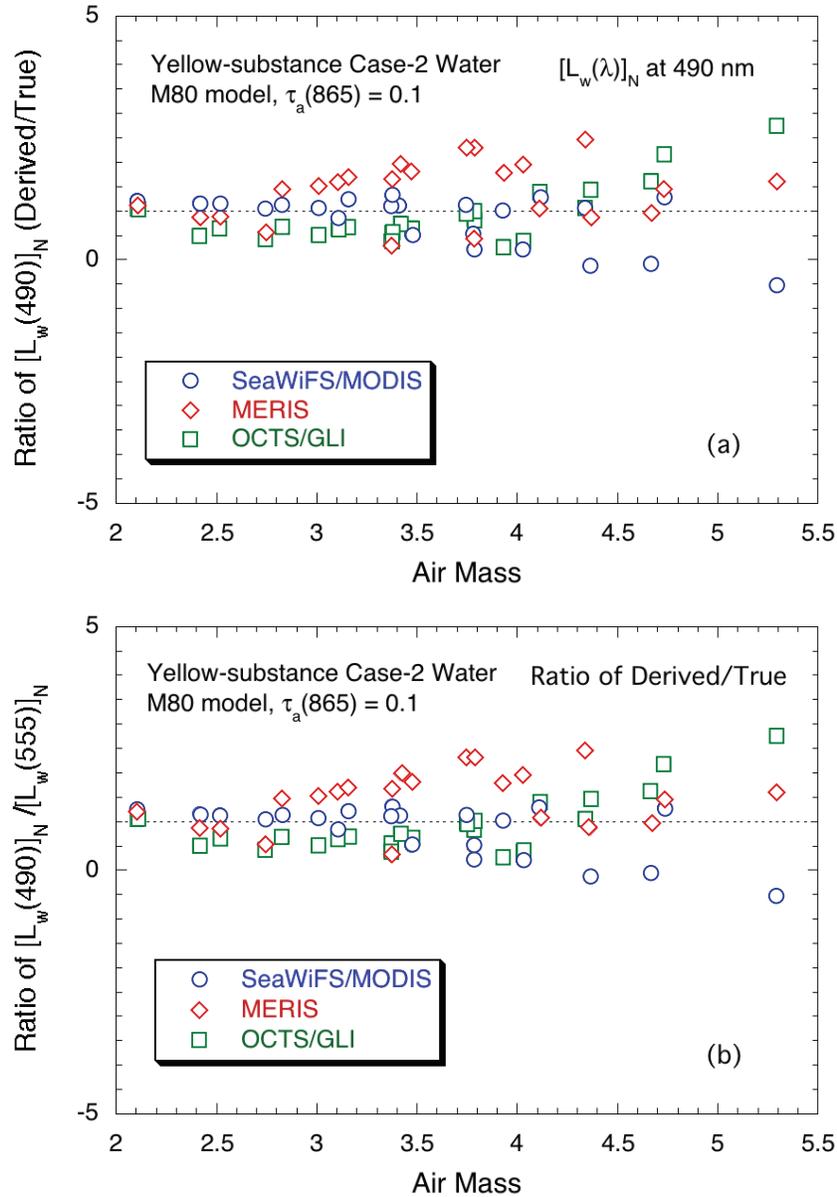
Figure 4.4 Ratio values (derived/true) of various ocean-colour parameters as a function of the air mass from atmospheric correction algorithms of SeaW-iFS/MODIS, MERIS, and OCTS/GLI, for (a) $[L_w(\lambda)]_N$ at 490 nm and (b) ratio $[L_w(490)]_N/[L_w(555)]_N$. These results are for the M80 aerosols with aerosol optical thickness of 0.1 at 865 nm and for a yellow substance-dominated Case-2 water. Note POLDER results are out of scale and are not shown in here.

we have only shown the comparison results for $[L_w(\lambda)]_N$ at 490 nm (Figure 4.4a) and the normalized water-leaving radiance ratio of $[L_w(490)]_N/[L_w(555)]_N$ (Figure 4.4b). The plot scales are also considerably enlarged (from -5 to 5) in Figure 4.4, compared with those in Figure 4.1 and Figure 4.3. Note that the POLDER results are not shown in Figure 4.4 because they are all outside the scale (see Table 4.5).

Statistics (mean and STD) comparison results for a yellow substance-dominated water and for various AOT values are summarized in Table 4.5. Results show significantly large errors in the derived $[L_w(443)]_N$, as well as for the parameter $[L_w(443)]_N/[L_w(555)]_N$, from all four algorithms. Conversely, errors for $[L_w(\lambda)]_N$ at wavelengths of 490 and 555 nm are reduced, compared with that for the blue bands. The sensor-derived $[L_w(490)]_N$, $[L_w(555)]_N$, and ratio results of $[L_w(490)]_N/[L_w(555)]_N$ may still be used with caution for retrieval of properties from yellow substance dominated waters. The relationships between the water-leaving radiance parameters and water properties for the Case-2, yellow substance-dominated waters are certainly different from the Case-1 waters.

4.3 Strongly-Absorbing Aerosols

4.3.1 Comparison Results

Figure 4.5 and Table 4.6 provide algorithm comparison results for the strongly-absorbing aerosols (U80 model) combined with a typical open ocean Case-1 water. The U80 aerosol particles are very strongly absorbing with the single-scattering albedo values of 0.783, 0.782, 0.781, 0.774, 0.762, and 0.748 for wavelengths of 443, 490, 555, 765, and 865 nm, respectively. Figure 4.5a shows comparison results for the ratio (derived/true) of sensor-derived $[L_w(\lambda)]_N$ at the wavelength of 443 nm, while Figure 4.5b shows the comparison results for the ratio of $[L_w(443)]_N/[L_w(555)]_N$. The pseudo-TOA radiance data were simulated with a two-layer atmosphere (aerosols in the bottom) for the U80 model with the AOT of 0.1 at 865 nm, overlying a clear, open ocean, Case-1 water (chlorophyll = 0.1 mg/m^3). Obviously, for this strongly-absorbing aerosol case, all four algorithms fail badly at deriving accurate $[L_w(\lambda)]_N$, i.e., the derived $[L_w(\lambda)]_N$ in the visible is significantly biased low (Figure 4.5a) with mean errors from the four algorithms of about $35 - 60\%$ (Table 4.6). However, the radiance ratio values are not that bad, particularly for the parameter $[L_w(443)]_N/[L_w(555)]_N$. Indeed, results in Table 4.6 show that mean errors in the derived $[L_w(443)]_N/[L_w(555)]_N$ are all within $\sim$10%. Thus, the radiance ratio values of $[L_w(443)]_N/[L_w(555)]_N$ may still be used

for deriving reasonable chlorophyll concentration values even though the $[L_w(\lambda)]_N$ values are not very accurate.

Table 4.6 Statistics (mean and standard deviation) for strongly absorbing aerosols (U80) with Case-1 water.

Parameter	C=0.1 mg/m^3 and for $\tau_a(865)$	Mean Ratio of Derived/True Value ± STD			
		SeaWiFS/MODIS	MERIS	OCTS/GLI	POLDER
$[L_w(443)]_N$	0.10	0.438±0.201	0.556±0.104	0.535±0.140	0.432± 0.232
$[L_w(490)]_N$	0.10	0.561±0.161	0.654±0.082	0.627±0.111	0.563±0.181
$[L_w(555)]_N$	0.10	0.383±0.276	0.602±0.170	0.567±0.195	0.469±0.257
$[L_w(443)]_N/$ $[L_w(555)]_N$	0.10	1.077±0.597	0.975±0.210	0.995±0.200	0.885±0.188
$[L_w(490)]_N/$ $[L_w(555)]_N$	0.10	1.416±1.134	1.154±0.254	1.214±0.376	1.327±0.770

The effects of the strongly-absorbing aerosols over Case-2 waters can be understood and explained by plotting the TOA reflectance ratio $[\rho_t - \rho_r](\lambda, 865) = [\rho_t(\lambda) - \rho_r(\lambda)]/[\rho_t(865) - \rho_r(865)]$ as a function of the wavelength for various cases. Figure 4.6a compares $[\rho_t - \rho_r](\lambda, 865)$ values for M80 (weakly-absorbing) and U80 (strongly-absorbing) aerosols with three different ocean waters, i.e., a typical clear Case-1 water mass, sediment-dominated Case-2 water, and yellow substance dominated Case-2 water. For a typical clear Case-1 water mass, the derived $[L_w(\lambda)]_N$ in the visible bands would be significantly underestimated (Figure 4.5a) with a non- or weakly-absorbing aerosol (e.g., M80 in Figure 4.6a) for estimation of the aerosol radiance contributions, i.e., as shown in Figure 4.6a the $[\rho_t - \rho_r](\lambda, 865)$ values at the visible are larger for the M80 model than the U80 model, leading to overestimation of aerosol radiance contribution and underestimation of the ocean radiance contributions. Similar cases are also shown for the two Case-2 waters in Figure 4.6a. However, underestimations of $[L_w(\lambda)]_N$ values are even worse due to ocean contributions at the NIR bands (combined problems for turbid waters in Figure 4.3 and Figure 4.4 and strongly-absorbing aerosols in Figure 4.5). Furthermore, another difficulty in dealing with this issue of strongly-absorbing aerosols, is that the aerosol radiance contributions depend on the aerosol vertical distribution, which is discussed further in the following section.

4.3.2   Effects of Vertical Distribution of Absorbing Aerosol

The effect of the vertical distribution of absorbing aerosols on the satellite-derived $[L_w(\lambda)]_N$ values can be demonstrated through the results in Figure 4.6b, which shows results of the TOA reflectance ratio as a function of the wavelength, for a strongly-absorbing aerosol (U80) with aerosol vertical distributions of two-layer
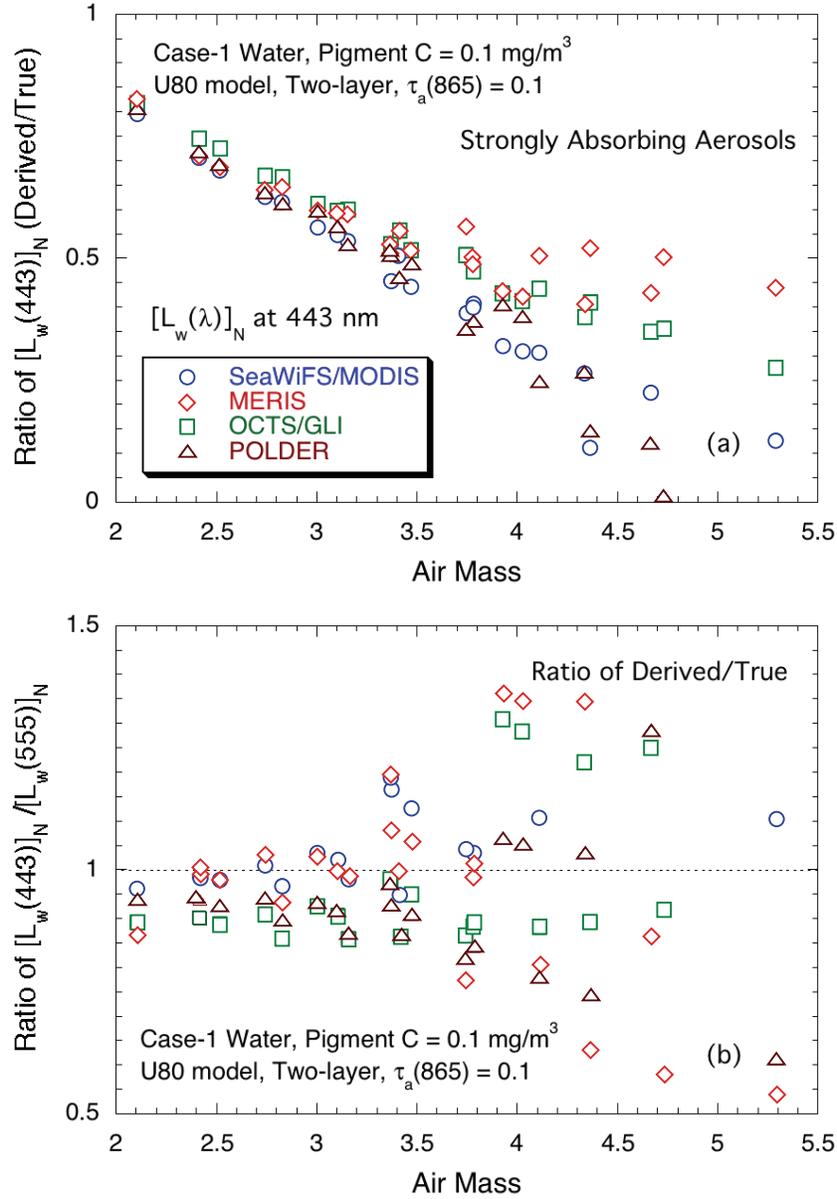
Figure 4.5 Ratio values (derived/true) of various ocean-colour parameters as a function of the air mass from atmospheric correction algorithms of SeaW-iFS/MODIS, MERIS, OCTS/GLI, and POLDER for (a) $[L_w(\lambda)]_N$ at 443 and (b) ratio $[L_w(443)]_N/[L_w(555)]_N$. These results are for the U80 (strongly-absorbing) aerosols with aerosol optical thickness of 0.1 at 865 nm and for open ocean (Case-1) water with a chlorophyll concentration of 0.1 mg/m^3.
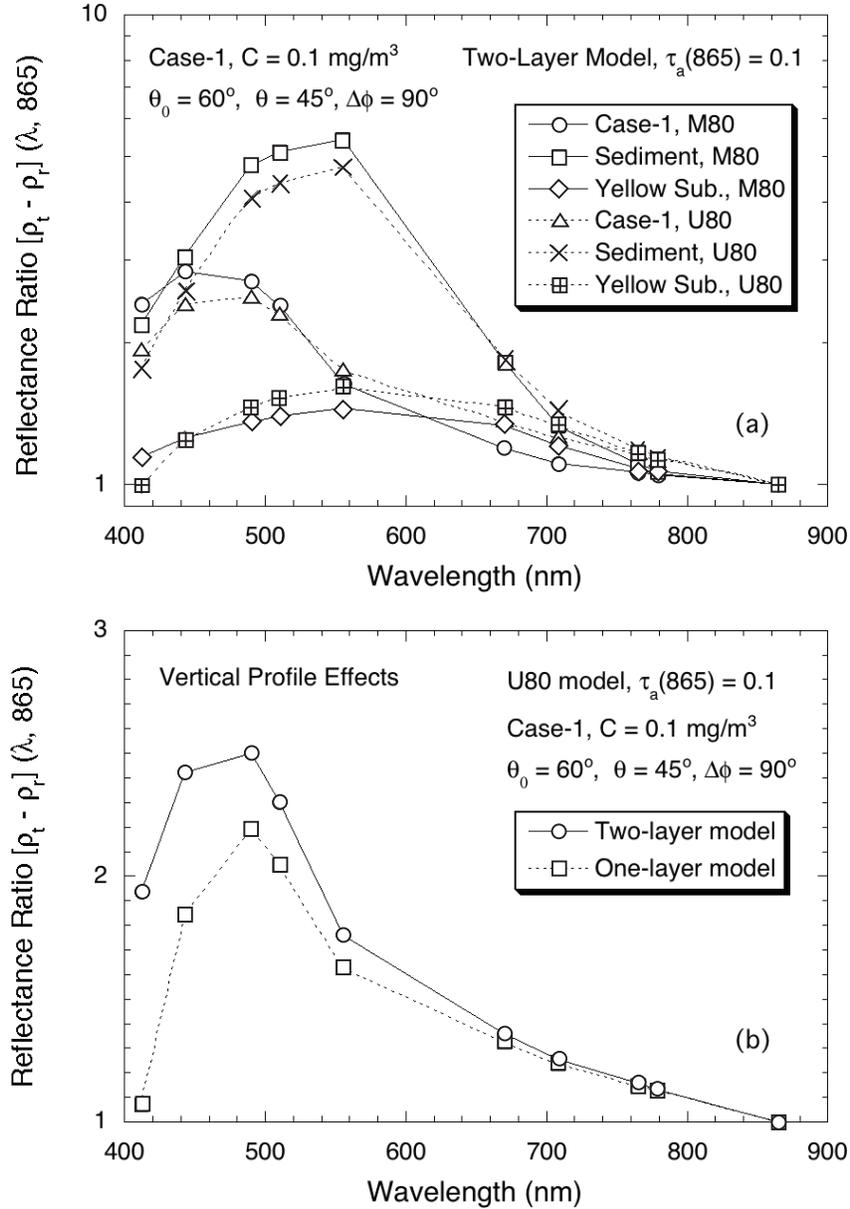
Figure 4.6 Reflectance ratio of $[\rho_t(\lambda) - \rho_r(\lambda)]/[\rho_t(865) - \rho_r(865)]$ as a function of the wavelength for various cases, demonstrating the effects of strongly-absorbing aerosols. (a) Comparison results of M80 (weakly absorbing) and U80 (strongly-absorbing) aerosols for Case-1 and Case-2 waters and, (b) aerosol vertical effects for strongly-absorbing aerosols (U80) compared with aerosol vertical distributed as two-layer and one-layer atmospheric models.

and one-layer atmospheric models. The two-layer model has been used for all computations in this report and the one-layer model is for aerosols (U80) uniformly mixed with molecules (Rayleigh). This is for a typical Case-1 water and for an AOT at 865 nm (U80) of 0.1. Thus, the only difference in computing two cases of $[\rho_t - \rho_r](\lambda, 865)$ in Figure 4.6b is their different vertical distributions. At the NIR wavelengths, the two cases give exactly the same $[\rho_t - \rho_r](\lambda, 865)$, while at the visible wavelengths (particularly at the blue bands) $[\rho_t - \rho_r](\lambda, 865)$ values are considerably different (with the one-layer model having significantly lower values) (Figure 4.6b). These results indicate that, for strongly-absorbing aerosols, the TOA aerosol radiance is strongly dependant upon the aerosol vertical distribution, and this information cannot be obtained from the NIR measurements. Therefore, to derive ocean-colour products accurately over strongly absorbing aerosols such as dust and smoke, information about aerosol vertical distribution is required. Such information can be obtained from LIDAR measurements, or possibly from passive measurements in the oxygen A-band (Dubuisson *et al.*, 2009).

4.4 Brief Summary

Algorithm performance evaluations from the comparison results presented in Sections 4.1 to 4.3 of this report are summarized briefly below.

4.4.1 Case-1 Waters

For the open ocean, Case-1 waters, all four operational algorithms performed reasonably well. For a typical open ocean and atmosphere case, the algorithms for MERIS, OCTS/GLI, SeaWiFS/MODIS, and POLDER produced mean errors of $[L_w(\lambda)]_N$ in the visible to within 2%, 4%, 5%, and 9% respectively, while for the radiance ratio values $([L_w(443)]_N/[L_w(555)]_N)$ and $[L_w(490)]_N/[L_w(555)]_N)$, mean errors for MERIS, SeaWiFS/MODIS, POLDER, and OCTS/GLI were within 2%, 2%, 6%, and 6% respectively. On the other hand, the SeaWiFS/MODIS algorithm consistently produced results with the lowest noise (STD) errors among the four operational algorithms.

Both POLDER and OCTS/GLI produced excellent aerosol optical thickness products, while SeaWiFS/MODIS and MERIS overestimated the AOT data. For a typical case, the mean errors in the derived AOT for POLDER, OCTS/GLI, SeaWiFS/MODIS, and MERIS are about 3%, 4%, 8%, and 14% respectively. With the use of vector aerosol lookup tables, the mean error in the derived AOT for SeaWiFS/MODIS algorithm can be reduced to 4%, in addition to a considerably reduced noise (STD) error.

4.4.2 Case-2 Waters

For the coastal region Case-2 waters, all four operational algorithms produced some significant errors in deriving ocean-colour products, particularly for the yellow

substance-dominated waters. For a sediment-dominated Case-2 water and a typical maritime atmosphere, mean errors in $[L_w(\lambda)]_N$ for wavelengths 443, 490, and 555 nm for SeaWiFS/MODIS, OCTS/GLI, POLDER, and MERIS ranged from 4–12%, 7–10%, 10–23% and 13–25%, respectively, while the mean errors in $[L_w(443)]_N/[L_w(555)]_N$ and $[L_w(490)]_N/[L_w(555)]_N$ for OCTS/GLI, SeaWiFS/MODIS, POLDER, and MERIS are 2–3%, 2–9%, 2–15%, and 3–14% respectively. It should be noted that all four operational algorithms can produce $[L_w(490)]_N/[L_w(555)]_N$ accurately with mean errors of ~2%. Again, the SeaWiFS/MODIS algorithm produced the lowest noise errors in the derived ocean-colour products.

However, for yellow substance dominated Case-2 waters, all four algorithms performed poorly, particularly $[L_w(\lambda)]_N$ in the short blue bands. On the other hand, satellite-derived $[L_w(\lambda)]_N$ at 490 and 555 nm, as well as radiance ratio of $[L_w(490)]_N/[L_w(555)]_N$ may still be useful for retrieval of some water property products from the CDOM-type waters (e.g, some results from SeaWiFS/MODIS).

4.4.3 Cases with Strongly-Absorbing Aerosols

For the strongly-absorbing aerosol (U80) case, all four operational algorithms significantly underestimated the derived $[L_w(\lambda)]_N$ values in the visible. Indeed, for a typical open ocean case (the most favorable ocean condition for algorithm performance) and with AOT of 0.1 at 865 nm, all four operational algorithms essentially failed to produce reasonable $[L_w(\lambda)]_N$ values, with mean errors in $[L_w(\lambda)]_N$ ranging from around -35% to -60%. However, algorithms can still produce good or reasonable radiance ratio values, particularly for the parameter $[L_w(490)]_N/[L_w(555)]_N$, therefore chlorophyll concentrations. In fact, the mean errors in the derived $[L_w(490)]_N/[L_w(555)]_N$ for OCTS/GLI, MERIS, SeaWiFS/MODIS, and POLDER are 0.5%, 2.5%, 7.7% and 12.5%, respectively, which are accurate enough for producing reasonable chlorophyll products, at least for low or moderate chlorophyll, where the ratio rapidly evolves as a function of chlorophyll.

Algorithm Validations from *In Situ* Data

Menghua Wang, Hajime Fukushima, Robert Frouin, David Antoine, Howard R. Gordon and André Morel

The atmospheric correction algorithms discussed in this report have been implemented into the corresponding data processing systems for producing the global ocean-colour products from various satellite ocean-colour sensors. Supported by the corresponding agencies and countries, there has been a significant effort in acquiring ocean-colour *in situ* data (see Mueller and Fargion, 2002; Werdell *et al.*, 2003; Werdell and Bailey, 2005), for validating the ocean-colour products produced by the satellite ocean-colour sensors SeaWiFS, MODIS, MERIS, OCTS/GLI, and POLDER (see Shimada *et al.*, 1998; Bailey *et al.*, 2000; Wang *et al.*, 2005; Bailey and Werdell, 2006; Murakami *et al.*, 2006; Zibordi, *et al.*, 2006; Antoine *et al.*, 2008). For the current operational SeaWiFS, MODIS, and MERIS global ocean-colour missions, there has been a continuous effort for algorithm evaluation and refinement through *in situ* data validation and global satellite ocean-colour data analyses (e.g. Wang, 2000; Patt, *et al.*, 2003; McClain *et al.*, 2004; Antoine *et al.*, 2008). In fact, SeaWiFS has undergone five major reprocessings of the entire data set. Each reprocessing has addressed the data quality issues that are related to the sensor calibration, instrument navigation, data masks and flags, and retrieval algorithms. In addition, from 1997—2003, the NASA Sensor Inter-calibration and Merger for Biological and Interdisciplinary Oceanic Studies (SIMBIOS) Project (McClain *et al.*, 2002) has played a leading role in the international ocean community to define and document a series of *in situ* data acquisition strategies and methodologies to ensure consistency in the *in situ* data collection for satellite algorithm evaluation and validation. The next section briefly describes a number of validation studies for SeaWiFS, MODIS, MERIS, OCTS/GLI, and POLDER data products.

5.1 The NOMAD Data Set for Algorithm Evaluation for Global Oceans

Using the NASA bio-Optical Marine Algorithm Data set (NOMAD), Werdell and Bailey (2005) and Bailey and Werdell (2006) evaluated the SeaWiFS-derived ocean-colour

products for both global oceans and ocean regions with deep water (usually open oceans). Their results show that over open oceans the mean ratio values (SeaWiFS vs. *in situ*) of SeaWiFS-derived $[L_w(\lambda)]_N$ at wavelengths of 412, 443, 490, 510, and 555 nm are 1.030, 0.962, 0.956, 0.975, and 0.976, respectively. However, for the global oceans (including coastal regions), these ratio values are reduced to 0.905, 0.915, 0.918, 0.918, and 0.915, respectively. These results are consistent with the simulation results of the SeaWiFS/MODIS algorithm performance discussed in previous sections in this report, showing better algorithm performance over the open ocean (Case-1 waters). It should be noted that the SeaWiFS/MODIS algorithm is not designed for Case-2 coastal waters, resulting in large uncertainties for satellite match-ups (particularly for $[L_w(\lambda)]_N$ in the blue), as has been reported by Feng *et al.* (2008) for coastal waters along the northeast coast of the U.S. and Mélin *et al.* (2007) for a coastal site in the northern Adriatic Sea.

5.2   The BOUSSOLE *In Situ* Data Set for Algorithm Evaluation

Using the *in situ* data from a deep, clear ocean site in the northwestern Mediterranean Sea (BOUSSOLE site) from September 2003 to October 2006, Antoine *et al.* (2008) evaluated algorithm performances for deriving ocean-colour products from SeaWiFS, MODIS-Aqua, and MERIS. Some AOT results were also included in the study. Their evaluation results show that the mean ratio values (satellite vs. *in situ*) for the SeaWiFS-derived normalized water-leaving reflectance $[\rho_w(\lambda)]_N$ at wavelengths 412, 443, 490, 510, 555 nm are 0.92, 1.00, 0.97, 0.95, and 0.90 respectively, while mean ratios for the MODIS-Aqua $[\rho_w(\lambda)]_N$ at wavelengths 412, 443, 488, 551 nm are 0.90, 0.99, 0.95, and 0.88, respectively. The MERIS-derived $[\rho_w(\lambda)]_N$ results show some significant over-estimations in the blue bands, with ratio values of 1.60, 1.32, 1.16, 1.22, and 1.21 for $[\rho_w(\lambda)]_N$ at wavelengths of 412, 443, 490, 510, and 560 nm respectively. Similar overestimation results have also been reported for MERIS data in a comparison study by Zibordi *et al.* (2006) for a coastal site in the northern Adriatic Sea. The overestimation of the MERIS-derived $[\rho_w(\lambda)]_N$ products, however, is most likely due to the lack of on-orbit vicarious calibration, which is necessary, and has been employed by both SeaWiFS and MODIS. The introduction of such a vicarious calibration is currently underway for MERIS. In addition, this study also showed that both SeaWiFS and MODIS-Aqua derived $[\rho_w(\lambda)]_N$ products show similar noise errors, which are lower (particularly in the blue bands) than those from MERIS.

On the other hand, the AOT comparison results (Antoine, *et al.*, 2008) show that SeaWiFS-derived AOT data are overestimated, compared with the ground-based measurements. The AOT over-estimations are consistent with results of Wang *et al.* (2005), and as was discussed earlier in this report, the derived AOT data can be improved with the use of the vector aerosol lookup tables that include the polarization effects (Wang, 2006a).

5.3   Some Validation Results for OCTS/GLI

For OCTS, *in situ* water-leaving radiance data were collected through international and interagency collaboration (Shimada *et al.*, 1998) at about 500 stations, but under rather stringent match-up conditions only 11 remained and were used for validation studies. The standard deviation of the $[L_w(\lambda)]_N$ estimate against *in situ* data was about +100% for the 412–520 nm bands, and about +400% for the 550 nm band with significantly large bias, which was understood to be related to calibration offset of the OCTS instrument, and not necessarily from the atmospheric correction algorithm. For GLI validation, Murakami *et al.* (2006) examined 435 $[L_w(\lambda)]_N$ data, again obtained through international and domestic collaboration, including nearly 300 data measurements collected by SIMBAD/SIMBADA hand-held radiometers (Deschamps *et al.*, 2004). The results (Murakami, *et al.*, 2006) show that the median absolute percentage differences (MedPD) between GLI and *in situ* data were 14.1–35.7% for $[L_w(\lambda)]_N$ at 380–565 nm using the 'Version 2.1' GLI atmospheric correction algorithm (Toratani *et al.*, 2007) where an empirical absorptive aerosol correction was implemented. However, Fukushima *et al.* (2007) compared the performance of algorithm Version 2.1 vs. Version 1.5, and the performance of the two was rather similar, suggesting that aerosol absorption is not a factor in the observed $[L_w(\lambda)]_N$ error.

5.4   The SIMBAD(A) *In situ* Data Set for POLDER Algorithm Evaluation

Using SIMBAD, and the advanced SIMBADA field radiometers (Deschamps *et al.*, 2004), above-water marine reflectances were measured in various oceans during cruises of opportunity, and compared with POLDER-1 and -2 estimates. In Case-1 waters, the comparison statistics were as follows: for POLDER-1, the bias between estimated and measured values was 0.001 at 443 nm (167 match-ups), 0.0019 at 490 nm (97 match-ups), and 0.0005 at 560 nm (167 match-ups). The corresponding standard deviations were 0.0051, 0.0035, and 0.0018, respectively (Fougnie, 1998). For POLDER-2 the values, obtained with 101 match-ups were -0.0021, -0.0028, and -0.0025 respectively for the bias, and 0.0048, 0.0041, and 0.0038 for the standard deviation (see `http://smsc.cnes.fr/POLDER/SCIEPROD/oc_pr.htm`). The POLDER-2 performance falls short of the accuracy requirement of 0.001–0.002 in the blue in oligotrophic waters (Gordon, 1997). The POLDER-3 estimates were evaluated using underwater radiometric measurements at the BOUSSOLE site during 2005 and 2006 (186 match-ups), which resulted in a standard deviation of 0.0019 at 490 nm and 0.0009 at 565 nm (Steinmetz, 2008). This was obtained after correction of the POLDER-3 radiance for residual stray light in the optical system. Note that the POLDER-3 spectral band centered on 443 nm, which has a high dynamic range, is

not used for ocean-colour purposes, but for cloud detection.

Conclusions and Recommendations

Menghua Wang, Howard R. Gordon, David Antoine, Robert Frouin André Morel, Hajime Fukushima and Pierre-Yves Deschamps

Several conclusions are evident from this algorithm comparison exercise, the most important of which is the good performance of the algorithms in Case-1 waters (comprising the bulk of the global oceans), with assumption of realistic maritime aerosol models. Although several conclusions below address improvements recommended for atmospheric correction, these are required only for a small portion of the global oceans, i.e., mainly areas near the coast with high concentrations of dissolved organic matter and/or suspended sediments, or areas influenced by wind-blown dust or urban pollution. In general, the atmospheric correction algorithms for global ocean-colour data processing can be considered highly successful. Listed below are the specific conclusions reached from this algorithm comparison exercise.

❖ For open ocean Case-1 waters with maritime aerosols, all four operational atmospheric correction algorithms generally performed well in deriving the $[L_w(\lambda)]_N$ spectra and radiance ratio values. Thus, over open oceans, ocean-colour radiance products can be derived accurately in most cases from satellite remote sensors. However, some *in situ* validation results show that further improvements in the data product are still required and are possible, particularly for $[L_w(\lambda)]_N$ in the blue.

❖ For a sediment-dominated Case-2 water with typical maritime aerosols, all four operational algorithms produced slightly larger errors in the $[L_w(\lambda)]_N$ in the blue bands, mainly due to an incorrect estimation of the NIR ocean contributions. The $[L_w(\lambda)]_N$ in the longer visible wavelengths (e.g. 555 nm), and radiance band ratio values can be retrieved accurately. Since the $[L_w(\lambda)]_N$ spectra for the sediment-dominated waters are highest in the green-red wavelengths, it is suggested that the satellite-derived $[L_w(\lambda)]_N$ and radiance ratio at the longer visible bands are used for retrieval of sediment-dominated water optical and biological properties.

❖ For a yellow substance-dominated Case-2 water, all four operational algorithms performed poorly, particularly for the $[L_w(\lambda)]_N$ in the blue band. It

is extremely difficult (if not impossible) to derive accurate $[L_w(\lambda)]_N$ in the blue because radiance signals in that region of the spectrum are very low for CDOM-type waters (strong absorption). In addition, the derived $[L_w(\lambda)]_N$ in the blue contains very significant noise errors. However, the $[L_w(\lambda)]_N$ in the blue should be used to obtain CDOM absorption information (i.e., to distinguish it from phytoplankton absorption), even though the blue radiance is difficult to derive accurately. The spectral shape of $[L_w(\lambda)]_N$, i.e., ratios, could be helpful for deriving the water property for yellow substance dominated waters.

❖ All four operational algorithms failed to produce accurate $[L_w(\lambda)]_N$ spectra in the visible wavelengths for a strongly-absorbing aerosol (U80). Satellite-derived $[L_w(\lambda)]_N$ values are significantly underestimated, with the mean error in $[L_w(\lambda)]_N$ ranging from around -35% to -60%. However, the radiance ratio, in particular $[L_w(490)]_N/[L_w(555)]_N$, is still reasonably accurate for the retrieval of ocean chlorophyll concentrations. For accurate retrieval of the $[L_w(\lambda)]_N$ spectra data over a strongly absorbing aerosol, one must (i) identify the presence of the strongly-absorbing aerosols and (ii) acquire the aerosol vertical distribution, for example from LIDAR measurements.

❖ Errors in the derived $[L_w(\lambda)]_N$ spectra from the various atmospheric correction algorithms are spectrally correlated, as was demonstrated in this report. Consequently, the resulting errors in radiance band ratios (e.g. $[L_w(490)]_N/[L_w(555)]_N$) are reduced. It is recommended that radiance band ratios should be used preferentially for deriving ocean optical and biological properties.

❖ The aerosol product (that is, aerosol optical thickness) is a by-product of ocean-colour data processing (atmospheric correction). Results show that the AOT data over the oceans can be derived accurately using the vector aerosol lookup tables, with errors within $\sim 5\%$. It was also demonstrated that the ocean $[L_w(\lambda)]_N$ spectra can be derived accurately using the scalar aerosol lookup tables, even though there are some slightly larger over estimations in the derived AOT data.

❖ Future development of ocean-colour remote sensing will require considerable efforts in retrieving ocean-colour products in the coastal ocean regions, where waters are not only Case-2 types, but the aerosols are often strongly absorbing (depending on the region). Some regional algorithms and approaches are useful in dealing with coastal complex ocean waters, for example the spectral matching algorithm, the spectral optimization algorithm, and neural network approaches. Furthermore, in order to deal with significant ocean contributions in the NIR bands in turbid waters, future satellite sensors will require SWIR bands with high signal-to-noise characteristics for measurement of optical

and biological properties in coastal and inland turbid waters. In dealing with the strongly-absorbing aerosols, it is first necessary to detect the presence of the strongly-absorbing aerosols (e.g. using measurements in the UV bands where the TOA signal is very sensitive to the aerosol absorption), and then to derive the aerosol vertical profile (for example, from LIDAR measurements) with sufficient accuracy for atmospheric correction.

Details of the POLDER Algorithm

Robert Frouin, Pierre-Yves Deschamps and Jean-Marc Nicolas

A.1 Radiometric Model

After radiometric calibration, POLDER Level-1 data are in the form of TOA normalized radiance, defined for each band j and direction i as:

$$R_{mea}(\lambda_j, i) = \pi L_{mea}(\lambda_j, i)/F_0(\lambda_j) \tag{A.1}$$

where L_{mea} is the measured radiance. The TOA normalized radiance, after corrections for gaseous absorption and scattering/absorption by stratospheric aerosols (made just after cloud masking), is expressed as:

$$R_t(\lambda_j, i) = R_{mol}(\lambda_j, i) + R_{gm}(\lambda_j, i) + R_{aer}(\lambda_j, i) + R_{ga}(\lambda_j, i) + T_o(\lambda_j, i)T(\lambda_j, i)R_g$$
$$+ \frac{t_o(\lambda_j, i)t(\lambda_j, i)\cos\theta_0\{[\rho_w(\lambda_j, i)]_N + [\rho_{wc}(\lambda_j)]_N\}}{1 - S(\lambda_j)\{[\rho_w(\lambda_j, i)]_N + [\rho_{wc}(\lambda_j)]_N\}}, \tag{A.2}$$

where R_{mol} accounts for multiple scattering by molecules, R_{gm} accounts for coupling terms between molecules and photons reflected on a rough sea surface, R_{aer} accounts for multiple scattering by aerosols and by molecules plus aerosols, R_{ga} accounts for coupling terms between aerosols and photons reflected on a rough surface, and S is the spherical albedo of the atmosphere (accounts for successive photon interactions with surface, then atmosphere, and again surface). In order to include multiple scattering on both molecules and aerosols (coupling), R_{aer} is computed as $R_{aer} = R_{tot} - R_{mol}$, where R_{tot} is the total (aerosol + molecule) scattering term. This decomposition allows one to adjust the molecular term by sea-surface pressure without modifying the aerosol term. It should be noted that Equation A.2 is only exact when the surface reflectance above the air-sea interface (water body + whitecaps) is isotropic.

A.2 Aerosol Model Inversion

The first step of the process is first the evaluation of the spectral dependence of the observed aerosol signal in the red and NIR part of the spectrum, and then of the

model which can be associated with that spectral dependence, including multiple scattering effects. First a corrected normalized radiance, R_{cor}, is computed from the normalized radiance R_t in each band j ($j = 4, 5, 6$ with $\lambda_4 = 670$ nm, $\lambda_5 = 765$ nm, $\lambda_6 = 865$ nm) and each viewing direction i:

$$R_{cor}(\lambda_j, i) = R_t(\lambda_j, i) - R_{mol}(\lambda_j, i) - R_{gm}(\lambda_j, i) - T_o(\lambda_j, i)T(\lambda_j, i)R_g$$

$$= R_{aer}(\lambda_j, i) + R_{ga}(\lambda_j, i) + \frac{t_o(\lambda_j, i)t(\lambda_j, i)\cos\theta_0[\rho_{wc}(\lambda_j)]_N}{1 - S(\lambda_j)[\rho_{wc}(\lambda_j)]_N} \qquad \text{(A.3)}$$

Then a weighted spectral dependence measured over all viewing directions is computed:

$$\epsilon = \sum_i \frac{AR_{cor}(670, i) + (1 - A)R_{cor}(765, i)}{R_{cor}(865, i)}, \qquad \text{(A.4)}$$

where A is a variable weighting factor taking values in the range 0–1. For POLDER-1, A is set to 1 because the noise affecting the 765 nm band is too high and would strongly affect the retrieved marine reflectance. In parallel, the same computation is carried out for each aerosol model in the lookup table database:

$$\epsilon_{\text{mod}} = \sum_i \frac{AR_{\text{mod}}(670, i) + (1 - A)R_{\text{mod}}(765, i)}{R_{\text{mod}}(865, i)} \qquad \text{(A.5)}$$

where $R_{\text{mod}}(\lambda_j, i)$ is linearly interpolated on four variables $(\theta_0, \theta, \phi, \tau_a)$.

Comparison of ϵ and ϵ_{mod} yields two models x and y such that $\epsilon_x < \epsilon < \epsilon_y$. The distance d_x is also computed:

$$d_x = \frac{\epsilon - \epsilon_x}{\epsilon_y - \epsilon_x} \qquad \text{(A.6)}$$

The 12 aerosol models have been organized in growing ϵ_{mod} order and selected so that their ϵ_{mod} values never cross each other for the geometries generally observed. The model that best fits the observation is coded as a real number, denoted Xd_x, between 1 and 12.

A specific procedure has been developed for very clear observations. In such situations, the spectral dependence is highly unpredictable because the denominator in Equation A.4 is very small. The aerosol model is set to a fixed value (C90) for very low aerosol loadings to prevent adding noise in the final estimates (marine reflectance and chlorophyll concentration). A threshold is applied to R_{cor} for each direction, and when a direction is below the threshold, the spectral dependence is forced to the value of the fixed model. For POLDER-1, the threshold accounts for an aerosol optical thickness of about 0.05.

A.3 Dealing with the 'Black-Pixel Assumption'

Aerosol model inversion relies on the hypothesis of a black ocean from 670 nm to 865 nm. It has been demonstrated that this is not true for eutrophic and Case-2

waters, where absorption of pure water is counter-balanced by scattering of particles (organic or inorganic). Thus the contribution of marine reflectance generally leads to overestimation of the aerosol Ångström coefficient. The computation of the marine reflectance is necessary prior to aerosol inversion, which in turn is necessary to compute marine reflectance correctly. Solutions currently developed rely on an iterative process (Siegel *et al.*, 2000) or on spatial homogeneity of aerosols versus water heterogeneity (Ruddick *et al.*, 2000).

In the operational algorithm, where computation time should be minimized, a simple solution has been developed, based on an empirical relationship between marine reflectance at 565 and 670 nm. This solution, first developed for CZCS by Viollier *et al.* (1980), has been shown to work reasonably well for waters that can be observed at POLDER spatial resolution, including high sedimentation and coccolithophorid bloom situations. Problems arise potentially over waters highly charged with yellow substances, where the algorithm will not work correctly.

The hypothesis that a linear relationship exists between marine reflectance at 565 and 670:

$$[\rho_w(670)]_N = a[\rho_w(565)]_N + b, \tag{A.7}$$

where $a \sim 0.20$ and $b \sim -0.0005$. Using that relationship, a new weighted spectral dependence is computed:

$$\epsilon = \sum_i \frac{A[R_{cor}(670, i) - aR_{cor}(565, i) + b] + (1 - A)R_{cor}(765, i)}{R_{cor}(865, i)}, \tag{A.8}$$

where the marine contributions at 565 and 670 nm cancel each other out.

A.4   Aerosol Optical Thickness Inversion

The second step of the process is the inversion of the aerosol optical thickness from observations. The corrected radiance $R_{cor}(865)$ is used in all viewing directions. For each direction and each tabulated optical thickness, $R_{mod}(865, i, \tau_a)$ is interpolated for four variables $(\theta_0, \theta, \phi, Xd_x)$ in the pre-computed lookup table. The arithmetic mean over all viewing directions is computed for R_{mod} and R_{cor} and the aerosol optical thickness τ_a is then given by:

$$\tau_a = \sum \frac{[\langle R_{mod}(865, \tau_{a2}) \rangle) - \langle R_{cor}(865) \rangle]\tau_{a1} + [\langle R_{cor}(865) \rangle - \langle R_{mod}(865, \tau_{a1}) \rangle]\tau_{a2}}{\langle R_{mod}(865, \tau_{a2}) \rangle - \langle R_{mod}(865, \tau_{a1}) \rangle}, \tag{A.9}$$

where $\langle R_{mod}(865), \tau_{a1} \rangle$ and $\langle R_{mod}(865), \tau_{a2} \rangle$ are the simulated radiances for aerosol model Xd_x (determined in the first step; see above) and for the tabulated aerosol optical thicknesses τ_{a1} and τ_{a2} that give simulated radiances surrounding the corrected radiance $\langle R_{cor}(865) \rangle$.

A.5 Dealing with Absorbing Aerosols

Absorption by aerosols is a difficult problem to solve because its main impact is observed in the very bands used for ocean-colour applications, i.e. in short wavelengths, because molecular scattering is maximum at these wavelengths, and because the absorption effect is proportional to the level of the signal. Near infrared information, therefore, cannot be readily extrapolated to the visible part of the spectrum. One solution using the multi-directionality capability of the POLDER instrument has been developed to deal with such absorbing aerosols. It relies on the change of absorption efficacy with molecular scattering and air mass changes. The aerosol absorption effect varies almost linearly with molecular scattering radiance multiplied by air mass, irrespective of aerosol altitude. The slope of the linear relation is related to the efficacy of aerosol absorption.

These characteristics have been implemented in the operational algorithm using the aerosol family concept. An aerosol family is a set of models (12) with consistent absorption. The core of the algorithm is played for each family, and the slope defined above is computed for each family. The family that leads to the slope nearest to zero is selected for final atmospheric correction.

A.6 Atmospheric Correction of Ocean-Colour Bands (443, 490, and 565 nm)

After having gone through the two steps described above twice for each family (i.e., one iteration), the aerosol model, optical thickness, and family inverted from that process are used to compute surface marine reflectance from the corrected TOA normalized radiances.

First, for each viewing direction a NIR equivalent corrected radiance, R_e, is computed as a weighted mean over the three red and NIR bands:

$$R_e(i) = \frac{a_{670}R_{cor}(670, i) + a_{765}R_{cor}(765, i) + a_{865}R_{cor}(865, i)}{a_{670} + a_{765} + a_{865}} \tag{A.10}$$

where a_{670}, a_{765}, and a_{865} are the weights given to each band. For POLDER-1, owing to the noise considerations mentioned above, a_{765} is equal to zero and a_{670} and a_{865} are equal to 0.5. Then for each ocean-colour band j ($j = 1, 2, 3$ with $\lambda_1 = 443$nm, $\lambda_2 = 490$nm, $\lambda_3 = 565$nm) the spectral dependence of the aerosol radiance, ϵ_e, is interpolated on five variables $(\theta_0, \theta, \phi, Xd_x, \tau_a)$ in the lookup table:

$$\epsilon_e(\lambda_j, i) = R_{\mathrm{mod}}(\lambda_j, i) \frac{a_{670} + a_{765} + a_{865}}{a_{670}R_{cor}(670, i) + a_{765}R_{cor}(765, i) + a_{865}R_{cor}(865, i)}. \tag{A.11}$$

When computing the lookup table for ϵ_e, geometric conditions, i.e., the triplet (θ_0, θ, ϕ), these are supposed to be identical for each band. Within a POLDER

measurement sequence (i.e., a set of viewing directions), however, the measurements are not made simultaneously in all the spectral bands because of the specific design of the POLDER instrument. A fine correction on ϵ_e is therefore necessary. The correction factor is defined by:

$$\Delta R(\lambda_j, i) = \frac{P(\gamma^{\lambda_j,i}) \cos \theta^{765,i}}{P(\gamma^{765,i}) \cos \theta^{\lambda_j,i}},$$

(A.12)

where $P(\gamma^{\lambda_j,i})$ and $P(\gamma^{765,i})$ are the values of the phase function of model Xd_x for scattering angles $\gamma^{\lambda_j,i}$ and $\gamma^{765,i}$, respectively, and $\cos \theta^{\lambda_j,i}$ and $\cos \theta^{765,i}$ are the cosine of the viewing zenith angle of bands at λ_j and 765 nm, respectively, for viewing direction i. In this correction, the band at 765 nm is considered as representative of the three red and NIR bands (670, 765, and 865 nm) used in the atmospheric correction scheme.

The correction term that accounts for aerosol contribution in each ocean-colour band $j (j = 1, 2, 3)$ is then easily computed as follows:

$$R_{aer}(\lambda_j, i) = \epsilon_e(\lambda_j, i) R_e(\lambda_j, i) \Delta R(\lambda_j, i).$$

(A.13)

This allows one to estimate the contribution R_w of the water body to R_t, i.e., the last term in Equation A.2:

$$R_w(\lambda_j, i) = R_t(\lambda_j, i) - R_{mol}(\lambda_j, i) - R_{gm}(\lambda_j, i) - T_0(\lambda_j, i) T(\lambda_j, i) R_g - R_{atm}(\lambda_j, i).$$

(A.14)

Finally the marine reflectance is obtained for each viewing direction i in each ocean-colour band j:

$$[\rho_w(\lambda_j, i)]_N = \frac{R_w(\lambda_j, i)}{\cos \theta_0 t_0(\lambda_j, i) t(\lambda_j, i) + S(\lambda_j) R_w(\lambda_j, i)} - [\rho_{wc}(\lambda_j)]_N$$

(A.15)

A.7 Sun Glint Correction

For a given POLDER pixel, 12 or 13 viewing directions are available. A couple of directions are highly contaminated by sun-glint and are thus rejected. Still some of the directions considered as sun-glint free are slightly contaminated. The correction term for those directions is $T_0 T R_g$. The sun glint reflectance, R_g, is considered spectrally flat and computed as a function of wind speed, U, using the Cox and Munk (1954) model:

$$R_g(\theta_0, \theta, \phi, U) = \frac{\pi P(Z(U)) R_f(\gamma)}{4 \cos^4 \beta \cos \theta_0}$$

(A.16)

where R_f is the reflection coefficient at the air-sea interface for the scattering angle γ, β is the wave inclination, and $P(Z(U))$ is the Gaussian slope distribution as given by Cox and Munk (1954). Surface wind speed is obtained from meteorological data. The correction is applied for $R_g < 0.005$. For higher R_g values the model is not precise enough (due to uncertainties on surface wind speed, intrinsic variability of Fresnel reflection on a rough surface).

A.8 Whitecap Correction

When sea surface agitation becomes important, generally for a wind speed above 8 m/s, the air-sea interface can be contaminated by whitecaps (Koepke, 1984; Monahan and O'Muircheartaigh, 1986). An empirical relationship between surface density of whitecaps and wind speed has been provided by these authors and is widely used:

$$S_{wc} = 2.95 \times 10^{-6} U^{3.52} \tag{A.17}$$

where S_{wc} is the fraction of the sea surface covered with whitecaps and U is expressed in m/s. Whitecap reflectance has been measured *in situ* and its mean value is generally considered to be equal to 0.22 in the visible. More recently *in situ* or aircraft measurements (Frouin, *et al.*, 1996; Moore, *et al.*, 2000; Nicolas *et al.*, 2001) have indicated that whitecap reflectance cannot be considered as spectrally flat in the visible and NIR region.

Therefore, in the algorithm the model used for whitecap reflectance is:

$$[\rho_{wc}(\lambda_j)]_N = 0.22\epsilon_{wc}(\lambda_j)S_{wc} \tag{A.18}$$

where $\epsilon_{wc}(\lambda_j)$ is a spectral whitecap coefficient defined for each band from 443 to 865 nm. Surface wind speed to compute S_{wc} comes from meteorological data, and a wind speed threshold of 8 m/s is used below which whitecap reflectance is neglected.

In the algorithm aerosol optical inversion module, if $R_{cor}(865) < 0$ and whitecap reflectance used in Equation A.3 is not 0, then ρ_{wc} is progressively lowered until $R_{cor}(865)$ becomes positive. If $R_{cor}(865)$ is still negative, no aerosol correction and no whitecap correction are made (but the pixel can still be rejected later in the processing line).

Other Atmospheric Correction Algorithms

Howard R. Gordon, Menghua Wang and Robert Frouin

B.1 Introduction

There has been significant progress in developing other approaches for atmospheric correction, in particular, in dealing with cases for either the strongly-absorbing aerosols and/or waters with non-negligible NIR ocean contributions. These algorithms are used regionally, and are not the focus of this report. Brief descriptions of these algorithms are provided below.

The algorithms described in Sections 2.1 to 2.4 are applicable only in the presence of non-absorbing or weakly-absorbing aerosols (used for global ocean-colour data processing). They cannot produce acceptable results in the presence of strongly-absorbing aerosols. In addition, they all require that $\rho_w(\lambda)$ be negligible in the NIR bands. These conditions are not always met. Two observations (Gordon, 1997) indicate how the algorithm is confounded in the presence of strongly-absorbing aerosols:

1. Although aerosol absorption can seriously reduce $\rho_a(\lambda) + \rho_{ra}(\lambda)$ in the visible, it is not possible on the basis of the observed TOA radiance in the NIR to infer the presence of aerosol absorption, because the spectral variation of $\rho_a(\lambda) + \rho_{ra}(\lambda)$ in the NIR depends mostly on the aerosol's size distribution; and

2. The vertical distribution of strongly-absorbing aerosols profoundly influences their TOA reflectance in the visible (especially in the blue) but not in the NIR. In the case of a mineral aerosol such as Saharan dust transported over large distances over the ocean by the winds, there is the additional complication that the dust is coloured, i.e., the absorption properties of the material itself vary strongly with the wavelength.

The fact that the absorption properties cannot be determined on the basis of the observations of $\rho_a(\lambda) + \rho_{ra}(\lambda)$ in the NIR means that observations in the visible are required as well. However, in the visible (especially in the blue) $\rho_w(\lambda)$ can be significant, and cannot be estimated *a priori*. This suggests that the retrieval of $\rho_w(\lambda)$ and the atmospheric correction (retrieval of $\rho_a(\lambda) + \rho_{ra}(\lambda)$) must be carried

out simultaneously. As retrieval of $\rho_a(\lambda) + \rho_{ra}(\lambda)$ in the existing algorithm requires aerosol models, retrieval of $\rho_w(\lambda)$ will require an optical model of the ocean. Two algorithms, based on simultaneous determination of oceanic and atmospheric properties that show promise in dealing with absorbing aerosols, have been developed by Gordon and co-workers (Gordon *et al.*, 1997; Chomko and Gordon, 1998).

The requirement for $\rho_w(\lambda) \approx 0$ in the NIR fails in turbid coastal waters. A remedy is to base atmospheric correction on spectral bands at longer wavelengths, where the absorption of water is greater than in the NIR and the corresponding $\rho_w(\lambda)$ is smaller: the shortwave infrared (SWIR) (Wang and Shi, 2005; Wang, 2007). In addition, the neural network approach for deriving ocean-colour products for regional applications also show some good results (Jamet *et al.*, 2005; Brajard *et al.*, 2006), in particular, for coastal regions with Case-2 waters (Schroeder *et al.*, 2007).

B.2 Spectral Matching Algorithm

The 'spectral matching algorithm' (SMA) is described in detail in Gordon *et al.*, (1997). In this algorithm, the properties of the ocean and the atmosphere are retrieved simultaneously. Briefly, assuming that $[\rho_w(\lambda_{NIR})]_N = 0$, $\rho_t(\lambda_{NIR}) - \rho_r(\lambda_{NIR})$ provides $\rho_a(\lambda_{NIR}) + \rho_{ra}(\lambda_{NIR})$. Given an aerosol model (the ith) one can find the value of the aerosol optical depth, $\tau_a^{(i)}(\lambda_{NIR})$, that reproduces $\rho_a(\lambda_{NIR}) + \rho_{ra}(\lambda_{NIR})$. Then from $\tau_a^{(i)}(\lambda_{NIR})$ and the model $\rho_a(\lambda_j) + \rho_{ra}(\lambda_j)$ can be determined as well $\tau_a^{(i)}(\lambda_j)$ for all spectral bands λ_j. This provides the quantity $\rho_w^{(i)}(\lambda_j)$, retrieved assuming that the ith aerosol model is correct. At this point the Gordon *et al.* (1988b) two-parameter model of the Case-1 water-leaving reflectance that uses the pigment concentration, C and a pigment-related scattering parameter at 550 nm, b^0, is employed to compute $\rho_w(\lambda_j)$ for a discrete set of values of C and b^0 that fall within the typical range of variation. The residual

$$\delta(i, C, b^0) = \sum_{j=1}^{n} \left[\frac{\rho_w(\lambda_j) - \rho_w^{(i)}(\lambda_j)}{\rho_w(\lambda_j)} \right]^2, \tag{B.1}$$

where n is the number of visible wavelengths, is then computed for each model and set of ocean parameters. The set of parameters i, C, and b^0, that yield the smallest $\delta(i, C, b^0)$ is chosen as the best, i.e., the solution the problem; however, as it is unlikely that the 'correct' model is one of the set of candidates, Gordon *et al.*, (1997) suggested averaging for the ten best retrievals (ten retrievals with the lowest values of $\delta(i, C, b^0)$) to obtain the retrieved ocean and aerosol parameters. Extensive tests using simulated pseudo data with strongly-absorbing aerosols suggest that this approach is capable of excellent retrievals in the presence of either weakly- or strongly-absorbing aerosols. Of particular importance is the fact that the algorithm has no difficulty indicating the presence of strongly-absorbing aerosols. The algorithm can also incorporate vertical structure by having candidate models with any

prescribed vertical structure. An important feature of this algorithm is that it can be configured to use the same LUTs as the standard algorithm, and therefore could be run concurrently. An unattractive feature of the algorithm is that it requires realistic aerosol models to effect the correction, i.e., the better the models approximate the real aerosol, the better the parameter retrievals. Obviously the results also depend on the quality of the ocean model.

Moulin *et al.* (2001a, 2001b) and Banzon *et al.* (2004) applied this method to imagery contaminated with Saharan dust, much improving the retrievals of C.

B.3   Spectral Optimization Algorithm

The 'spectral optimization algorithm' (SOA) is described in detail in Chomko and Gordon (1998). As in the spectral matching algorithm, the properties of the ocean and the atmosphere are retrieved simultaneously. In contrast to the spectral matching algorithm, no attempt is made to use realistic aerosol models, i.e., aerosol models are described by the overly-simple power-law size distributions (number between r and $r + dr \propto r^{-(v+1)}$) are employed to derive the aerosol properties. Briefly, for a given value of the parameter v, assuming the particles are spherical, and ignoring the aerosol vertical distribution for the moment, the aerosol reflectance $\rho_a(\lambda) + \rho_{ra}(\lambda)$ only depends on the real (m_r) and imaginary (m_i) parts of the aerosol refractive index and $\tau_a(\lambda_{NIR})$. The values of m_r and m_i are assumed to be independent of λ, so such a model will apply to wavelength-independent absorbing aerosols only, e.g., carbonaceous. As in the spectral matching algorithm, the water contribution to the TOA reflectance depends on the parameters C, and b^0, through the Gordon *et al.* (1988b) reflectance model. Standard optimization procedures are then used to determine the values of these parameters using an equation similar to Equation B.1, i.e., minimizing $\delta(v, \tau_a, m_r, m_i, C, b^0)$, where $\tau_a = \tau_a(\lambda_{NIR})$.

Application to SeaWiFS imagery off the U.S. east coast has been presented by Chomko and Gordon (2001). The algorithm showed consistent retrieved water properties between days with turbid and clear atmospheres. The algorithm was improved by Chomko *et al.* (2003) by replacing the bio-optical model with a more robust model (Garver and Siegel, 1997; Maritorena *et al.*, 2002) and showed excellent retrievals of both C and the absorption by detrital material. It was further modified by Kuchinke *et al.* (2009a; 2009b) for application to Case-2 waters.

B.4   The SWIR Algorithm

For dealing with the turbid waters in the coastal regions, where there are often significant ocean contributions in the NIR bands, Wang (2007) proposed an atmospheric correction algorithm using the shortwave infrared (SWIR) bands. At the SWIR wavelengths, ocean water has much stronger absorption than that at the NIR bands (Hale

and Querry, 1973), thus the black ocean assumption is generally valid at the SWIR bands, even for very turbid ocean waters. The algorithm basically operates in the same way as that of Gordon and Wang (1994a), but the two NIR bands (e.g. MODIS 748 and 869 nm) are replaced with two SWIR bands (e.g. MODIS 1240 and 2130 nm) for atmospheric correction. Wang *et al.* (2009) evaluated the performance of the SWIR algorithm using both MODIS data and *in situ* measurements, and Wang and Shi (2005) and Wang *et al.* (2007) demonstrated applications for extremely turbid waters in various coastal regions. In addition, ocean-colour products derived from the SWIR-based atmospheric correction have been shown to have various important applications, such as studying storm-driven phytoplankton blooms (Shi and Wang, 2007; Liu *et al.*, 2009) and storm-induced sediment re-suspension (Shi and Wang, 2008), storm-water runoff plume detection (Nezlin, *et al.* 2008), inland fresh water monitoring and management (Wang and Shi, 2008), and flood-driven river plume dynamics (Shi and Wang, 2009). With the SWIR method, NIR ocean contributions can also be derived accurately and used for retrieval of ocean properties such as sediment concentration.

B.5   Neural Network Approach

Atmospheric correction using the neural network approach has also shown promising results. In contrast to standard approaches, but in line with spectral matching and optimization algorithms, the correction is not based on decoupling atmospheric and oceanic effects, and it takes into account all the spectral information in the measurements. The neural network methodology is used either to model the radiation transfer in the ocean-atmosphere system (direct modelling), or to achieve a mapping between top-of-atmosphere measurements and bottom-of-atmosphere reflectance or geophysical parameters (inverse modelling). The basic advantages of neural networks are exploited, namely their good approximation properties, their robustness to noise, and their rapidity of execution. However, the neural network approach requires realistic training data sets (usually regionally dependent) for the algorithm tuning, and it may be difficult to produce accurate global ocean-colour products.

In the neuro-variational method proposed by Jamet *et al.* (2005) and refined by Brajard *et al.* (2006), the TOA signal is modelled by the use of multi-layer perceptrons. One perceptron is used for atmospheric reflectance, one for water reflectance, and one for atmospheric transmittance. Atmospheric and oceanic parameters affecting the measured signal, namely aerosol index of refraction, size distribution, and optical thickness, chlorophyll-a concentration, and hydrosol scattering, are retrieved using a variational inversion scheme. The distance between observed reflectance and that calculated at several wavelengths is minimized, the control parameters being the oceanic and atmospheric parameters. An iterative cost function formulation

and minimization phases, controlled separately by oceanic and atmospheric parameters, allows one to handle absorbing aerosols. A limited evaluation against *in situ* measurements has demonstrated acceptable chlorophyll-*a* concentration retrievals, consistent with standard SeaWiFS results.

In the inverse model parameterization developed for MERIS and described in Schroeder *et al.* (2007), the TOA signature, solar and viewing geometries, and environmental data (surface pressure and wind speed) are used as data entry in a fully connected, forward-feed, neural network. The output data are the spectral bottom-of-atmosphere reflectance and, as a by-product, aerosol optical thickness. Situations of Case-2 waters were simulated and used in the determination of the free parameters of the network, which makes an algorithm adapted to those optically-complex waters. For the marine reflectance product, a mean absolute percentage error of 18% in the spectral range 412—710 nm was obtained in comparisons with *in situ* measurements. The improvement in accuracy was substantial in the blue part of the spectrum when neural network estimates were compared with the standard MERIS Level-2 marine reflectance product.

In the function field methodology proposed by Pelletier and Frouin (2006) and Frouin and Pelletier (2007), the TOA reflectance vectors, after correction for molecular effects, are considered as explanatory variables conditioned by the angular geometry. The inverse problem, therefore, is viewed as a collection of similar inverse problems, continuously indexed by the angular variables. The solution is in the form of a field of non-linear regression models over the set of permitted values for the angular variables. Each value of the field is a regression model that performs a direct mapping of the TOA reflectance to the chlorophyll-*a* concentration (Pelletier and Frouin, 2006) or the marine reflectance (Frouin and Pelletier, 2007). The selected models, for reasons of approximation theory, are fields of shifted ridge functions. The fields constructed on synthetic data for Case-1 waters are robust to noise, they handle situations of weakly and strongly-absorbing aerosols well, and the retrievals are accurate in both oligotrophic and productive waters. The methodology was applied successfully to satellite imagery, but needs to be further tested and evaluated against *in situ* measurements. Extension to the retrieval of other variables such as yellow substance absorption and sediment concentration, is possible.

In the algorithm proposed by Gross-Colzy *et al.* (2007a), the satellite reflectance is first decomposed into principal components. The components sensitive to the ocean signal are then combined to retrieve the principal components of the marine reflectance. This allows a reconstruction of the marine reflectance and, therefore, an estimate of the marine reflectance. Neural network methodology is used to approximate the non-linear functions that relate the useful principal components of satellite reflectance to the principal components of marine reflectance. Keeping only the ocean-sensitive principal components of satellite reflectance reduces the influence of the atmosphere, making the non-linear mapping accurate. The algorithm performs atmospheric correction in the presence of a wide range of aerosol contents

and types, including absorbing mixtures, for the full range of water properties (Case-1 and Case-2), and marine reflectance is retrieved with good theoretical accuracy. By operating with principal components, the algorithm is minimally influenced by biases in radiometric calibration (only inter-band calibration needs to be accurate), making it well adapted to provide consistency across sensors and continuity in the quality of the marine reflectance (Gross-Colzy *et al.*, 2007b).

<div style="border:1px solid #000; padding:4px;">

Appendix C

</div>

Atmospheric Diffuse Transmittance

Howard R. Gordon, Pierre-Yves Deschamps, Menghua Wang and Robert Frouin

C.1 Introduction

In the remote sensing of ocean colour, we are interested in the water-leaving radiance $L_w(\theta, \phi)$, i.e. the component of the radiance leaving the sea surface that was transmitted through the interface from below the ocean surface. The radiance just below the sea surface is $L_u(\theta', \phi)$, where θ' and θ are related by the law of refraction, i.e., $\sin\theta = m\sin\theta'$. $L_w(\theta, \phi)$ and $L_u(\theta', \phi)$ are related by

$$L_w(\theta, \phi) = \frac{T_f(\theta, \theta')}{m^2} L_u(\theta', \phi), \tag{C.1}$$

where $T_f(\theta, \theta')$ is the Fresnel reflectance of the air-sea interface. This is not the only component of the upward radiance just above the sea surface: the sky radiance $L_{sky}(\pi - \theta, \phi)$ will be Fresnel-reflected upward by the sea surface adding $L_{sky}(\pi - \theta, \phi)[1 - T_f(\theta, \theta')]$ to the upward radiance just above the sea surface. Note that $L_{sky}(\pi - \theta, \phi)$ is the totality of sky radiance, i.e., it includes any and all-multiple reflections from the interface. The total radiance just above the sea surface $L_{w(total)}(\theta, \phi)$ is

$$L_{w(total)}(\theta, \phi) = L_{sky}(\pi - \theta, \phi)[1 - T_f(\theta, \theta')] + L_w(\theta, \phi). \tag{C.2}$$

If the sea surface is rough, the first term is replaced by an integral over solid angle, as is the right-hand-side of Equation C.1. These are related to the radiance measured at the top of the atmosphere $L_t(\theta, \phi)$ by

$$L_t(\theta, \phi) = L_{path}(\theta, \phi) + t(\theta, \phi)L_{w(total)}(\theta, \phi), \tag{C.3}$$

where $L_{path}(\theta, \phi)$ is the path radiance, i.e., the radiance generated by scattering within the atmosphere along the path of sight and $t(\theta, \phi)$ is usually referred to as the diffuse transmittance. Writing this out in detail, we have

$$L_t(\theta, \phi) = L_{path}(\theta, \phi) + t(\theta, \phi)L_{sky}(\pi - \theta, \phi)[1 - T_f(\theta, \theta')] + t(\theta, \phi)L_w(\theta, \phi). \tag{C.4}$$

In the Gordon and Wang (1994a) atmospheric correction scheme the path radiance is defined to include sky radiance reflected from the interface, i.e.,

$$L_{\text{path}}^{GW}(\theta, \phi) = L_{\text{path}}(\theta, \phi) + t(\theta, \phi)L_{sky}(\pi - \theta, \phi)[1 - T_f(\theta, \theta')]. \quad (C.5)$$

The Gordon-Wang lookup tables for $L_{\text{path}}^{GW}(\theta, \phi)$ were generated by solving the radiative transfer equation for an atmosphere illuminated from the top by the sun and bounded by a Fresnel-reflecting interface over a totally absorbing medium, i.e., any photons penetrating the interface are lost. Thus, if there are photons incident both from the sun and from beneath the surface (actually reflected upward from beneath the water surface) in the Gordon-Wang definition,

$$L_t(\theta, \phi) = L_{\text{path}}^{GW}(\theta, \phi) + t(\theta, \phi)L_w(\theta, \phi). \quad (C.6)$$

C.2   Formal Definition of Diffuse Transmittance

Using Equations C.2 and C.3, the diffuse transmittance can be defined as

$$t\left(\hat{\xi}\right) = \frac{L_w^{(TOA)}\left(\hat{\xi}\right)}{L_w\left(\hat{\xi}\right)}, \quad (C.7)$$

where $L_w(\hat{\xi})$ is the radiance leaving the surface in the direction $\hat{\xi}$, $L_w^{(TOA)}(\hat{\xi})$ is the radiance originating in the water and exiting the TOA in the direction $\hat{\xi}$, $\hat{\xi} = \hat{i}\sin\theta\cos\phi + \hat{j}\sin\theta\sin\phi + \hat{k}\cos\theta$ is in the propagation direction, and $\hat{i}$, $\hat{j}$, $\hat{k}$ are Cartesian unit vectors. Yang and Gordon (1997) provided a rigorous framework based on the reciprocity principle in which to compute $t(\hat{\xi})$. They showed that $t(\hat{\xi})$ is not just a function of the atmospheric properties, but also depends on the angular distribution of $L_w(\hat{\xi})$ itself. In general, this distribution is unknown. If it were known, the procedure for computing $t(\hat{\xi})$ would be straightforward: consider the atmosphere bounded by a Fresnel-reflecting, but totally transparent ocean, introduce a radiance $L_w(\hat{\xi})$ with the appropriate angular distribution just above the sea surface, and compute the radiance leaving the TOA, $L_w^{(TOA)}(\hat{\xi})$. In practice simplifying assumptions have been used to effect this computation. Gordon and Wang (1994a) assume that the upwelling radiance just beneath the sea surface $L_u(\hat{\xi})$ is uniform, i.e., independent of direction, while the POLDER team (University of Lille) assume that $L_w(\hat{\xi})$ is uniform. The resulting $t(\hat{\xi})$, and hence the retrieved value of $L_w(\hat{\xi})$, will depend on which assumption is employed. When either $L_u(\hat{\xi})$ or $L_w(\hat{\xi})$ are assumed to be uniform, the associated $t(\hat{\xi})$ will be denoted by $t^*(\hat{\xi})$. In reality, however, neither $L_u(\hat{\xi})$ nor $L_w(\hat{\xi})$ are completely uniform.

Yang and Gordon (1997) show that when $L_u(\hat{\xi})$ is uniform, $t(\hat{\xi})$ (denoted by t^* to differentiate it from t) can be computed from

$$t^{*(GW)}\left(-\hat{\xi}_0\right) = \frac{E_d\left(\vec{\rho}_B^-\right)}{F_0\left|\hat{\xi}_0 \bullet \hat{n}_T\right|T_f\left(\hat{\xi}_0\right)} \quad (C.8)$$

where $E_d\left(\vec{\rho}_{\bar{B}}\right)$ is the downward irradiance at a position just below the sea surface specified by $\vec{\rho}_{\bar{B}}$, when the TOA is illuminated with the solar beam (irradiance F_0) propagating in the direction $\hat{\xi}_0$. The POLDER team computation of $t\left(\hat{\xi}\right)$ is given by

$$t^{*(UL)}\left(-\hat{\xi}_0\right) = \frac{E_d\left(\vec{\rho}_B^+\right)}{F_0\left|\hat{\xi}_0 \bullet \hat{n}_T\right|} \tag{C.9}$$

where $E_d\left(\vec{\rho}_B^+\right)$ is the downward irradiance at a position just above the sea surface specified by $\vec{\rho}_B^+$, when the TOA is illuminated with the solar beam (irradiance F_0) propagating in the direction $\hat{\xi}_0$. For completeness, we provide the associated equations valid for any angular distribution of $L_u\left(\hat{\xi}\right)$ and $L_w\left(\hat{\xi}_0\right)$:

$$t^{(GW)}\left(-\hat{\xi}_0\right) = \frac{1}{F_0\left|\hat{\xi}_0 \bullet \hat{n}_T\right| T_f\left(\hat{\xi}_0\right)} \int \left|\hat{\xi} \bullet \hat{n}_T\right| L_1\left(\vec{\rho}_B^-,\hat{\xi}\right) \frac{L_u\left(\vec{\rho}_B^-,-\hat{\xi}\right)}{L_u\left(\vec{\rho}_B^-,-\hat{\xi}_0\right)} d\Omega\left(\hat{\xi}\right)$$
$$\tag{C.10}$$

$$t^{(UL)}\left(-\hat{\xi}_0\right) = \frac{1}{F_0\left|\hat{\xi}_0 \bullet \hat{n}_T\right|} \int \left|\hat{\xi} \bullet \hat{n}_T\right| L_1\left(\vec{\rho}_B^+,\hat{\xi}\right) \frac{L_u\left(\vec{\rho}_B^+,-\hat{\xi}\right)}{L_u\left(\vec{\rho}_B^+,-\hat{\xi}_0\right)} d\Omega\left(\hat{\xi}\right) \tag{C.11}$$

where $L_1\left(\vec{\rho}_B^{\pm},\hat{\xi}\right)$ is radiance just above $(+)$ or just beneath $(-)$ the sea surface when the TOA is illuminated with the solar beam (irradiance F_0) propagating in the direction $\hat{\xi}_0$. Over all, the integrations are in the downward direction of $\hat{\xi}$. Given either $L_u(\xi)$ just below the water surface, or $L_w(\xi)$ just above the water surface, exact values of the diffuse transmittance in any direction can be obtained from these equations. Figure C.1 provides example results for the ratio of $t^{(UL)}/t^{(GW)}$ as a function of the solar (or sensor) zenith angle for wavelengths of 443 and 555 nm and for the M80 aerosols with the AOT at 865 nm of 0.1 and 0.2. Results in Figure C.1 show that for $\theta \leq 70°$ the difference between $t^{(UL)}$ and $t^{(GW)}$ are within ~2%. Thus, we have used these relationships (Figure C.1) for making corrections in conversion between two systems in deriving the normalized water-leaving radiance.
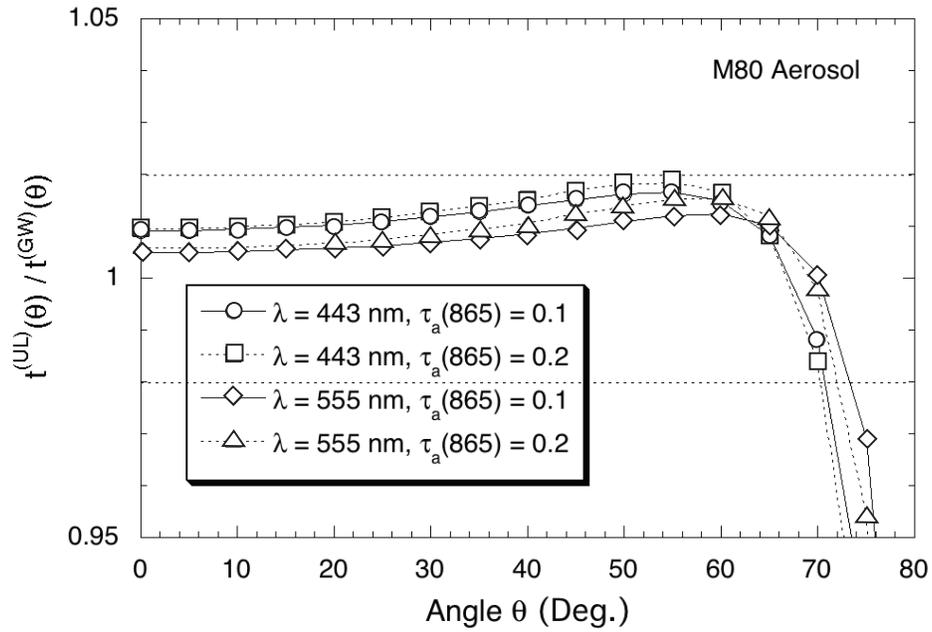
Figure C.1   The ratio of the atmospheric diffuse transmittance computed by assuming the upward radiance uniformly distributed just above the surface ($t^{(UL)}$) and just below the surface ($t^{(GW)}$) as a function of the solar (or sensor) zenith angle for wavelengths of 443 and 555 nm and for the M80 aerosols with the AOT at 865 nm of 0.1 and 0.2.

Ocean Bidirectional Reflectance Distribution Function

André Morel, Howard R. Gordon and Menghua Wang

D.1 Introduction

Developed through a series of papers over many years, the ocean bi-directional reflectance distribution function (BRDF) of ocean water-leaving radiances has been studied by many scientists (Gordon and Clark, 1981; Morel and Gentili, 1991; 1993; 1996; Gordon, 2005; Wang, 2006b). Key in this development is the theoretical concept of the normalized water-leaving radiance, defined as the water-leaving radiance that would be viewed at nadir when the Sun is at the zenith and mean Earth-Sun distance, with no intervening of atmosphere. The initial definition of the normalized water-leaving radiance (measured at the wavelength λ and solar-zenith, sensor-zenith, and relative azimuth angles of $\theta_0, \theta,$ and $\Delta\phi$) by Gordon and Clark (1981)

$$[L_w(\lambda, \theta_0, \theta, \Delta\phi)]_N = L_w(\lambda, \theta_0, \theta, \Delta\phi) \frac{\bar{F}_0(\lambda)}{E_d^{(+)}(\lambda, \theta_0)} \cong \left(\frac{d}{d_0}\right)^2 \frac{L_w(\lambda, \theta_0, \theta, \Delta\phi)}{t(\lambda, \theta_0)\cos\theta_0},$$

(D.1)

accounts for variations between mean extraterrestrial solar irradiance $\bar{F}_0(\lambda)$ and irradiance incident on the sea surface $E_d^{(+)}(\lambda, \theta_0)$ due to solar zenith angle θ_0, atmospheric transmittance $t(\lambda, \theta_0)$, and effects of variations in Earth-Sun distance $(d/d_0)^2$ during the year. Morel *et al.* (2002) and Morel and Gentili (1991; 1993; 1996) extended the definition to account for additional effects due to angular variations in reflection and refraction at the sea surface and for the in-water BRDF, introducing a quantity they dubbed the exact normalized water-leaving radiance, $[L_w(\lambda)]_N^{Exact}$, i.e.,

$$[L_w(\lambda)]_N^{Exact} = [L_w(\lambda, \theta_0, \theta, \Delta\phi)]_N \left\{(f/Q)_{Eff}\right\} \left[\frac{\Re_0(\lambda, \tau_a, W)}{\Re(\lambda, \theta_0, \theta, \tau_a, W)}\right],$$

(D.2)

where term $(f/Q)_{Eff}$ represents effects of the in-water ocean BRDF (Morel and Gentili, 1996), while the term $\Re$ ratio accounts for angular variations in all effects of reflection and refraction of radiance at the sea surface. In effect, this representation separates BRDF effects attributed to the ocean surface (term with $\Re$ ratio) from

effects associated with the angular distribution of upwelling radiance just beneath the water surface (Morel and Gentili, 1996)

$$\{(f/Q)_{Eff}\} = \left\{ \left(\frac{f_0(\lambda, IOP)}{Q_0(\lambda, IOP)} \right) \Big/ \left(\frac{f(\lambda, \theta_0, IOP)}{Q(\lambda, \theta_0, \theta, \Delta\phi, IOP)} \right) \right\} \tag{D.3}$$

which depends on solar-sensor geometry and the ocean inherent optical properties (IOPs). In the above, f is a coefficient that relates ocean upwelling irradiance reflectance to the ocean inherent optical properties and the Q factor is defined as ratio of the upwelling irradiance just beneath the ocean surface to the upwelling radiance just beneath the ocean surface (Morel and Gentili, 1996). f_0 and Q_0 are defined for $f(\lambda, \theta_0 = 0, IOP)$ and $Q(\lambda, \theta_0 = 0, \theta = 0, IOP)$, respectively. Note that, for a uniform angular distribution of upwelling radiance just beneath the ocean surface, $\{(f/Q)_{Eff}\} \equiv 1$.

D.2 Ocean Surface Effects

In Equation D.2, the factor $\mathfrak{R}(\lambda, \theta_0, \theta, \tau_a, W)$ is given by Morel and Gentili (1996)

$$\mathfrak{R}(\lambda, \theta_0, \theta, \tau_a, W) = \left[\frac{1 - \bar{\rho}_f(\lambda, \theta_0, \tau_a, W)}{1 - \bar{r}R(\lambda, \theta_0)} \right] \left[\frac{1 - \rho_f(\lambda, \theta, W)}{m^2} \right], \tag{D.4}$$

and $\mathfrak{R}_0(\lambda, \tau_a, W)$ is defined for $\mathfrak{R}(\lambda, \theta_0 = 0, \theta = 0, \tau_a, W)$. $\bar{\rho}_f(\lambda, \theta_0, \tau_a, W)$ and $\rho_f(\lambda, \theta, W)$ are the surface Fresnel reflectivity for irradiance (from Sun and sky) and radiance, respectively, corresponding to a given spectral wavelength λ, solar-sensor geometry (θ_0 and θ), aerosol optical property (aerosol model and optical thickness τ_a), and surface wind speed W. In Equation D.4, $R(\lambda, \theta_0)$ is the irradiance reflectance backscattered from the water just beneath the surface, $\bar{r}$ is the reflectivity (spherical albedo) of upward irradiance by the surface (irradiance incident upward to the surface from below the interface), and m is the refractive index of water. We can further define $\mathfrak{R}(\lambda, \theta_0, \theta, \tau_a, W)$ as a product of functions that are dependent separately on the solar and viewing angle alone, i.e.,

$$\mathfrak{R}(\lambda, \theta_0, \theta, \tau_a, W) = \mathfrak{R}^{(Sun)}(\lambda, \theta_0, \tau_a, W)\mathfrak{R}^{(View)}(\lambda, \theta, W), \tag{D.5}$$

where

$$\mathfrak{R}^{(Sun)}(\lambda, \theta_0, \tau_a, W) = \frac{1 - \bar{\rho}_f(\lambda, \theta_0, \tau_a, W)}{1 - \bar{r}R(\lambda, \theta_0)} \tag{D.6}$$

and

$$\mathfrak{R}^{(View)}(\lambda, \theta, W) = \frac{1 - \rho_f(\lambda, \theta, W)}{m^2}. \tag{D.7}$$

The first term in Equation D.5, $\mathfrak{R}^{(Sun)}(\lambda, \theta_0, \tau_a, W)$, corresponds to the effects of the air-water interface for the downward irradiance contribution across from above to beneath the surface, while the second term in Equation D.5, $\mathfrak{R}^{(View)}(\lambda, \theta, W)$, is the

effects of the air-water interface for the upward radiance across from beneath to above the surface. We can thus re-write Equation D.2 as

$$[L_w(\lambda)]_N^{Exact} = [L_w(\lambda, \theta_0, \theta)]_N \left\{(f/Q)_{Eff}\right\} \left[\frac{\mathfrak{R}_0^{(Sun)}(\lambda, \tau_a, W)}{\mathfrak{R}^{(Sun)}(\lambda, \theta_0, \tau_a, W)}\right] \left[\frac{\mathfrak{R}_0^{(View)}(\lambda, W)}{R^{(View)}(\lambda, \theta, W)}\right].$$
(D.8)

Recently, it has been found that, for cases with θ_0 and θ up to ~60°, the third term in Equation D.8, $\left[\mathfrak{R}_0^{(Sun)}(\lambda, \tau_a, W)/\mathfrak{R}^{(Sun)}(\lambda, \theta_0, \tau_a, W)\right]$, depends only on the properties of the ocean surface and not the atmosphere (Wang, 2006b), while the term $\left[\mathfrak{R}_0^{(View)}(\lambda, W)/R^{(View)}(\lambda, \theta, W)\right]$ can be computed accurately with a flat ocean surface (i.e., independent of the wind speed) (Gordon, 2005). Thus, the effects in angular variation of the surface reflection and refraction on the normalized water-leaving radiance ($\mathfrak{R}$ terms in Equation D.8) can be calculated easily (Gordon, 2005; Wang, 2006b). Figure D.1 shows typical cases of two $\mathfrak{R}$ terms in Equation D.8. Figure D.1a shows $\left[\mathfrak{R}_0^{(Sun)}(\lambda, \tau_a, W)/\mathfrak{R}^{(Sun)}(\lambda, \theta_0, \tau_a, W)\right]$ (with a flat ocean surface) as a function of the solar-zenith angle for various wavelengths and for a case of the M80 model with aerosol optical thickness of 0.1, while Figure D.1b shows $\left[\mathfrak{R}_0^{(View)}(\lambda, W)/R^{(View)}(\lambda, \theta, W)\right]$ as a function of the sensor-zenith angle for various wind speeds.

D.3   In Water BRDF Effects

Within a water body, particularly close to the interface, the upward radiance field is not isotropic, so that a bidirectional reflectance distribution function (BRDF) has to be taken into account. Simple considerations help explain this non-isotropic character (see Morel *et al.*, 2002). The first consideration deals with the average number, $\tilde{n}$, of scattering events undergone by photons before they come back and reach the surface; the second one is related to the shape of the volume scattering function (VSF), particularly the shape of its backward lobe (which is particularly, but not exclusively, involved in the formation of the backward flux).

Morel and Gentili (1991) showed that $\tilde{n}$ is equal to $(1 - \varpi)^{-1}$, where ϖ is the single scattering albedo (i.e., the ratio (b/c) of the scattering coefficient to the attenuation coefficient). Therefore, when ϖ is small enough, single scattering prevails, and the upward radiance field tends to mimic the backward lobe of the VSF, centered on the anti-sun direction. If molecular backscattering prevails, with a round shaped backward lobe, the upward radiance field will thus remain quasi-isotropic. When non-negligible, the Raman effect with an almost isotropic VSF, acts in the same direction. Alternatively, if particle backscattering prevails, with a backward peaked lobe, the radiances coming from the anti-sun direction will be reinforced, so that the anisotropy will be increased.

In contrast, when particles are abundant, ϖ increases, thus $\tilde{n}$ may become high (for instance, photons experiencing 5 or 10 successive scattering events before they
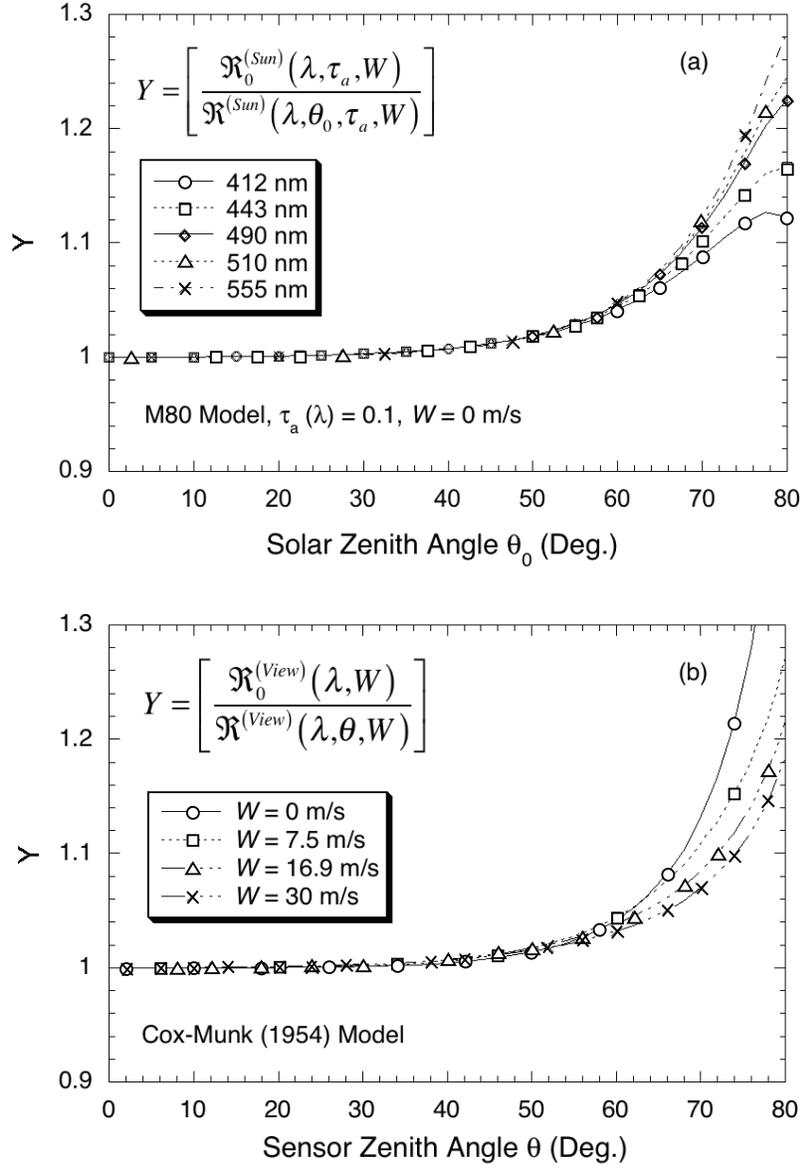
Figure D.1 Typical cases of two $\mathfrak{R}$ terms in Equation D.8 for (a) $[\mathfrak{R}_0^{(Sun)}(\lambda, \tau_a, W)/\mathfrak{R}^{(Sun)}(\lambda, \theta_0, \tau_a, W)]$ as a function of the solar-zenith angle for various wavelengths and (b) $\left[\mathfrak{R}_0^{(View)}(\lambda, W)/\mathfrak{R}^{(View)}(\lambda, \theta, W)\right]$ as a function of the sensor-zenith angle for various wind speeds.

can escape toward atmosphere, when ϖ = 0.8 or 0.9); in such cases (eutrophic waters or very turbid waters, appropriate wavelengths), the features of the backscattering lobe are smoothed out by the effect of multiple scattering, so that the upward light field will tend to be isotropic again (whatever the shape of the VSF). For most situations and wavelengths, however, the non-isotropic character of the upward radiance field will be the general rule.

As initially defined (Equation D.1), the normalized water-leaving radiance is still a quantity that depends on the observational conditions (through $\theta_0, \theta, \Delta\phi$). To fully respect the hypothetical geometry at the basis of the normalized water-leaving radiance (namely, radiance emerging from nadir, and sun at zenith), it was necessary to introduce a 'correction' to account for the in-water BRDF effect. This correction is represented by $(f/Q)_{Eff}$ in Equation D.2, as made explicit by Equation D.3. A detailed and illustrated description of the possible variations of the quantities f, Q, and of their ratio f/Q, are provided by Morel and Mueller (2002), to which the reader is referred for additional information. Briefly, these variations are as follows.

D.3.1   The f-Coefficient

The irradiance reflectance (or irradiance ratio), R, is defined as the ratio of the plane upward irradiance, E_u, to the plane downward irradiance, E_d, just below the surface: $R = E_u/E_d$; R is related to the IOP, essentially to the backscattering coefficient and the absorption coefficient, b_b and a, respectively. This relationship (wavelength λ omitted) is conveniently expressed under a simplified form as $R = f[b_b/a]$, where f is a (dimensionless) coefficient which depends on the illumination conditions, summarized by the sun zenith angle, θ_0, and on all the IOP; therefore it is written $R = f(\theta_0, \lambda, IOP)[b_b/a]$.

For a given λ, and a given set of IOP, f is always minimal when $\theta_0 = 0$; it is denoted f_0 in this case and its value amounts to about 1/3 (an historical value). With increasing θ_0, f increases monotonously, by up to 100% when θ_0 exceeds 60°. To the extent that in Case-1 waters, the IOP, including the VSF, can be, on average, related to the chlorophyll concentration, [Chl] (Morel *et al.*, 2002; Morel and Gentili, 2004), f can be regarded as a [Chl] dependent-coefficient (or inversely, [Chl] can be regarded as a substitute for all IOP when expressing f).

As a rule, both $f_0(\theta_0 = 0, [Chl], \lambda)$ and $f(\theta_0, [Chl], \lambda)$ increase for increasing [Chl]. In total, f_0 may exhibit values ranging from 0.28 to 0.45 (according to λ and [Chl]), whereas f varies within a wider range, from approximately 0.28 to 0.65. Figures 13.5 and 13.6 in Morel and Mueller (2002) display the variations of f as a function of the three variables (θ_0, λ, [Chl]). They also show the influence of the Raman effect on the f-parameter, which is not negligible especially in very clear waters (i.e., when [Chl] is low, for instance, 0.03 mg m^{-3}).

D.3.2 The Q-Coefficient

The Q-Coefficient describes the angular structure of the upward radiance field, as it stands immediately beneath the surface. It is defined via the relationship between any upward radiance (L_u) and the upward plane irradiance, E_u (actually the integral of the upward radiance field), so that

$$L_u(\lambda, \theta_0, \theta, \Delta\phi, IOP) = E_u(\lambda, \theta_0, IOP)/Q(\lambda, \theta_0, \theta, \Delta\phi, IOP).$$

Q is expressed as steradian, and would be constant and equal to π (sr), if the upward radiance field was uniform. In natural waters, values between 2 and 6, or more, are possible when all ($\theta - \Delta\phi$) directions are considered. For the upward directions within the Snell cone, i.e., for the upward radiances oriented in such a way that they are able to emerge, the range of variations in Q is more restricted. The particular Q-value, denoted $Q_0(\lambda, IOP)$, corresponds to both a sun at zenith and a viewing nadir angle $\theta = 0$ (i.e., when aiming at nadir); Q_0 is spectrally rather flat, but depends on [Chl] (a substitute for IOP in Case-1 waters); it increases from about π to 4.3, when [Chl] goes from 0.03 to 10 mg m^{-3} (Fig. 13.7 in Morel and Mueller, 2002). If θ_0, the solar zenith angle, increases, but the viewing angle, θ, remains null, the corresponding function for nadir (denoted Q_n)

$$Q_n = Q(\lambda, \theta_0, \theta = 0, \Delta\phi = 0, IOP)$$

also increases when θ_0 goes from 0° to 60°, by 30 to 100% depending on [Chl].

D.3.3 The Ratio f/Q

The particular value $f_0(\lambda, IOP)/Q_0(\lambda, IOP)$, which appears in Equation D.3, is built with the particular values of both f and Q, pertinent to an observation at nadir and when the sun is at zenith. This ratio varies within the range 0.075 and 0.120 (sr^{-1}), or actually within a narrower interval if only the blue and green radiations are considered. Indeed, the highest values occur for the red wavelengths (> 600 nm), and for the IOP corresponding to the lowest [Chl]; this enhancement is (partly) due to the influence of the Raman scattering in such waters when λ exceeds 560 nm.

For all geometries and conditions, the ratio $f(\lambda, \theta_0, IOP)/Q(\lambda, \theta_0, \theta, \Delta\phi, IOP)$ is always larger than $f_0(\lambda, IOP)/Q_0(\lambda, IOP)$, and experiences considerable variations with rather complex geometrical structures (see Fig. 13.10, Morel and Mueller, 2002). The highest values are always found in the principal plane, either in the direction of the sun ($\Delta\phi = 0$) or in the anti-sun ($\Delta\phi = \pi$) direction (depending on the shape of the VSF, i.e. on [Chl]). As f and Q experience concomitant increases when the solar zenith angle increases, their ratio is less varying than the two terms themselves. In total, variations to be expected for f/Q are within the limits 0.08 (low [Chl], blue wavelengths, high sun, quasi-vertical viewing) and about 0.16 (high [Chl], large sun angle and viewing angle approaching the critical angle).

D.3.4 The Corrective Term $(f/Q)_{Eff}$

Defined above (Equation D.3) as

$$\{f_0(\lambda, IOP)/Q_0(\lambda, IOP)\}/\{f(\lambda, \theta_0, IOP)/Q(\lambda, \theta_0, \theta, \Delta\phi, IOP)\},$$

this term is always smaller than 1, as the numerator is a minimal value of f/Q. Since the numerator and denominator (with λ and IOP in common) partly experience similar trends, the variations in the above ratio are thus more limited. In effect, this corrective term varies approximately between the upper value 1, and 0.6, in the worse conditions of observation (such as high [Chl], slant viewing angle, low sun elevation).

D.3.5 Additional Comments

All the above f and Q values have been obtained by solving the radiative transfer equation (RTE) for the coupled atmosphere-ocean system (Morel and Gentili, 1991; 1993; 1996). The numerical solutions of the RTE were obtained through Monte-Carlo simulations and also by using the invariant embedding method i.e. the HYDROLIGHT code developed by Mobley (1994). Only clear cloudless skies were considered. In the above expressions, the dependency on the illumination conditions was simply summarized by a single parameter, namely θ_0, the sun-zenith angle, whilst in reality these conditions are also determined by the aerosol content (and nature). A sensitivity study (Fig. 9 in Morel and Gentili, 1996) showed that the influence of the aerosol optical thickness on f/Q is weak ($< 10\%$) and thus can be neglected. The same can be said about the wind speed which governs the sea state and surface slopes, and is of second order effect regarding the upward radiant field.

About the ocean itself, it is important to note that only Case-1 waters with varying [Chl] have been considered in the computations, because their average IOP are predictable and can be used as inputs in the RTE computations. Therefore, the BRDF effects are modelled for these Case-1 waters, and the present BRDF correction was proposed only for these waters.

The Q and f/Q coefficients have been produced for nadir angles, θ, between $1°$ and $90°$ (17 values), and for 13 values for the azimuth difference ($\Delta\phi$ from 0 to 180°). Therefore, the geometrical structure of the entire (2π sr) in-water upward radiance field is described with a sufficient spatial resolution for efficient interpolation. This description extending on the half space is more than what is needed when considering the radiances able to emerge (those within the Snell circle, with $\theta \sim 48°$), or those able to be included within the swath of an orbiting sensor ($\theta < 35° - 40°$). A full 2π description of the radiant field, however, is needed when comparing in-water upward radiance measurements and theoretical predictions, which is the only way of testing the skill of the radiance model.

Such tests were carried out with satisfactory results by using various radiance distribution camera systems at sea (Voss, 1989; Voss and Chapin, 2005). The first

successful comparison between experimental and predicted Q-values (Morel *et al.*, 1995) was made in Case-1 water with [Chl] ~0.3 mg m^{-3}, at three wavelengths, and with a sun-zenith angle varying from 32° to 80° (the historical data from Lake Pend Oreille, at various depths, were used additionally in this test). In a second series of comparisons made at four wavelengths, the variation in the sun zenith angle was restricted ($28° - 40°$), whereas the [Chl] range was large (0.14 – 11 mg m^{-3}) (Voss and Morel, 2005). Upwelling radiance distributions from several cruises in varied Case-1 waters ([Chl] from 0.03 to 1.4 mg m^{-3}) and with a wide range of solar zenith angles ($0 - 80°$), were studied (Voss *et al.*, 2007). From these data, it was shown that the RMS difference between modelled and measured $L_u(\theta, \Delta\phi)/L_u$(nadir) was of the order of 0.03, well within the noise in the data.

It can be concluded that, in Case-1 waters, the bidirectional effect is well understood and can be accurately corrected for. The situation is considerably less favorable in Case-2 waters (sediment-dominated or yellow substance dominated Case-2 waters), despite some preliminary attempts (Loisel and Morel, 2001) which cannot be generalized. The lack of a reliable prediction and the absence of generic parameterizations for the IOP in such complex waters currently remain a serious obstacle to further development, except on a case-by-case basis.

References

Antoine D., d'Ortenzio F., Hooker S.B., Becu G., Gentili B., Tailliez D., Scott A.J. (2008). Assessment of uncertainty in the ocean reflectance determined by three satellite ocean color sensors (MERIS, SeaWiFS and MODIS-A) at an offshore site in the Mediterranean Sea (BOUSSOLE project). J. Geophys. Res. 113, C07013, doi: 10.1029/2007JC004472

Antoine D., Morel A. (1998). Relative importance of multiple scattering by air molecules and aerosols in forming the atmospheric path radiance in the visible and near-infrared parts of the spectrum. Appl. Opt. 37: 2245-2259

Antoine D., Morel A. (1999). A multiple scattering algorithm for atmospheric correction of remotely sensed ocean color (MERIS instrument): principle and implementation for atmospheres carrying various aerosols including absorbing ones. Int. J. Remote Sens. 20: 1875-1916

Antoine D., Nobileau D. (2006). Recent increase of the dust load over the Mediterranean Sea, as revealed from 6 years of ocean color satellite (SeaWiFS) observations. J. Geophys. Res. 111, D12214, doi: 10.1029/2005JD006795

Austin R.W. (1974). The remote sensing of spectral radiance from below the ocean surface. In: Jerlov N.G., Nielsen E.S. (Eds.) Optical Aspects of Oceanography. Academic, San Diego, Calif., p 317-344

Bailey S.W., McClain C.R., Werdell P.J., Schieber B.D. (2000). Normalized water-leaving radiance and chlorophyll-a match-up analyses. Report No. Vol. 10, NASA Tech. Memo. 2000-206892, Hooker, S.B., Firestone, E.R. (Eds.), NASA Goddard Space Flight Center, Greenbelt, Maryland

Bailey S.W., Werdell P.J. (2006). A multi-sensor approach for the on-orbit validation of ocean color satellite data products. Remote Sens. Environ. 102: 12-23

Banzon V.F., Evans R.E., Gordon H.R., Chomko R.M. (2004). SeaWiFS observations of the Arabian Sea southwest monsoon bloom for the year 2000. Deep-Sea Res. II 51: 189-208

Brajard J., Jamet C., Moulin C., Thiria S. (2006). Use of a neuro-variational inversion for retrieving oceanic and atmospheric constituents from satellite ocean color sensor: Application to absorbing aerosols. Neural Networks 19: 178-185

Bricaud A., Morel A. (1987). Atmospheric correction and interpretation of marine radiances in CZCS imagery: use of a reflectance model. Oceanologica Acta, SP: 33-50

Chomko R., Gordon H.R. (1998). Atmospheric correction of ocean color imagery: use of the Junge power-law aerosol size distribution with variable refractive index to handle aerosol absorption. Appl. Opt. 37: 5560-5572

Chomko R.M., Gordon H.R. (2001). Atmospheric correction of ocean color imagery: test of the spectral optimization algorithm with SeaWiFS. Appl. Opt. 40: 2973-2984

Chomko R.M., Gordon H.R., Maritorena S., Siegel D.A. (2003). Simultaneous retrieval of oceanic and atmospheric parameters for ocean color imagery by spectral optimization: a validation. Remote Sens. Environ. 84: 208-220

Clark D.K. (1981). Phytoplankton algorithms for the Nimbus-7 CZCS. In: Gower J.R.F. (ed) Oceanography from Space. Plenum, New York, p 227-238

Clarke G.K., Ewing G.C., Lorenzen C.J. (1970). Spectra of backscattered light from the sea obtained from aircraft as a measure of chlorophyll. Science 167: 1119-1121

Clarke G.L., Ewing G.C. (1974). Remote spectroscopy of the sea for biological production studies. In: Jerlov N.G., Steemann-Nielsen E. (Eds.) Optical aspects of oceanography. Academic Press, London, New York, p 389-413

Cox C., Munk W. (1954). Measurements of the roughness of the sea surface from photographs of the sun's glitter. J. Opt. Soc. Am. 44: 838-850

Deschamps P.Y., Fougnie B., Frouin R., Lecomte P., Verwaerde C. (2004). SIMBAD: a field radiometer for satellite ocean color validation. Appl. Opt. 43: 4055-4069

Deuze J.L., Herman M., Santer R. (1989). Fourier series expansion of the radiative transfer equation in the atmosphere-ocean system. J. Quant. Spectrosc. Radiat. Transfer 41: 483-494

Ding K., Gordon H.R. (1994). Atmospheric correction of ocean-color sensors: effects of the Earth's curvature. Appl. Opt. 33: 7096-7106

Dubuisson P., Frouin R., Dessailly D., Duforêt L., Léon J.-F., Voss K., Antoine D. (2009). Estimating the altitude of aerosol plumes over the ocean from reflectance ratio measurements in the O_2 A-band. Rem. Sens. Environ, 113: 1899-1911

Fell F., Fischer J. (2001). Numerical simulation of the light field in the atmosphere ocean system using the matrix-operator method. J. Quant. Spectrosc. Radiat. Transfer 69: 351-388

Feng H., Vandemark D., Campbell J.W., Holben B.N. (2008). Evaluation of MODIS ocean color products at a northeast United States coast site near the Martha's Vineyard Coastal Observatory. Int. J. Remote Sens. 29: 4479-4497

Fougnie B. (1998). Contribution of the POLDER satellite sensor to observing ocean color (in French). Ph.D, No. 2342, University of Lille, France

Frouin R., Pelletier B. (2007). Fields of non-linear regression models for atmospheric correction of satellite ocean-color imagery. Remote Sens. Environ. 11: 450-465

Frouin R., Schwindling M., Deschamps P.Y. (1996). Spectral reflectance of sea foam in the visible and near infrared: *In situ* measurements and remote sensing implications. J. Geophys. Res. 101(C6): 14,361-14,372

Fukushima H., Higurashi A., Mitomi Y., Nakajima T., Noguchi T., Tanaka T., Toratani M. (1998). Correction of atmospheric effects on ADEOS/OCTS ocean color data: Algorithm description and evaluation of its performance. J. Oceanogr. 54: 417-430

Fukushima H., Toratani M., Murakami H., Deschamps P.Y., Frouin R., Tanaka A. (2007). Evaluation of ADEOS-II GLI ocean color atmospheric correction using SIMBADA handheld radiometer data. J. Oceanogr. 63: 533-543

Garver S.A., Siegel D.A. (1997). Inherent optical property inversion of ocean color spectra and its biogeochemical interpretation: 1. Time series from the Sargasso Sea. J. Geophys. Res. 102: 18,607-18,625

Gordon H.R. (1978). Removal of atmospheric effects rom satellite imagery of the oceans. Appl. Opt. 17: 1631-1636

Gordon H.R. (1980). A preliminary assessment of the NIMBUS-7 CZCS atmospheric correction algorithm in a horizontally inhomogenous atmosphere. In: Gower J.F.R. (ed) Oceanography from Space. Plenum Press, New York and London, p 281-294

Gordon H.R. (1989). Can the Lambert-Beer law be applied to the diffuse attenuation coefficient of ocean water. Limnol. Oceanogr. 34: 1389-1409

Gordon H.R. (1997). Atmospheric correction of ocean color imagery in the Earth Observing System era. J. Geophys. Res. 102: 17,081-17,106

Gordon H.R. (2005). Normalized water-leaving radiance: revisiting the influence of surface roughness. Appl.Opt. 44: 241-248

Gordon H.R., Brown J.W., Evans R.H. (1988a). Exact Rayleigh scattering calculations for use with the Nimbus-7 Coastal Zone Color Scanner. Appl. Opt. 27: 862-871

Gordon H.R., Brown O.B., Evans R.H., Brown J.W., Smith R.C., Baker K.S., Clark D.K. (1988b). A semianalytic radiance model of ocean color. J. Geophys. Res. 93: 10909-10924

Gordon H.R., Brown O.B., Jacobs M.M. (1975). Computed relationship between the inherent and apparent optical properties of a flat homogeneous ocean. Appl. Opt. 14: 417-427

Gordon H.R., Clark D.K. (1980). Atmospheric effects in the remote sensing of phytoplankton pigments. Boundary-layer Meteorology 18: 299-313

Gordon H.R., Clark D.K. (1981). Clear water radiances for atmospheric correction of coastal zone color scanner imagery. Appl. Opt. 20: 4175-4180

Gordon H.R., Clark D.K., Brown J.W., Brown O.B., Evans R.H., Broenkow W.W. (1983). Phytoplankton pigment concentrations in the Middle Atlantic Bight: comparison of ship determinations and CZCS estimates. Appl. Opt. 22: 20-36

Gordon H.R., Du T., Zhang T. (1997). Remote sensing of ocean color and aerosol properties: resolving the issue of aerosol absorption. Appl. Opt. 36: 8670-8684

Gordon H.R., Morel A. (1983). Remote assessment of ocean color for interpretation of satellite visible imagery: A review, Vol. Springer-Verlag, New York

Gordon H.R., Wang M. (1992). Surface roughness considerations for atmospheric correction of ocean color sensors. 2: Error in the retrieved water-leaving radiance. Appl. Opt. 31: 4261-4267

Gordon H.R., Wang M. (1994a). Retrieval of water-leaving radiance and aerosol optical thickness over the oceans with SeaWiFS: A preliminary algorithm. Appl. Opt. 33: 443-452

Gordon H.R., Wang M. (1994b). Influence of oceanic whitecaps on atmospheric correction of ocean-color sensor. Appl. Opt. 33: 7754-7763

Gross-Colzy L., Colzy F., Frouin R., Henry P. (2007a). A general ocean color atmospheric correction scheme based on principal component analysis-Part 1: Performance on Case 1 and Case 2 waters. In: Frouin R., Lee Z. (Eds.) Coastal Ocean Remote Sensing. SPIE, Bellingham, WA, doi: /10.1117/12.738508

Gross-Colzy L., Colzy F., Frouin R., Henry P. (2007b). A general ocean color atmospheric correction scheme based on principal component analysis-Part 2: Level 4 merging capabilities. In: Frouin R., Lee Z. (Eds.) Coastal Ocean Remote Sensing, Bellingham Wa, doi: /10.1117/12.738514

Hale G.M., Querry M.R. (1973). Optical constants of water in the 200-nm to 200-μm wavelength region. Appl. Opt. 12: 555-563

Jamet C., Thiria S., Moulin C., Crépon M. (2005). Use of a neurovariational inversion for retrieving oceanic and atmospheric constituents from ocean color imagery: A feasibility study. J. Atmos. Ocean Technol. 22: 460-475

Koepke P. (1984). Effective reflectance of oceanic whitecaps. Appl. Opt. 23: 1816-1824

Kuchinke C.P., Gordon H.R., Franz B.A. (2009). Spectral optimization for constituent retrieval in Case 2 waters I: Implementation and performance. Remote Sens. Environ. 113: 571-587

Kuchinke C.P., Gordon H.R., L. W. Harding J., Voss K.J. (2009). Spectral optimization for constituent retrieval in Case 2 waters II: Validation study in the Chesapeake Bay. Remote Sens. Environ. 113: 610-621

Liu X., Wang M., Shi W. (2009). A study of a Hurricane Katrina-induced phytoplankton bloom using satellite observations and model simulations. J. Geophys. Res. 114, C03023, doi: 10.1029/2008JC004934

Loisel H., Morel A. (2001). Non-isotropy of the upward radiance field in typical coastal (Case 2) waters. Int. J. Remote Sens. 22: 275-295

Maritorena S., Siegel D.A., Peterson A. (2002). Optimization of a semi-analytical ocean color model for global scale applications. Appl. Opt. 41: 2705-2714

McClain C., Esaias W., Feldman G., Frouin R., Gregg W., Hooker S. (2002). The proposal for the NASA Sensor Intercalibration and Merger for Biological and Interdisciplinary Oceanic Studies (SIMBIOS) Program, 1995. Report No. NASA Tech. Memo. 2002-210008, 54pp, NASA Goddard Space Flight Center, Greenbelt, Maryland, 54 pp

McClain C.R., Feldman G.C., Hooker S.B. (2004). An overview of the SeaWiFS project and strategies for producing a climate research quality global ocean bio-optical time series. Deep-Sea Res. II 51: 5-42

Mélin F., Zibordi G., Berthon J.F. (2007). Assessment of satellite ocean color products at a coastal site. Remote Sens. Environ. 110: 192-215

Mobley C.D. (1994). Light and Water: Radiative Transfer in Natural Waters, Academic, New York

Monahan E.C., O'Muircheartaigh I.G. (1986). Whitecaps and the passive remote sensing of the ocean surface. Int. J. Remote Sens. 7: 627-642

Moore G.F., Aiken J., Lavender S. (1999). The atmospheric correction of water color and the quantitative retrieval of suspended particulate matter in Case II waters: application to MERIS. Int. J. Remote Sens. 20: 1713-1733

Moore K.D., Voss K.J., Gordon H.R. (2000). Spectral reflectance of whitecaps: Their contribution to water-leaving radiance. J. of Geophys. Res. 105: 6493-6499

Morel A. (1980). In-water and remote measuements of ocean color. Boundary-layer Meteorol. 18: 177-201

Morel A. (1982). Optical properties and radiant energy in the waters of the Guinea dome and the Mauritanian upwelling area in relation to primary production. Conseil International pour l'Exploration de la Mer; Rapports et Proces Verbaux 180: 94-107

Morel A., Antoine D., Gentili B. (2002). Bidirectional reflectance of oceanic waters: accounting for Raman emission and varying particle scattering phase function. Appl. Opt. 41: 6289-6306

Morel A., Gentili B. (2004). Radiation transport within oceanic (case 1) water. J. Geophys. Res. 109: C06008, doi: 10.1029/2003JC002259

Morel A., Gentili G. (1991). Diffuse reflectance of oceanic waters: its dependence on Sun angle as influenced by the molecular scattering contribution. Appl. Opt. 30: 4427-4438

Morel A., Gentili G. (1993). Diffuse reflectance of oceanic waters. II. Bidirectional aspects. Appl. Opt. 32: 6864-6879

Morel A., Gentili G. (1996). Diffuse reflectance of oceanic waters. III. Implication of bidirectionality for the remote-sensing problem. Appl. Opt. 35: 4850-4862

Morel, A., Mueller, J.L. (2002). Normalized water-leaving radiance and remote sensing reflectance: bidirectional reflectance and other factors. In: Mueller, J.L., Fargion, G.S. (Eds.), Ocean Optics Protocols for Satellite Ocean Color Sensor Validation, Revision 3, Vol. 2, NASA/TM-2002-210004, Goddard Space Flight Center, Greenbelt, Maryland, USA, p 183-210

Morel A., Prieur L. (1977). Analysis of variations in ocean color. Limnol. Oceanogr. 22: 709-722

Morel A., Voss K.J., Gentili B. (1995). Bidirectional reflectance of oceanic waters - a comparison of modeled and measured upward radiance fields. J. Geophys. Res. 100: 13,143-13,150

Moulin C., Gordon H.R., Chomko R.M., Banzon V.F., Evans R.H. (2001a). Atmospheric correction of ocean color imagery through thick layers of Saharan dust. Geophys. Res. Letters 28: 5-8

Moulin C., Gordon H.R., Banzon V.F., Evans R.H. (2001b). Assessment of Saharan dust absorption in the visible from SeaWiFS imagery. J. Geophys. Res. 106: 18,239-218,249

Mueller J.M., Fargion G.S. (2002). Ocean Optics Protocols for Satellite Ocean Color Sensor Validation, Revision 3, Part I & II. Report No. NASA Tech. Memo. 2002-210004, NASA Goddard Space Flight Center, Greenbelt, Maryland, USA

Murakami H., Sasaoka K., Hosoda K., Fukushima H., Toratani M., Frouin R., Mitchell B.G., Kahru M., Deschamps P.Y., Clark D., Flora S., Kishino M., Saitoh S., Asanuma I., Tanaka A., Sasaki H., Yokouchi K., Kiyomoto Y., Saito H., Dupouy C., Siripong A., Matsumura S., Ishizaka J. (2006). Validation of ADEOS-II GLI ocean color products using *in situ* observations. J. Oceanogr. 62: 373-393

Nakajima T., Tanaka M. (1988). Algorithms for radiative intensity calculations in moderately thick atmospheres using a truncation approximation. J. Quant. Spectrosc. Radiat. Transfer 40: 51-69

Nakajima T., Tanaka M., Yamamoto M., Shiobara M., Arao K., Nakanishi Y. (1989). Aerosol optical characteristics in the yellow sand events observed in May, 1982 at Nagasaki-part II models. J. Meteor. Soc. Japan 67: 279-291

NASDA-EOC (1997). Advanced Earth Observing Satellite (ADEOS) OCTS data processing algorithm description, Ver. 2.0.1. http://suzaku.eorc.jaxa.jp/GLI2/adeos/Products/Specifications/OCTSAlgoPDF.html

NASDA-EOC (2004). GLI ocean algorithm description: Atmospheric correction (OTSK1A), Ver.2.1. http://suzaku.eorc.jaxa.jp/GLI/ocean/algorithm/index.html

Nezlin N.P., DiGiacomo P.M., Diehl D.W., Jones B.H., Johnson S.C., Mengel M.J., Reifel K.M., Warrick J.A., Wang M. (2008). Stormwater plume detection by MODIS imagery in the southern California coastal ocean. Est. Coast. Shelf Sci. 80: 141-152

Nicolas J.M., Deschamps P.Y., Frouin R. (2001). Spectral reflectance of oceanic whitecaps in the visible and near infrared: Aircraft measurements over open ocean. Geophy. Res. Lett. 28: 4445-4448

Nobileau D., Antoine D. (2005). Detection of blue-absorbing aerosols using near infrared and visible (ocean color) remote sensing observations. Remote Sens. Environ. 95: 368-387

Patt F.S., Barnes R.A., R. E. Eplee J., Franz B.A., Robinson W.D., Feldman G.C., Bailey S.W., Gales J., Werdell P.J., Wang M., Frouin R., Stumpf R.P., Arnone R.A., R. W. Gould J., Martinolich P.M., Ransibrahmanakul V., O'Reilly J.E., Yoder J.A. (2003). Algorithm updates for the fourth SeaWiFS data reprocessing. Report No. Vol. 22, NASA Tech. Memo. 2003-206892, Hooker, S.B., Firestone, E.R. (Eds.), NASA Goddard Space Flight Center, Greenbelt, Maryland, 74 pp

Pelletier B., Frouin R. (2006). Remote sensing of chlorophyll-a concentration by use of ridge function fields. Appl. Opt. 45: 784-798

Ruddick K.G., Ovidio F., Rijkeboer M. (2000). Atmospheric correction of SeaWiFS imagery for turbid coastal and inland waters. Appl. Opt. 39: 897-912

Schroeder T., Behnert I., Schaale M., Fischer J., Doerffer R. (2007). Atmospheric correction algorithm for MERIS above case-2 waters. Int. J. Remote Sens. 28: 1469-1486

Shettle E.P., Fenn R.W. (1979). Models for the Aerosols of the Lower Atmosphere and the Effects of Humidity Variations on Their Optical Properties. Report No. AFGL-TR-79-0214, U.S. Air Force Geophysics Laboratory, Hanscom Air Force Base, Mass.

Shi W., Wang M. (2007). Observations of a Hurricane Katrina-induced phytoplankton bloom in the Gulf of Mexico. Geophy. Res. Lett. 34(11): L11607

Shi W., Wang M. (2008). Three-dimensional observations from MODIS and CALIPSO for ocean responses to cyclone Nargis in the Gulf of Martaban. Geophy. Res. Lett. 35: L21603, doi: 10.1029/2008GL035279

Shi W., Wang M. (2009). Satellite observations of flood-driven Mississippi River plume in the spring of 2008. Geophy. Res. Lett. 36: L07607, doi: 10.1029/2009GL037210

Shimada M., Oaku H., Mitomi Y., Murakami H., Nakamura Y., Ishizaka J., Kawamura H., Tanaka T., Kishino M., Fukushima H. (1998). Calibration and validation of the ocean color version-3 product from ADEOS OCTS. J. Oceanogr. 54: 401-416

Siegel D.A., Wang M., Maritorena S., Robinson W. (2000). Atmospheric correction of satellite ocean color imagery: the black pixel assumption. Appl. Opt. 39: 3582-3591

Smith R.C., Baker K.S. (1978). The bio-optical state of ocean waters and remote sensing. Limnol. Oceanogr. 23: 247-259

Smith R.C., Baker K.S. (1981). Optical properties of the clearest natural waters. Appl. Opt. 20: 177-184

Smith R.C., Wilson W.H. (1981). Ship and satellite bio-optical research in the California Bight. In: Gower J.F.R. (ed) Oceanography from Space. Plenum Press, New York and London, p 281-294

Steinmetz F. (2008). Study of the correction of atmospheric scattering and sunlight reflected by the wind-ruffled surface for observing ocean color from space (in French). Ph.D, No. 4160, University of Lille, France

Tanaka A., Kishino M., Doerffer R., Schiller H., Oishi T., Kubota T. (2004). Development of a neural network algorithm for retrieving concentrations of chlorophyll, suspended matter and yellow substance from radiance data of the Ocean Color and Temperature Scanner. J. Oceanogr. 60: 519-530

Toratani M., Fukushima H., Murakami H., Tanaka A. (2007). Atmospheric correction scheme for GLI with absorptive aerosol correction. J. Oceanogr. 63: 525-532

Tyler J.E. (1973). SCOR Discoverer Expedition, May 1970: data report - measurements of photosynthesis, available radiant flux and supporting oceanographic data. Unesco-sponsored programmes and publications, University of California, Scripps Institution of Oceanography, San Diego, USA

Tyler J.E., Smith R.C. (1970). Measurements of spectral irradiance underwater, Vol. Gordon and Breach Science Publishers, New York, 103 pp

Viollier M., Tanre, D., Deschamps P. Y. (1980). An algorithm for remote sensing of water color from space. Boundary Layer Meteorol. 18: 247-267

Voss K.J. (1989). Electro-optic camera system for measurement of the underwater radiance distribution. Optical Engineering 28: 241-247

Voss K.J., Chapin A.L. (2005). Upwelling radiance distribution camera system, NURADS. Optics Express 13: 4250-4262

Voss K.J., Morel A., Antoine D. (2007). Detailed validation of the bidirectional effect in various Case 1 waters for application to ocean color imagery. Biogeosciences 4: 781-789

Wang M. (2000). The SeaWiFS atmospheric correction algorithm updates. Report No. Vol. 9, NASA Tech. Memo. 2000-206892, Hooker, S.B., Firestone, E.R. (Eds.), NASA Goddard Space Flight Center, Greenbelt, Maryland

Wang, M. (2002). The Rayleigh lookup tables for the SeaWiFS data processing: Accounting for the effects of ocean surface roughness. Int. J. Remote Sens. 23: 2693-2702.

Wang M. (2004). Extrapolation of the aerosol reflectance from the near-infrared to the visible: the single-scattering epsilon vs multiple-scattering epsilon method. Int. J. Remote Sens. 25: 3637-3650

Wang M. (2005). A refinement for the Rayleigh radiance computation with variation of the atmospheric pressure. Int. J. Remote Sens. 26: 5651-5663

Wang M. (2006a). Aerosol polarization effects on atmospheric correction and aerosol retrievals in ocean color remote sensing. Appl. Opt. 45: 8951-8963

Wang M. (2006b). Effects of ocean surface reflectance variation with solar elevation on normalized water-leaving radiance. Appl. Opt. 45: 4122-4128

Wang M. (2007). Remote sensing of the ocean contributions from ultraviolet to near-infrared using the shortwave infrared bands: simulations. Appl. Opt. 46: 1535-1547

Wang M., Bailey S. (2001). Correction of the sun glint contamination on the SeaWiFS ocean and atmosphere products. Appl. Opt. 40: 4790-4798

Wang M., Gordon H.R. (1994). A simple, moderately accurate, atmospheric correction algorithm for SeaWiFS. Remote Sens. Environ. 50: 231-239

Wang M., Knobelspiesse K.D., McClain C.R. (2005). Study of the Sea-Viewing Wide Field-of-View Sensor (SeaWiFS) aerosol optical property data over ocean in combination with the ocean color products. J. Geophys. Res. 110, D10S06, doi: 10.1029/2004JD004950

Wang M., Shi W. (2005). Estimation of ocean contribution at the MODIS near-infrared wavelengths along the east coast of the U.S.: Two case studies. Geophy. Res. Lett. 32(13): L13606.1-L13606.5

Wang M., Shi W. (2008). Satellite observed algae blooms in China's Lake Taihu. Eos Trans. AGU 89: 201-202

Wang M., Son S., Shi W. (2009). Evaluation of MODIS SWIR and NIR-SWIR atmospheric correction algorithm using SeaBASS data. Remote Sens. Environ. 113: 635-644

Wang M., Tang J., Shi W. (2007). MODIS-derived ocean color products along the China east coastal region. Geophy. Res. Lett. 34, L06611, doi: 10.1029/2006GL028599

Werdell P.J., Bailey S., Fargion G., Pietras C., Knobelspiesse K., Feldman G., McClain C.R. (2003). Unique data repository facilitates ocean color satellite validation Eos, Transactions, American Geophysical Union, 377 pp

Werdell P.J., Bailey S.W. (2005). An improved *in-situ* bio-optical data set for ocean color algorithm development and satellite data product validation. Remote Sens. Environ. 98: 122-140

Yang H., Gordon H.R. (1997). Remote sensing of ocean color: assessment of water-leaving radiance bidirectional effects on atmospheric diffuse transmittance. Appl. Opt. 36: 7887-7897

Zibordi G., Mélin F., Berthon J.-F. (2006). Comparison of SeaWiFS, MODIS and MERIS radiometric products at a coastal site. Geophy. Res. Lett. 33: L06617, 10.1029/2006GL025778

Acronyms and Abbreviations

ACWG	Atmospheric Correction Working Group
AOT	Aerosol Optical Thickness
BRDF	Bi-directional Reflectance Distribution Function
CNES	Centre National d'Etudes Spatiales
CZCS	Coastal Zone Color Scanner
ESA	European Space Agency
GLI	Global Imager
IOCCG	International Ocean-Colour Coordinating Group
IOP	Inherent Optical Property
JAXA	Japan Aerospace Exploration Agency
LIDAR	Light Detection and Ranging
LOA	Laboratoire d'Optique Atmosphérique
LUTs	Lookup Tables
MERIS	Medium Resolution Imaging Spectrometer
MODIS	Moderate Resolution Imaging Spectroradiometer
MOM	Matrix Operator Method
NASA	National Aeronautics and Space Administration
NASDA	National Space Development Agency of Japan (now JAXA)
NIR	Near-Infrared
NOMAD	NASA bio-Optical Marine Algorithm Dataset
OCTS	Ocean Color and Temperature Scanner
POLDER	Polarization and Directionality of the Earth's Reflectances
PPA	Plane-Parallel Atmosphere
RH	Relative Humidity
RTE	Radiative Transfer Equation
RMS	Root Mean Square
SeaWiFS	Sea-viewing Wide Field-of-View Sensor
SSE	Single Scattering Epsilon
SIMBAD	Optical radiometer designed by LOA to validate ocean-colour observations from space
SIMBADA	Advanced SIMBAD
SIMBIOS	Sensor Intercomparison for Marine Biological and Interdisciplinary Ocean Studies
SMA	Spectral Matching Algorithm
SOA	Spectral Optimization Algorithm

SOS	Successive Order of Scattering
SSE	Single Scattering Epsilon
STD	Standard Deviation
SWIR	Shortwave Infrared
TOA	Top of Atmosphere
VIS	Visible
VSF	Volume Scattering Function